

INVESTIGATION OF TRANSLATION ELONGATION, TERMINATION AND
RECYCLING BY BULK BIOCHEMICAL AND SINGLE MOLECULE METHODS

by
Laura Nevin Lessen

A dissertation submitted to Johns Hopkins University in conformity with the
requirements for the degree of Doctor of Philosophy

Baltimore, Maryland
September 2019

© 2019 Laura Nevin Lessen
All Rights Reserved

Abstract

The process of translation of mRNAs into functional proteins by the ribosome is crucial to cell viability. Problems encountered by the ribosome during any of the phases of this process can have major deleterious effects. Although, our understanding of the steps of the translation have grown immensely over the years, specific questions regarding the complex dynamics of these processes have yet to be fully understood. In particular, recent studies have elucidated pauses during elongation that are caused by specific pairs of codons. Through the use of *in vitro* biochemical experiments in tandem with and *in vivo* ribosome profiling and cryo-EM structures to investigate these inhibitory codon pairs, we were able to demonstrate that this type of elongation stalling is mainly caused by slow decoding in the ribosomal A site. The mechanistic details of how the ribosome is rescued from stalls similar to these during elongation, as well as the similar processes of termination and recycling, also remain to be fully understood. Through my development of a single molecule fluorescence microscopy assay to investigate ribosome rescue, termination and recycling these dynamics can be further explored. Taken together, I have furthered our understanding of a particular type of elongation pause using an *in vitro* biochemical system and have expanded that system for use at the single molecule level to investigate the dynamic processes of translation further.

Rachel Green, Ph.D. (Sponsor and Reader)

Professor

Department of Molecular Biology & Genetics

Johns Hopkins University School of Medicine

Jie Xiao, Ph.D. (Reader)

Professor

Department of Biophysics & Biophysical Chemistry

Johns Hopkins University School of Medicine

Acknowledgements

First, I would like to thank my advisor Rachel Green for her continuous support throughout graduate school. The intellectual environment of the lab stems directly from her curiosity, expertise and leadership and has been a challenging and wonderful place to pursue my Ph.D.

I would also like to thank all the members of my thesis committee, Jie Xiao, James Berger, Taekjip Ha and Christian Kaiser for their input and advice throughout my Ph.D. Special thanks also to the Berger Lab, Puglisi lab and Beckmann lab, whom I had the privilege of collaborating with. I would especially like to thank Tim Wendorff from the Berger lab for allowing me to venture into the world of single molecule with him. To the Program in Molecular Biophysics and the staff, thank you for the opportunity to pursue my Ph.D. here at Hopkins and for your guidance throughout.

I also have to give a huge thanks to the past and current members of the Green lab who made working in lab every day enjoyable. In particular: to my original bay mate and mentor, Anthony, thank you for teaching me everything I needed to know about the lab and the system that would yield all of the results of my Ph.D. work; to my new bay mate and co-founder of the “Lady-bay”, Karole, for enlightening me about the wonders of yeast genetics and helping to keep me sane during these last years of my Ph.D; to Julie for keeping the lab running and functioning on a daily basis; and to Colin for all his complementary *in vivo* work and for the growing pet I get to stare at on my bench each day.

Thank you to all my friends that have supported me throughout this time both from the Biophysics program and outside of it. Special thanks to my classmates Chris (and Shannon) and Ryan for making me laugh and commiserating over graduate school struggles.

Extra special thanks go out to my parents who have always encouraged and enabled me to pursue my goals. I could not have gotten to graduate school or completed my degree without your love and support. I am so blessed to have a wonderfully supportive family that grew even further during graduate school – thank you and I love you all!

Lastly, and mostly, I have to thank my husband and classmate, Henry. Meeting you in graduate school was nothing short of a blessing. Your encouragement and support are never-ending and you inspire me to continue learning and growing every day. I look forward to our continued adventures together as The Doctors Lessen.

Table of Contents

Abstract	ii
Acknowledgements	iv
List of Figures	viii
Chapter 1: Introduction	1
Elongation	3
Ribosome stalling during elongation	4
Termination	6
Ribosome rescue	7
Recycling	8
Conclusion	9
Figures	10
Figure Legends	14
References	18
Chapter 2: Slow decoding of problematic codon pairs during translation elongation	21
Introduction	22
Results	24
Discussion	39
Figures	46
Figure Legends	69
Methods	81
References	94

Chapter 3: Development of a single molecule system to investigate the molecular mechanisms of translation termination, ribosome rescue and recycling	97
Introduction	98
Results	100
Discussion	108
Figures	111
Figure Legends	121
Methods	128
References	138
Curriculum Vitae	141

List of Figures

Chapter 1

Figure 1. Overview of eukaryotic translation and specific steps of translation	
elongation	10
Figure 2. Ribosome stalling during elongation	11
Figure 3. Canonical translation termination versus ribosome rescue	12
Figure 4. Ribosome recycling following termination or rescue	13

Chapter 2

Figure 1. Inhibitory codon pairs slow elongation <i>in vitro</i>	46
Figure 2. Effects of tRNA concentration on elongation rates and endpoints	47
Figure 3. Increased 21 nt RPFs on inhibitory pairs indicate an empty ribosomal	
A site	48
Figure 4. Loss of the ribosomal protein Asc1 inhibits elongation	49
Figure 5. CGA-CCG and CGA-CGA induce stalling through decoding-incompatible	
mRNA conformations in the A site	50
Figure 6. Ribosomes stalled on poly(A) stretches reveal alterations in both the	
peptidyl-transferase and decoding centers	51
Figure 7. Disomes stalled on poly(A) tracts form a novel POST-POST assembly	52
Figure EV1. Initiation complex test of Met-Pm activity and individual product	
analysis of MFRR elongation	53

Figure EV2. Ribosome profiling analysis showing defects in peptide bond formation	54
Figure EV3. Initiation complex test of Met-Pm activity with ribosomes lacking Asc1 and their corresponding elongation rates	55
Figure EV4. Cryo-EM structures of RNCs stalled on inhibitory codon pairs in comparison with the A site decoding situation	56
Figure EV5. Structural details of the codon-based stalling	57
Figure EV6. Elongation of AAA is slower than AAG on MFK5 initiation complexes	58
Figure S1. CGA-CCG reporter mRNA and purification of the stalled 80S RNCs	59
Figure S2. CGA-CGA reporter mRNA and purification of the stalled 80S RNCs	60
Figure S3. 3D classification and processing scheme of the 80S ribosomes stalled on the CGA-CCG reporter mRNA	61
Figure S4. 3D classification and processing scheme of the 80S ribosomes stalled on the CGA-CGA reporter mRNA	62
Figure S5. Puromycin reactivity of CGA-CGA and CGA-CCG stalled RNCs	63
Figure S6. Poly(A) reporter mRNA and purification of the stalled 80S RNCs	64
Figure S7. 3D classification and processing scheme of the 80S ribosomes stalled on the poly(A) reporter mRNA	65
Figure S8. Local resolution and FSC curves for the 80S cryo-EM density maps of stalled ribosomes	66
Figure S9. 3D classification and processing scheme of the disomes stalled on the poly(A) reporter mRNA	67

Figure S10. Local resolution and FSC curves for the individually refined 80S cryo-EM density maps of poly(A) stalled disomes	68
--	----

Chapter 3

Figure 1. Construction of single molecule TIRF microscope	111
Figure 2. Steps of sample chamber preparation	112
Figure 3. Ribosome labeling and function tests	113
Figure 4. Single molecule visualization of initiation complexes with labeled ribosomes	114
Figure 5. Characterization of a Cy5-M labeled ribosomes by single molecule visualization	115
Figure 6. Testing of labeled RLI1 for ribosome recycling activity	116
Figure 7. Testing of labeled eRF1 and eRF3 for canonical termination by peptide release	117
Supplementary Figure 1. Function of Cy5-M complexes in vitro and further characterization of their lifetimes	118
Supplementary Figure 2. Purification of RLI1-SNAP construct	119
Supplementary Figure 3. Purification of labeled termination and rescue factors	120

Chapter 1: Introduction

Cell viability and function relies on the flow of genetic material from DNA to RNA to protein, referred to as the central dogma of biology. The process of translating the RNA sequence into the various proteins needed for cells to function is carried out by the molecular machine known as the ribosome. The ribosome is comprised at its core of RNA which carries out its catalytic functions and contains over 40 protein factors that allow it to catalyze the process of translation through three main sites known as the amino-acyl site (A-site), the peptidyl site (P-site) and the exit site (E-site). The ribosome requires many additional factors to successfully carry out translation including messenger RNAs (mRNAs), transfer RNAs (tRNAs) as well as other accessory protein factors. Together, these factors, with the ribosome at the core, ensure fidelity throughout translation to synthesize the functional proteins needed throughout the cell. While the function of the ribosome was discovered many years ago, there is a lot more we continue to learn about its function and how translation is regulated in cells.

The process of translation is highly regulated and is comprised of four main steps: initiation, elongation, termination and recycling (Figure 1A). Translation must be performed with high fidelity in order for cell maintenance and viability and, as such, is generally conserved throughout different domains of life while there are still substantial differences as well. Here, I will focus on eukaryotic translation, especially in the model organism *S. cerevisiae*. For proper translation to occur the ribosome, with the help of many protein initiation factors, is positioned with a start codon (AUG) and initiator methionine tRNA in the ribosomal P-site. Elongation then follows with the movement of the ribosome

along the mRNA transcript one codon (three nucleotides) at a time. As the ribosome moves along an mRNA, it coordinates the interaction of aminoacyl-tRNAs that carry a specific amino acid, corresponding to their cognate mRNA codons. The ribosome, with the help of elongation factors, catalyzes the peptidyl transfer reaction that forms peptide bonds between amino acids, thereby synthesizing a growing peptide chain. Elongation continues until the ribosome reaches a stop codon within its A-site which usually occurs at the end of an open reading frame (ORF) triggering translation termination. Termination is carried out by the factors eRF1 and eRF3 which recognize the stop codon and coordinate the release of the polypeptide chain, forming the functional protein. Ribosome recycling, the final step of translation, is primarily carried out by the protein RLI1 (ABCE1 in higher eukaryotes) and returns the ribosomal subunits to the free pool needed for continued translation of other mRNA transcripts.

In this chapter, I will focus on the current understanding of the steps of elongation, termination and recycling within the translation field. I will pay particular attention to the problems that the ribosome can encounter during translation elongation and how these problems are resolved. These problems present kinetic barriers that the ribosome must either get through or be rescued from. I will then compare canonical termination and ribosome recycling to ribosome rescue that occurs when problems encountered by the ribosome cannot be resolved. The kinetic barriers that the ribosome faces during each round of translation have a large impact on overall cellular function and viability and are an important area of continued research.

Elongation

Translation elongation begins when the first amino acid following the start codon is added to the peptide chain and ends when a stop codon enters the ribosomal A-site at the end of an ORF. This process is highly conserved between bacteria and eukaryotes and proceeds through three steps: tRNA decoding and accommodation into the ribosomal A-site, peptide bond formation, and translocation (Figure 1B). Amino acids for the growing peptide chain are brought to the ribosome on amino-acylated tRNAs in complex with the highly abundant elongation factor eEF1A (EF-Tu in bacteria) and GTP^{1, 2}. The anticodon stem loop of the amino-acylated tRNA is matched to the codon in the A-site in a process known as decoding. It is during this step that improper aa-tRNAs are rejected from the ribosome. Once the cognate codon-anticodon interaction is matched in the ribosomal A-site, the GTPase eEF1A activates, hydrolyzes GTP and is subsequently released as eEF1A-GDP from the ribosome, locking the A site tRNA into the proper position (reviewed for bacteria³). This process of accommodation brings the amino acid of the aa-tRNA into the peptidyl transferase center of the large subunit of the ribosome. The amine side chain of the A-site tRNA is then poised for nucleophilic attack on the aminoacyl ester linkage of the P-site tRNA and the growing peptide chain is moved to the tRNA in A-site of the ribosome (reviewed for bacteria⁴). As the peptide bond is being formed the ribosome moves into what is known as the rotated state, positioning the acceptor ends of the P and A site tRNAs into the E and P sites while the anticodon ends remain in the P and A sites, respectively (E/P and P/A hybrid states)⁵⁻⁷. This rotated state of the ribosome is the substrate for the binding of the elongation factor eEF2 in complex with GTP. The hydrolysis of GTP allows for ribosome translocation, moving the hybrid state tRNAs back

into the classical state, but now one codon further along the mRNA, placing them in the E and P sites of the ribosome⁸⁻¹². An additional, essential, elongation factor in fungi, eEF3, may promote the release of the E-site tRNA^{13, 14}. The previously named initiation factor 5A (eIF5A), has also been shown to promote elongation through binding to the ribosomal E-site when it is unoccupied for long periods of time such as when the ribosome is moving through slowly translated sequences¹⁵. Together these steps open the A-site for the next round of elongation through the same steps of decoding, accommodation, and translocation to continue building the polypeptide.

Ribosome stalling during elongation

The translating ribosome encounters many different “roadblocks” impeding its progress during elongation (for an extensive review see ref¹⁶). Here, I will focus on impediments caused by the mRNA and tRNA substrates of the ribosome. First, to discuss these substrates it is important to note that, although there are 20 amino acids, there are 61 codons that code for them. This degeneracy allows multiple codons to code for a particular amino acid and multiple tRNAs to bring the same amino acid to the ribosome. Some mRNA codon-anticodon interactions do not match perfectly through Watson-Crick base-pairing, but instead require wobble decoding (Figure 2A)¹⁷. Wobble pairing occurs between the 3' nucleotide of the mRNA codon and the 5' nucleotide of the tRNA anticodon and most commonly involves a G-U wobble pair. Other wobble pairs allowed in this position by the ribosome include I-A, I-U and I-C, which all involve the deaminated guanosine nucleobase, inosine (I). Wobble decoding allows cells to express fewer than 61 different tRNAs to decode all possible codons¹⁸, albeit more slowly than canonical Watson-

Crick decoding^{19, 20}. Therefore, the process of decoding can affect the rate of translation since mRNA codons are decoded at different rates^{21, 22}.

Another determinant of the rate of decoding by the ribosome is the “optimality” or “rarity” of a given codon^{23, 24}. Codons are defined as optimal or rare based on where and how often they appear in the transcriptome. Optimal codons are used abundantly in highly expressed genes, where rare codons are used minimally^{25, 26}. Correspondingly, optimal codons are decoded faster than their rare counterparts^{27, 28}. Optimality also correlates with the copy number of tRNAs within a cell, which is used as a proxy for the expression level of a given tRNA²⁹ (Figure 2B). tRNA copy number varies greatly from as few as one genomic copy to as many as 16 in *S. cerevisiae*^{30, 31}. In addition to tRNA copy number, tRNA sequence varies greatly between different species.³² Furthermore, the availability of charged tRNA within the cell also determines the rate at which it will be decoded by the ribosome^{27, 33, 34}. This results from the distinct, yet related, inefficiency of tRNA aminoacylation by specific aminoacyl-tRNA synthetases in the cell. Uncharged tRNAs within the cytoplasm compete for binding within the ribosomal A-site during decoding and will be rejected, thereby slowing the rate of decoding^{35, 36}. For these reasons, optimal codons are used frequently throughout the transcriptome, particularly in highly transcribed genes, to maintain a large pool of charged tRNA available for continued elongation^{25, 26, 29}.

As discussed above, the specific mRNA codons being translated by the ribosome affect the rate of elongation. Interestingly, sequential pairs of codons have been implicated in the rate of translation, beyond the contribution of the individual codons^{37, 38}. A recent, comprehensive study in yeast used a fluorescent protein reporter to score the expression of a reporter containing randomized pairs of adjacent codons.³⁹ This study identified 17 codon

pairs that inhibit translation (Figure 2C). They showed that these effects are different from those exhibited by individual codons or the amino acid being added to the peptide chain. Many of the inhibitory pairs identified involve wobble decoding and tRNAs with low copy number as described above. For many of these pairs the order of the codons mattered for this inhibition. This finding implies that the interaction of tRNAs with one another and the ribosome could play a direct role in this inhibition. Further investigation into this type of inhibition will further our understanding of the communication between the different sites of the ribosome and how exactly the ribosome handles these troublesome sequences.

Termination

The ribosome elongates through the ORF until it reaches a stop codon (UGA, UAG, or UAA) in its A-site, triggering translation termination (Figure 3A)⁴⁰. In eukaryotes, the termination factor, eRF1 recognizes all three stop codons within the A-site. It is delivered to the ribosome by an accessory GTPase, eRF3 similar to delivery of aa-tRNAs by eEF1A during elongation^{41, 42}. eRF1 is structurally similar to tRNA and contains two essential motifs that allow it to carry out its function in termination (Figure 3B). When eRF1 binds in the A-site it recognizes the stop codon through its NIKS motif (Arg-Ile-Lys-Ser)⁴³⁻⁴⁵. Upon recognition it is thought that eRF3 then hydrolyzes GTP^{46, 47}, positioning eRF1 into its activated confirmation where the catalytic GGQ (Gly-Gly-Glu) motif of eRF1 is positioned near the peptidyl transferase center of the large subunit⁴⁸. This motif coordinates a water molecule as a nucleophile to attack the polypeptide chain on the P-site tRNA, releasing it from the tRNA and the ribosome for use in the cell, and ending the termination phase of translation.

Ribosome Rescue

Although most ribosomes reach the stop codon at the end of an ORF, instances arise within cells where ribosomes stall prematurely along the ORF. Stalling can be caused by mRNA sequence (Figures 2B and 2C), amino acid sequence, mRNA structure, and genetic mutations leading to premature termination codons within an ORF, and truncated mRNAs, to name a few examples. In all of these cases the stalled ribosomes need to be rescued from the mRNA in order to return them to the free pool for continued translation throughout the cell (Figure 3A). This occurs through a set of complex pathways, known as ribosome quality control, that release the ribosomes, degrade the aberrant polypeptide, and degrade the problematic mRNA that led to these problems.^{49, 50}

The process of ribosome rescue requires the protein factors DOM34 and HBS1 in yeast (Pelota and HBS1L in mammalian cells)⁵¹⁻⁵³. DOM34 is structurally homologous to the canonical termination factor eRF1 with two key differences that highlight the different functions performed by these two proteins^{54, 55} (Figure 3B). DOM34 lacks the NIKS motif that recognizes the stop codon of the mRNA within the A-site of the ribosome. This allows DOM34 to act at all codons rather than requiring stop codons specifically for its function. Secondly, DOM34 lacks the catalytic GGQ motif that eRF1 has to hydrolyze the peptide from the P site tRNA. As an outcome, DOM34 does not release the growing polypeptide from the tRNA and the ribosome during the rescue process⁵⁶. Despite these two important differences, DOM34 is thought to be delivered to the ribosome in complex with its accessory GTPase HBS1 and the GTP hydrolysis of HBS1 is thought to be important to position DOM34 correctly within the A-site of the stalled ribosome. Overall, DOM34 and

HBS1 act on ribosomes that encounter obstacles during translation elongation in order for these ribosomes to be recycled⁵⁷⁻⁵⁹ – the final step in translation discussed below.

Recycling

Following canonical termination with eRF1 and eRF3 and ribosome rescue with DOM34 and HBS1, the large and small subunits of the ribosome must be released from the mRNA to allow them to translate other mRNAs. The substrate for recycling is slightly different in these two cases (Figure 4A & 4B). For canonical termination, the polypeptide chain has been released from the P site tRNA, but the tRNA remains bound to the ribosome. In the rescue situation, the peptidyl tRNA is bound in the P-site of the ribosome with the incomplete polypeptide still attached. In both cases, the tRNA is released from the ribosomes and the small and large subunits from the mRNA by the action of the ATPase RLI (ABCE1 in mammalian cells)^{60, 61}. This protein shares a binding site on the ribosome with the termination factor eRF3 and the rescue factor HBS1 suggesting that GTP hydrolysis and release of these factors from the ribosome is required before RLI1 is able to bind^{45, 62}. RLI1 then uses the force generated from hydrolysis of ATP to separate the ribosomal subunits. It is thought that RLI1 propagates this force through eRF1, pushing this factor into the intersubunit space and separating the large subunit of the ribosome⁴⁵. Once the subunits are released, they are bound by initiation factors to prevent rebinding. ABCE1 has also been shown to bind to 40S subunits alone and it was initially identified to play a role in translation initiation potentially linking the end of recycling to re-initiation and continued cell proliferation.⁶³⁻⁶⁶

Conclusion

Since the discovery of the ribosome and the genetic code, years of research have led to our current understanding of the translation process. The translation cycle is a highly dynamic and directional process. Much of our current understanding comes from measurements of bulk samples with many molecules functioning simultaneously in solution. These methods are still being used to examine many of the remaining questions in the field. Roadblocks to translation elongation and how the ribosomes are able to continue is currently a major area of exploration. The discovery inhibitory codon pairs raises questions about how these codons mediate their specific effects. Is it through the interactions of tRNAs on the ribosome? Are these mRNAs threaded through the ribosome differently than others? Moving to the end of the translation cycle, there is still much to be elucidated regarding the mechanisms of canonical termination, rescue and ribosome recycling – How are stop codons recognized as correct or premature in the context of an mRNA? How do the termination factors and rescue factors communicate with one another and with the recycling factor RLI1? In chapter 2, I will use bulk biochemical experiments to further understand the translation of inhibitory codon pairs, specifically attempting to gain knowledge into how these different pairs are handled by the ribosome. Then, in chapter 3, I discuss my work to develop single molecule methods to allow further investigation into the specific, dynamic mechanisms of translation termination, ribosome rescue and recycling. Using both traditional biochemical kinetic methods as well as time resolved single molecule methods we hope to learn more about the highly dynamic and directional kinetic steps in translation elongation, termination and recycling.

Figures

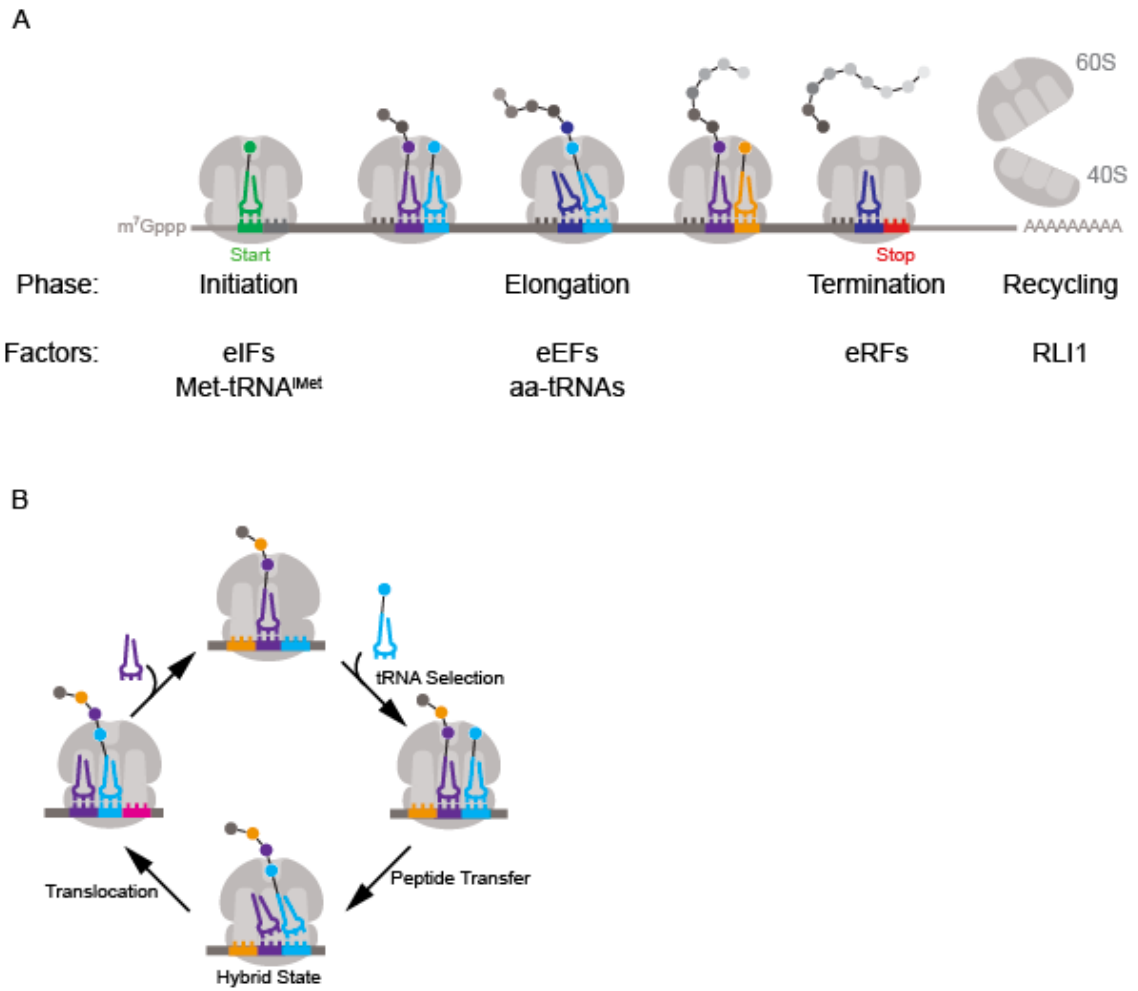


Figure 1

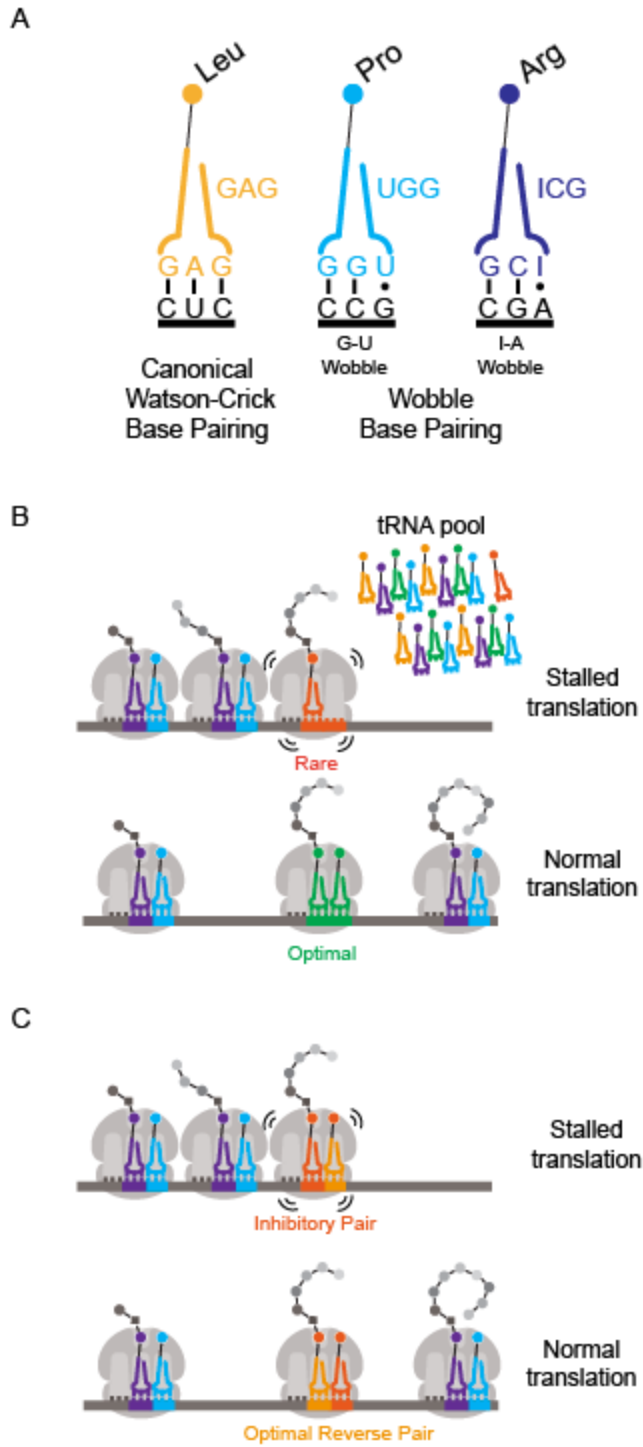


Figure 2

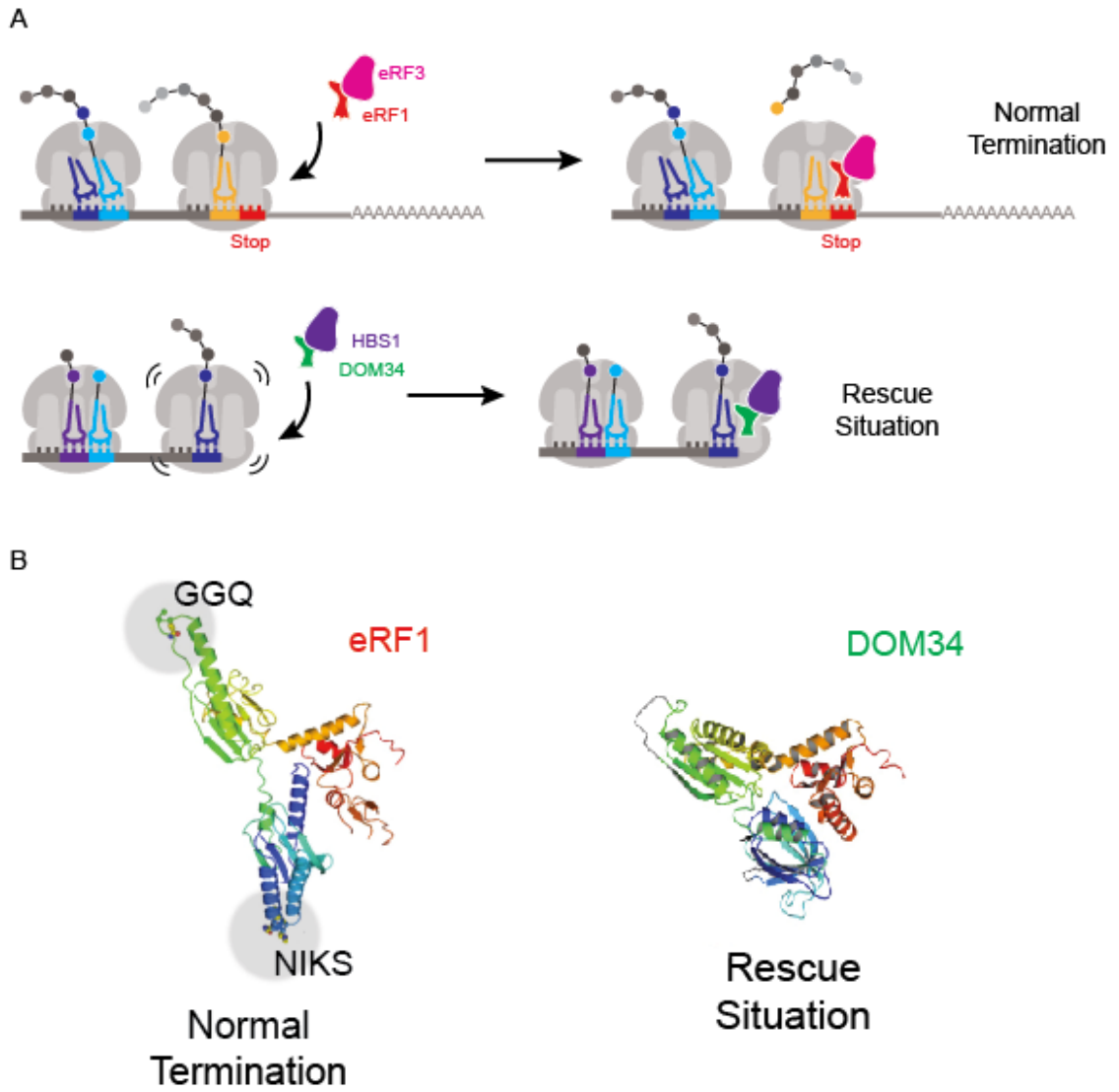


Figure 3

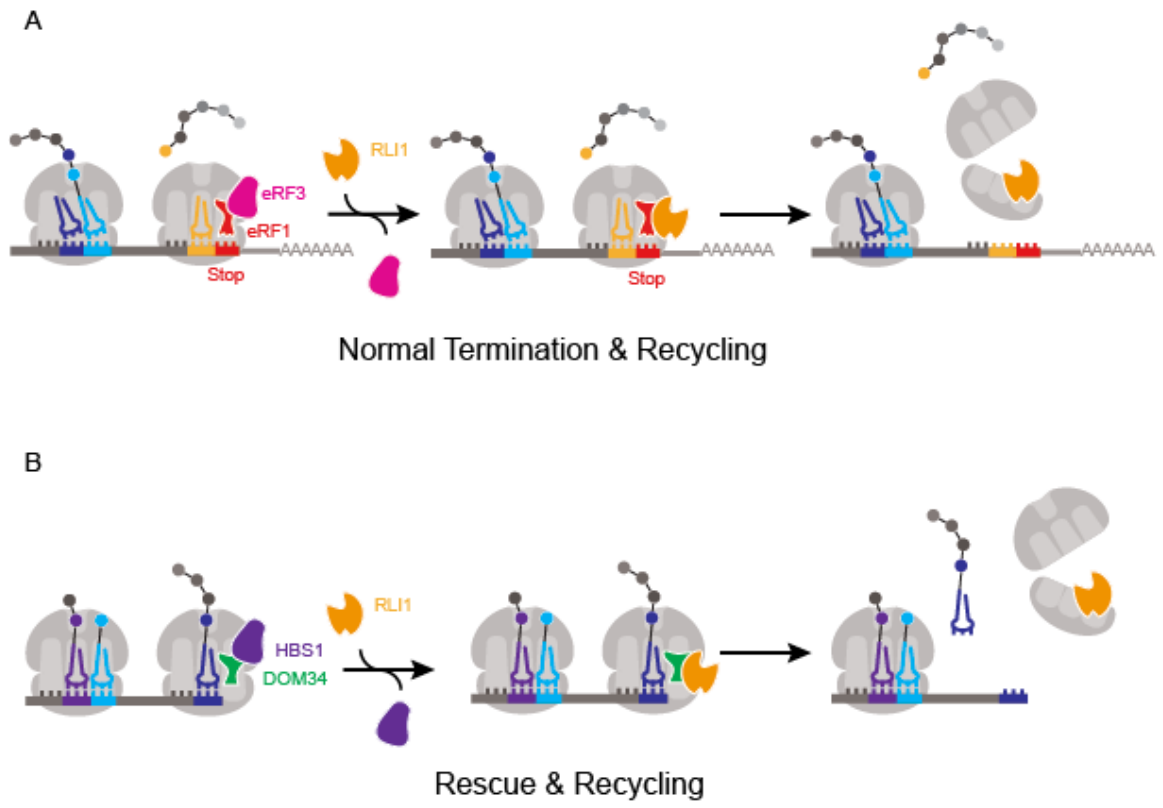


Figure 4

Figure Legends

Figure 1. Overview of eukaryotic translation and specific steps of translation elongation. **(A)** The process of translation begins with initiation through the coordination of many initiation factors (eIFs), initiator Met-tRNA^{iMet}, and the 40S and 60S ribosomal subunits onto the start (AUG) codon of an mRNA. Elongation then allows for individual amino acids to be added to the growing polypeptide chain as the ribosome reads along the mRNA one codon at a time with the help of many elongation factors (eEFs). When the ribosome reaches a stop codon at the end of an open reading frame (ORF) translation is terminated and the peptide is released by the termination factors (eRFs). Finally, the ribosomal subunits must be recycled by the recycling factor RLI1 and returned to the cytoplasm for re-initiation and continued translation of other mRNA transcripts. **(B)** Translation elongation begins after the AUG start codon when next tRNA is decoded and accommodated into the A site of the ribosome by the help of the elongation factor eEF1A and GTP. Peptide transfer (PT) then occurs transferring the growing peptide chain onto the A site tRNA with the addition of the newest amino acid. The tRNAs on the ribosome then enter hybrid E-P, P-A states until the ribosome translocates to the next mRNA codon through the help of the elongation factors eEF2 and eEF3. This then opens the A site of the tRNA for the next round of elongation.

Figure 2. Ribosome stalling during elongation. (A) Schematic of example tRNAs showing canonical Watson-Crick base pairing of the tRNA anti-codon to the mRNA codon as well as wobble decoding when 3' base of the mRNA codon is decoded through non-canonical pairing with the 5' base of the tRNA anticodon. Two common types of wobble decoding are shown G-U and IA. Wobble pairing is depicted by a dot while canonical Watson-Crick decoding is depicted as a line. **(B)** The use of rare codons (red) within the mRNA ORF can lead to slow decoding in the ribosomal A site and lead to ribosome stalling as compared to optimal codons (green). **(C)** Particular codon/tRNA pairs have been shown to cause ribosome stalling when in a certain arrangement (**top**), but are not inhibitory and therefore do not cause stalling in other arrangements (**bottom**).

Figure 3. Canonical translation termination versus ribosome rescue. (A) Top: Canonical termination begins when the ribosome reaches a stop codon within the A site. eRF1 recognizes the stop codon and is accommodated through the GTPase activity of its accessory termination factor eRF3 to coordinate peptide-hydrolysis and release the completely synthesized polypeptide for use in the cell. **Bottom:** When the ribosome translates to the end of a truncated message (or stalling occurs within the ORF during elongation – not depicted) the rescue factor DOM34 binds in the A site of the ribosome with its accessory GTPase HBS1 to signal for the ribosomes to be recycled and the mRNA and polypeptide to be degraded through downstream regulatory pathways. **(B)** Comparison of the termination factor eRF1 with the rescue factor DOM34. eRF1 contains a NIKS motif to specifically recognize the stop codons at the end of ORFs and a catalytic GGQ motif to coordinate the peptide-hydrolysis reaction. DOM34, on the other hand, lacks these motifs, allowing it to recognize sense codons and disabling the coordination of peptide-hydrolysis leaving the peptide bound to the peptidyl tRNA following rescue.

Figure 4. Ribosome recycling following termination or rescue. (A) Following canonical termination by eRF1 and eRF3 at a stop codon at the end of an ORF, the recycling factor RLI1 binds and uses the force generated from the hydrolysis of ATP to separate the small and large subunits. Altogether, termination and recycling result is a full length cleaved polypeptide chain, and recycled 40S and 60S ribosomal subunits for continued translation.

(B) Following rescue by DOM34 and HBS1 on cleaved or stalled mRNAs, the recycling factor RLI1 binds and uses the force generated from the hydrolysis of ATP to separate the small and large subunits. This process results in a released peptidyl tRNA with the growing polypeptide still attached signaling for other regulatory processes to degrade the incomplete polypeptide and mRNA and allow the ribosomal subunits to be used in subsequent rounds of translation.

References

1. Carvalho, M.D., Carvalho, J.F. & Merrick, W.C. Biological characterization of various forms of elongation factor 1 from rabbit reticulocytes. *Archives of biochemistry and biophysics* **234**, 603-611 (1984).
2. Shao, S. *et al.* Decoding Mammalian Ribosome-mRNA States by Translational GTPase Complexes. *Cell* **167**, 1229-561774592 (2016).
3. Zaher, H.S. & Green, R. Fidelity at the Molecular Level: Lessons from Protein Synthesis. *Cell* **136**, 746-762 (2009).
4. Beringer, M. & Rodnina, M.V. The ribosomal peptidyl transferase. *Molecular cell* **26**, 311-321 (2007).
5. Moazed, D. & Noller, H.F. Intermediate states in the movement of transfer RNA in the ribosome. *Nature* **342**, 142-148 (1989).
6. Behrmann, E. *et al.* Structural snapshots of actively translating human ribosomes. *Cell* **161**, 845-857 (2015).
7. Agirrezabala, X. *et al.* Visualization of the hybrid state of tRNA binding promoted by spontaneous ratcheting of the ribosome. *Molecular cell* **32**, 190-197 (2008).
8. Jørgensen, R. *et al.* Two crystal structures demonstrate large conformational changes in the eukaryotic ribosomal translocase. *Nature structural biology* **10**, 379-385 (2003).
9. Spahn, C.M. *et al.* Domain movements of elongation factor eEF2 and the eukaryotic 80S ribosome facilitate tRNA translocation. *The EMBO journal* **23**, 1008-1019 (2004).
10. Taylor, D.J. *et al.* Structures of modified eEF2 80S ribosome complexes reveal the role of GTP hydrolysis in translocation. *The EMBO journal* **26**, 2421-2431 (2007).
11. Ling, C. & Ermolenko, D.N. Structural insights into ribosome translocation. *Wiley interdisciplinary reviews. RNA* (2016).
12. Ermolenko, D.N. & Noller, H.F. mRNA translocation occurs during the second step of ribosomal intersubunit rotation. *Nature structural & molecular biology* **18**, 457-462 (2011).
13. Triana-Alonso, F.J., Chakraborty, K. & Nierhaus, K.H. The elongation factor 3 unique in higher fungi and essential for protein biosynthesis is an E site factor. *The Journal of biological chemistry* **270**, 20473-20478 (1995).
14. Andersen, C.B. *et al.* Structure of eEF3 and the mechanism of transfer RNA release from the E-site. *Nature* **443**, 663-668 (2006).
15. Schuller, A.P., Wu, C.C., Dever, T.E., Buskirk, A.R. & Green, R. eIF5A Functions Globally in Translation Elongation and Termination. *Molecular cell* **66**, 194-20500000 (2017).
16. Schuller, A.P. & Green, R. Roadblocks and resolutions in eukaryotic translation. *Nature reviews. Molecular cell biology* **19**, 526-541 (2018).
17. Agris, P.F. *et al.* Celebrating wobble decoding: Half a century and still much is new. *RNA biology* **15**, 537-553 (2018).
18. Crick, F.H. Codon-anticodon pairing: the wobble hypothesis. *Journal of molecular biology* **19**, 548-555 (1966).
19. Weinberg, D.E. *et al.* Improved Ribosome-Footprint and mRNA Measurements Provide Insights into Dynamics and Regulation of Yeast Translation. *Cell reports* **14**, 1787-1799 (2016).
20. Stadler, M. & Fire, A. Wobble base-pairing slows in vivo translation elongation in metazoans. *RNA (New York, N.Y.)* **17**, 2063-2073 (2011).
21. Sørensen, M.A. & Pedersen, S. Absolute in vivo translation rates of individual codons in Escherichia coli. The two glutamic acid codons GAA and GAG are translated with a threefold difference in rate. *Journal of molecular biology* **222**, 265-280 (1991).
22. Koutmou, K.S., Radhakrishnan, A. & Green, R. Synthesis at the Speed of Codons. *Trends in biochemical sciences* **40**, 717-718 (2015).
23. Plotkin, J.B. & Kudla, G. Synonymous but not the same: the causes and consequences of codon bias. *Nature reviews. Genetics* **12**, 32-42 (2011).
24. Quax, T.E., Claassens, N.J., Söll, D. & van der Oost, J. Codon Bias as a Means to Fine-Tune Gene Expression. *Molecular cell* **59**, 149-161 (2015).

25. dos Reis, M., Savva, R. & Wernisch, L. Solving the riddle of codon usage preferences: a test for translational selection. *Nucleic acids research* **32**, 5036-5044 (2004).
26. Sharp, P.M. & Li, W.H. The codon Adaptation Index--a measure of directional synonymous codon usage bias, and its potential applications. *Nucleic acids research* **15**, 1281-1295 (1987).
27. Dana, A. & Tuller, T. The effect of tRNA levels on decoding times of mRNA codons. *Nucleic acids research* **42**, 9171-9181 (2014).
28. Sabi, R. & Tuller, T. Modelling the efficiency of codon-tRNA interactions based on codon usage bias. *DNA research : an international journal for rapid publication of reports on genes and genomes* **21**, 511-526 (2014).
29. Sabi, R., Volvovitch Daniel, R. & Tuller, T. stAICalc: tRNA adaptation index calculator based on species-specific weights. *Bioinformatics (Oxford, England)* **33**, 589-591 (2017).
30. Chan, P.P.L., T.M., Vol. 37 D93-D97 (Nucleic Acids Research; 2009).
31. Chan, P.P.L., T.M., Vol. 44 D184-D189 (Nucleic Acids Research; 2016).
32. Ikemura, T. & Ozeki, H. Codon usage and transfer RNA contents: organism-specific codon-choice patterns in reference to the isoacceptor contents. *Cold Spring Harbor symposia on quantitative biology* **47 Pt 2**, 1087-1097 (1983).
33. Yu, C.-H.H. *et al.* Codon Usage Influences the Local Rate of Translation Elongation to Regulate Co-translational Protein Folding. *Molecular cell* **59**, 744-754 (2015).
34. Gardin, J. *et al.* Measurement of average decoding rates of the 61 sense codons in vivo. *eLife* **3** (2014).
35. Elf, J., Nilsson, D., Tenson, T. & Ehrenberg, M. Selective charging of tRNA isoacceptors explains patterns of codon usage. *Science (New York, N.Y.)* **300**, 1718-1722 (2003).
36. Chu, D., Barnes, D.J. & von der Haar, T. The role of tRNA and ribosome competition in coupling the expression of different mRNAs in *Saccharomyces cerevisiae*. *Nucleic acids research* **39**, 6705-6714 (2011).
37. Chevance, F.F., Le Guyon, S. & Hughes, K.T. The effects of codon context on in vivo translation speed. *PLoS genetics* **10** (2014).
38. Gutman, G.A. & Hatfield, G.W. Nonrandom utilization of codon pairs in *Escherichia coli*. *Proceedings of the National Academy of Sciences of the United States of America* **86**, 3699-3703 (1989).
39. Gamble, C.E., Brule, C.E., Dean, K.M., Fields, S. & Grayhack, E.J. Adjacent Codons Act in Concert to Modulate Translation Efficiency in Yeast. *Cell* **166**, 679-690 (2016).
40. Dever, T.E. & Green, R. The Elongation, Termination, and Recycling Phases of Translation in Eukaryotes. *Cold Spring Harbor Perspectives in Biology* **4** (2012).
41. Frolova, L. *et al.* Eukaryotic polypeptide chain release factor eRF3 is an eRF1- and ribosome-dependent guanosine triphosphatase. *RNA (New York, N.Y.)* **2**, 334-341 (1996).
42. Kong, C. *et al.* Crystal structure and functional analysis of the eukaryotic class II release factor eRF3 from *S. pombe*. *Molecular cell* **14**, 233-245 (2004).
43. Frolova, L. *et al.* A highly conserved eukaryotic protein family possessing properties of polypeptide chain release factor. *Nature* **372**, 701-703 (1994).
44. Song, H. *et al.* The crystal structure of human eukaryotic release factor eRF1--mechanism of stop codon recognition and peptidyl-tRNA hydrolysis. *Cell* **100**, 311-321 (2000).
45. Brown, A., Shao, S., Murray, J., Hegde, R.S. & Ramakrishnan, V. Structural basis for stop codon recognition in eukaryotes. *Nature* **524**, 493-496 (2015).
46. Alkalaeva, E.Z., Pisarev, A.V., Frolova, L.Y., Kisselev, L.L. & Pestova, T.V. In vitro reconstitution of eukaryotic translation reveals cooperativity between release factors eRF1 and eRF3. *Cell* **125**, 1125-1136 (2006).
47. Salas-Marco, J. & Bedwell, D.M. GTP hydrolysis by eRF3 facilitates stop codon decoding during eukaryotic translation termination. *Molecular and cellular biology* **24**, 7769-7778 (2004).
48. Frolova, L.Y. *et al.* Mutations in the highly conserved GGQ motif of class 1 polypeptide release factors abolish ability of human eRF1 to trigger peptidyl-tRNA hydrolysis. *RNA (New York, N.Y.)* **5**, 1014-1020 (1999).
49. Brandman, O. & Hegde, R.S. Ribosome-associated protein quality control. *Nature structural & molecular biology* **23**, 7-15 (2016).

50. Joazeiro, C.A.P.A.P. Ribosomal Stalling During Translation: Providing Substrates for Ribosome-Associated Protein Quality Control. *Annual review of cell and developmental biology* **33**, 343-368 (2017).
51. Doma, M.K. & Parker, R. Endonucleolytic cleavage of eukaryotic mRNAs with stalls in translation elongation. *Nature* **440**, 561-564 (2006).
52. Carr-Schmid, A., Pfund, C., Craig, E.A. & Kinzy, T.G. Novel G-protein complex whose requirement is linked to the translational status of the cell. *Molecular and cellular biology* **22**, 2564-2574 (2002).
53. Chen, L. *et al.* Structure of the Dom34-Hbs1 complex and implications for no-go decay. *Nature structural & molecular biology* **17**, 1233-1240 (2010).
54. Graille, M., Chaillet, M. & van Tilbeurgh, H. Structure of yeast Dom34: a protein related to translation termination factor Erf1 and involved in No-Go decay. *The Journal of biological chemistry* **283**, 7145-7154 (2008).
55. Lee, H.H. *et al.* Structural and functional insights into Dom34, a key component of no-go mRNA decay. *Molecular cell* **27**, 938-950 (2007).
56. Shoemaker, C.J., Eyler, D.E. & Green, R. Dom34:Hbs1 Promotes Subunit Dissociation and Peptidyl-tRNA Drop-Off to Initiate No-Go Decay. *Science* **330**, 369-372 (2010).
57. Guydosh, N.R. & Green, R. Dom34 rescues ribosomes in 3' untranslated regions. *Cell* **156**, 950-962 (2014).
58. Guydosh, N.R. & Green, R. Translation of poly(A) tails leads to precise mRNA cleavage. *RNA (New York, N.Y.)* **23**, 749-761 (2017).
59. Tsuboi, T. *et al.* Dom34:hbs1 plays a general role in quality-control systems by dissociation of a stalled ribosome at the 3' end of aberrant mRNA. *Molecular cell* **46**, 518-529 (2012).
60. Pisarev, A.V. *et al.* The role of ABCE1 in eukaryotic posttermination ribosomal recycling. *Molecular cell* **37**, 196-210 (2010).
61. Shoemaker, C.J. & Green, R. Kinetic analysis reveals the ordered coupling of translation termination and ribosome recycling in yeast. *Proceedings of the National Academy of Sciences* **108** (2011).
62. Preis, A. *et al.* Cryoelectron microscopic structures of eukaryotic translation termination complexes containing eRF1-eRF3 or eRF1-ABCE1. *Cell reports* **8**, 59-65 (2014).
63. Heuer, A. *et al.* Structure of the 40S-ABCE1 post-splitting complex in ribosome recycling and translation initiation. *Nature structural & molecular biology* **24**, 453-460 (2017).
64. Andersen, D.S. & Leever, S.J. The essential Drosophila ATP-binding cassette domain protein, pixie, binds the 40 S ribosome in an ATP-dependent manner and is required for translation initiation. *The Journal of biological chemistry* **282**, 14752-14760 (2007).
65. Chen, Z.-Q.Q. *et al.* The essential vertebrate ABCE1 protein interacts with eukaryotic initiation factors. *The Journal of biological chemistry* **281**, 7452-7457 (2006).
66. Dong, J. *et al.* The essential ATP-binding cassette protein RL11 functions in translation by promoting preinitiation complex assembly. *The Journal of biological chemistry* **279**, 42157-42168 (2004).

Chapter 2: Molecular mechanism of translational stalling by inhibitory codon combinations and poly(A) tracts

Note: This chapter was published on BioRxiv and submitted to The EMBO Journal on September 2, 2019.

Abstract

Inhibitory codon pairs and poly(A) tracts within the translated mRNA cause ribosome stalling and reduce protein output. The molecular mechanisms that drive these stalling events, however, are still unknown. Here, we use a combination of *in vitro* biochemistry, ribosome profiling, and cryo-EM to define molecular mechanisms that lead to these ribosome stalls. First, we use an *in vitro* reconstituted yeast translation system to demonstrate that inhibitory codon pairs slow elongation rates which are partially rescued by increased tRNA concentration or by an artificial tRNA not dependent on wobble base pairing. Ribosome profiling data extend these observations by revealing that paused ribosomes with empty A sites are enriched on these sequences. Cryo-EM structures of stalled ribosomes provide a structural explanation for the observed effects by showing decoding-incompatible conformations of mRNA in the A sites of all studied stall-inducing sequences. Interestingly, in the case of poly(A) tracts, the inhibitory conformation of the mRNA in the A site involves a nucleotide stacking array. Together, these data demonstrate novel mRNA-induced mechanisms of translational stalling in eukaryotic ribosomes.

Introduction

Coding sequences for proteins in any genome (the open reading frames or ORFs) have evolved in the context of their full mRNA transcript to be expressed at the appropriate level. Interestingly, synonymous codon choice has been shown to have broad impacts on many aspects of translation including translational efficiency^{1, 2}, mRNA decay³ and cotranslational protein folding^{4, 5}. The effects on translational efficiency are primarily mediated through the competition of cognate and near-cognate tRNA interactions, as dictated by the pool of charged tRNAs available in the cell^{1, 6, 7}. Individual codons that are generally decoded by more abundant tRNAs and are associated with increased translation efficiency have been defined as “optimal”⁸⁻¹⁰. Moreover, codon usage biases, codon context and interactions between adjacent codons have all been suggested to play a role in translational efficiency^{11, 12}, though their direct effects on elongation are still not fully understood.

A recent study in yeast defined a collection of 17 specific codon pairs that caused a substantial down-regulation in protein output¹³. For 12 of these pairs, the order of the codons within the pair was critical for the observed inhibition. Despite the diverse nature of these pairs, there were some shared features. First, the proline codon CCG and the arginine codon CGA appeared frequently in the collection of inhibitory pairs. The CCG codon is decoded by a G-U wobble base pair while the CGA codon is the sole codon in yeast decoded by an obligate I:A wobble pair¹⁴. Notably, while the previous study¹³ concluded that these inhibitory codon pairs likely impacted the decoding step of elongation, there was little understanding of the molecular basis for these events.

Besides inhibitory codon pairs, poly(A) tracts represent perhaps the most abundant and potent stall-inducing mRNA sequence in eukarya (reviewed in ¹⁵. Translation of poly(A) sequences commonly occurs when ribosomes encounter an abnormal (premature) polyadenylation event within the ORF or when ribosomes read through a stop codon. Premature polyadenylation alone occurs in approximately 1% of yeast and human transcripts, highlighting the importance of this mechanism ^{16, 17}. While translation of poly(A) tracts initially results in the synthesis of poly-lysine, long poly(A) tracts subsequently trigger quality control pathways that contribute to overall protein homeostasis ^{18,19}. The earliest studies suggested that this stalling was caused by electrostatic interactions between the poly-basic nascent chain and the peptide exit tunnel of the ribosome ²⁰. However, there are several lines of evidence suggesting that the stalling mechanism of poly(A) tracts is more complex. Interestingly, as few as two consecutive AAA codons were shown to cause ribosome sliding during translation in *E. coli* ²¹. Moreover, the identity of the basic residue-encoding codon is of particular importance for efficient stalling, as the CGA arginine-encoding codon is most potent in yeast ²², and AAA codons are more potent than AAG lysine-encoding codons at inducing translational stalling ^{21,23}.

All of the inhibitory sequences described above result in partial or complete translational stalling *in vivo*. Considerable attention has been paid to the molecular consequences of the translating ribosomes encountering such mRNA sequences (i.e. the downstream quality control events that are triggered). In particular, recent work has suggested that ribosomal collisions with the leading, stalled ribosome are a key event that triggers the quality control responses that include decay of the mRNA (“No Go Decay” or NGD) and the nascent peptide (Ribosome-associated Quality Control or RQC) ²⁴⁻²⁶.

However, there has been little characterization of the molecular events on the ribosome that lead to such dramatic outcomes.

Here we use a yeast *in vitro* reconstituted biochemical system to directly measure the rates of translation elongation that might be impacted by inhibitory codon pairs and poly(A) tracts. Use of this *in vitro* system allows for ready manipulation of mRNA coding sequence, tRNA identity and concentration, as well as ribosome composition to reveal defects in the individual steps of translation elongation. Together with high-resolution ribosome profiling, our results reveal clear defects in the decoding step as the primary determinant of ribosomal stalling on these inhibitory mRNA sequences. Cryo-EM structures of ribosome complexes stalled at these mRNA sequences reveal detailed insight into the molecular basis for the translational stalling. Importantly, we observe decoding-incompetent conformations of mRNA in the A sites of all stall-inducing sequences that we studied, thus readily explaining the biochemically-defined decoding defects. Moreover, structural characterization of poly(A) stalled disomes reveals a novel disome conformation with both ribosomes in the POST translocation state, suggesting a role for ribosome collisions in promoting frameshifting. Taken together, our data reveal an mRNA-induced translational stalling mechanism of eukaryotic ribosomes.

Results

Inhibitory codon pairs slow elongation *in vitro*

To examine the impact of inhibitory codon pairs on translation elongation *in vitro*, we selected pairs that most potently reduced GFP expression in the *in vivo* experiments and those that contained codons which appeared in multiple inhibitory pairs (Fig 1A)¹³.

The strongest candidates were CGA-CGA and CGA-CCG encoding Arg-Arg and Arg-Pro, respectively. The arginine codon CGA is decoded by ICG tRNA^{Arg} where inosine forms a unique purine-purine I:A wobble pair. The proline codon CCG is found in many inhibitory codon pairs, likely because it is decoded by tRNA using a G-U wobble pair, UGG tRNA^{Pro} (Fig 1A). The prevalence of and dependency on wobble base-pairing in inhibitory codon pairs led Grayhack and co-workers to conclude that elongation is blocked by non-optimal codon-anticodon pairing at neighboring sites on the ribosome (i.e. the P and A sites). Furthermore, they showed that for these codon pairs, the order of the codons in the pair is critical; the reverse pair has little to no effect on protein output.

To monitor synthesis of tetrapeptides containing these inhibitory codon pairs, we employed an *in vitro* reconstituted yeast translation system^{27,28}. Initiation complexes (ICs) were assembled using ribosome subunits, [³⁵S]-Met-tRNA^{iMet}, and mRNAs containing an AUG codon, the codon pair of interest, and an additional codon encoding Phe or Lys before or after the pair to enhance visualization of the products by electrophoretic thin-layer chromatography (eTLC). Following purification, each IC was treated with puromycin (Pm) to release the nascent chain and determine the fraction of bound [³⁵S]-Met-tRNA^{iMet} that forms Met-Pm. Puromycin reacts with peptidyl-tRNA bound to the ribosome when the peptidyl-transferase center (PTC) of the large subunit is accessible and releases the polypeptide chain as peptidyl-puromycin. As such, this assay reports on the overall competence and conformation of the peptidyl-transferase center of the ICs. We consistently observed that ICs formed with the different mRNA transcripts formed Met-Pm products to a similar extent (Fig EV1A). Therefore, differences in the amount of peptide produced

using ICs containing different mRNA templates were not due to the efficiency of IC formation or to the differential ability of the programmed ribosome to make peptide bonds.

For elongation reactions, the desired tRNAs were purified from bulk tRNA using biotinylated oligonucleotides ²⁹, charged with the corresponding aminoacyl-tRNA synthetase, and the aminoacyl-tRNAs were pre-incubated with eEF1A and GTP to form ternary complexes. Ternary complexes were then mixed with purified ICs and elongation factors eEF2, eEF3, and eIF5A. Peptide formation was monitored by quenching time points of the reactions in KOH and resolving the formed products by eTLC (Fig 1A). The initial experiments were performed with ribosome complexes at ~2 nM and aa-tRNAs at ~12 nM, where both binding and catalysis contribute to the observed rate (i.e. k_{cat}/K_m conditions). For each inhibitory codon pair a control “optimal” IC was prepared where the non-optimal codons were replaced by synonymous codons that are decoded by the same tRNA, but without wobble base pairing. For example, the optimal codon CGC was used as a control for CGA because it is decoded by the same ICG tRNA^{Arg} via a pyrimidine-purine C:I pair with a standard Watson-Crick geometry ³⁰ instead of a purine-purine (A:I) wobble base pair (Fig 1A).

Visual examination of the reaction profiles for the inhibitory CGA-CGA codon pair (in red) relative to the optimal CGC-CGC codon pair (in green) reveals a clear defect in elongation (Fig 1B). First, the inhibitory Arg-Arg pair exhibits a significantly lower endpoint, with ~25% of the radiolabeled Met forming the final tetrapeptide product, MFRR, compared with ~45% for the optimal Arg-Arg sequence. In a similar fashion, there are clear elongation defects for the inhibitory Arg-Pro, CGA-CCG codon pair (in red) compared to the optimal CGC-CCA codon pair (in green) (Fig 1C); the inhibitory Arg-Pro

pair has only ~20% of the radiolabeled Met forming the final tetrapeptide product, MRPK, compared to ~50% for the optimal Arg-Pro sequence. As endpoint defects often suggest the existence of an off pathway reaction, we asked whether there were high levels of peptidyl-tRNA drop-off during elongation for the Arg-Arg or Arg-Pro reactions that might explain the observed defects. However, when we directly tested this possibility using an assay involving peptidyl hydrolase (Pth) that acts only on tRNAs not bound to the ribosome, we saw no evidence for drop off with any of the complexes (Fig EV1B, C)^{28,31}.

In addition to the endpoint defects, we also observe a reduced rate of formation of the final peptide product for the complexes encoding both the Arg-Arg and Arg-Pro pairs; in each case, the observed rates were about three-fold slower than those of their optimal counterparts (Fig 1B, C). For the Arg-Arg pair, where MFR and MFRR can be separately resolved, we see a substantial build-up of MFR intermediate peptide relative to the CGC-CGC dicodon control (Figs 1B and EV1D). Quantification of both products (MFR and MFRR) of this inhibitory pair as well as elongation on a single arginine message (MFR) indicate that elongation through the first CGA codon is slightly slow, but that the subsequent elongation through the second CGA codon is the major inhibitory step (Figs EV1E, F).

Together, these data reveal *in vitro* defects in elongation reactions on the ribosome resulting from two distinct inhibitory codon pairs. These observations provide strong evidence that the initially observed effects *in vivo*¹³ reflect defects intrinsic to ribosome function rather than resulting from mRNA decay or other downstream cellular events.

Multiple defects in decoding caused by codon pairs

Assuming that one likely cause of elongation slow-down may be defects in decoding, we asked if the inhibition arises from simple defects in the energetics of tRNA binding (a second order event) or instead from more downstream defects (i.e. in first order events) that follow including GTPase activation and accommodation^{32,33}. As the initial *in vitro* experiments were performed in a k_{cat}/K_m regime, we repeated the elongation assays at 10-fold higher ternary complex concentrations. For Arg-Arg, we see an approximately 2-fold rescue of the rate of the reaction with higher tRNA concentrations for the inhibitory pair (CGA-CGA) with only very modest changes in the rate of the reaction for the optimal pair (CGC-CGC) (Fig 2A, left). Similarly, for the Arg-Pro combination, we see an approximately 4-fold increase in the rate of the reaction with higher tRNA concentrations for the inhibitory pair (CGA-CCG) with only a modest, maximally 1.5-fold increase, for the optimal pair (CGC-CCA) (Fig 2A, right). These results suggest that tRNA binding contributes in part to the observed defects seen for the inhibitory pairs. Importantly, however, we observe that for both codon pairs (CGA-CGA and CGA-CCG), the endpoint defects are not overcome at high tRNA concentrations (Fig 2B). These latter data strongly suggest that a certain fraction of the complexes is unable to elongate independent of saturating levels of aminoacyl-tRNA substrate.

Given the unusual nature of the I:A wobble base pair found in the P site after incorporation of the first Arg in the codon pair, we also wondered whether the substantial defects that we observed might be rescued with the use of a non-natural, exact match UCG tRNA^{Arg} as shown *in vivo* in the previous study¹³. We expressed the non-natural tRNA^{Arg} on a CEN plasmid in yeast and purified it as above using a biotinylated oligonucleotide. In

elongation reactions performed under k_{cat} conditions (high tRNA concentrations), this non-natural tRNA did partially rescue the endpoint defects in the elongation reaction associated with the CGA-CGA codon pair (Fig 2C); these data suggest that the unusual I:A pairing in the P site at least partially contributes to the endpoint defects associated with these inhibitory codon pairs.

Increased 21 nt RPFs on inhibitory pairs indicate an empty ribosomal A site

To further investigate the molecular mechanisms of inhibition underlying the inhibitory codon pairs, we turned to high-resolution ribosome profiling³⁴. We recently reported that ribosome profiling using a cocktail of elongation inhibitors can trap ribosomes in their different functional states, distinguished by the size of ribosome protected footprints (RPFs). For example, when cycloheximide (CHX) and tigecycline (TIG) are added to yeast lysates to prevent ribosomes from translating post cell lysis, RPFs that are 21 nucleotides (nts) in length correspond to ribosomes in a “classical” or POST state waiting to decode the next aminoacyl-tRNA while RPFs that are 28 nts in length correspond primarily to ribosomes trapped in a “rotated” or PRE state³⁴. Building on an earlier study that showed an enrichment in ribosome density when the 17 inhibitory codon pairs are aligned^{13,35}, we generated libraries using CHX and TIG to better distinguish the functional state of the paused ribosomes. In the plot shown in Fig 3A, the average ribosome density on 17 inhibitory codon pairs (with the first codon in the P site and second in the A site) is shown as a function of the RPF length on the Y-axis. We observe that while the density of 28 nt RPFs is fairly constant across this region, there is a large accumulation of 21 nt RPFs at the A site codon (Fig 3A). These data indicate that for these 17 inhibitory

pairs, elongation inhibition is likely caused by slow decoding of the second codon of the inhibitory pair, resulting in an empty A site that yields shorter footprints.

We can also look individually at the representative codon pairs studied above (CGA-CGA and CGA-CCG) and we see significant accumulation of 21 nt RPFs in the A site relative to the amount observed for their optimal counterparts (red vs. green) (Fig 3B). These data provide direct evidence that elongation inhibition on these codon pairs results from slow decoding of the second codon of the inhibitory pair.

We also considered the possibility that for the inhibitory codon pairs, tRNAs are accommodated but fail to undergo peptidyl transfer, perhaps because of a misalignment in the active site of the 60S subunit. We observed previously that the addition of anisomycin (ANS), a peptidyl-transferase inhibitor, together with CHX, blocks bound tRNAs from forming peptide bonds such that they eventually fall out of the A site; in these libraries, 21 nt RPFs represent two different ribosome populations, those in a pre-accommodation and a pre-peptidyl transfer state. Indeed, in samples prepared with CHX/ANS, we observe more 21 nt RPFs at peptide motifs known to undergo slow peptidyl transfer²⁸ relative to those motifs or codons enriched in the CHX/TIG samples (Fig EV2A). If the chemistry of peptide-bond formation were slow for the inhibitory codon pairs, we would expect to see an increase of 21 nt RPFs at these sites in the CHX/ANS library relative to the CHX/TIG library. Instead, we see the same level of enrichment of 21 nt RPFs at these sites (Fig 3C, left), arguing that the limiting step for the inhibitory base pairs is not peptide bond formation. These findings are consistent with the hypothesis that certain wobble pairs impact the decoding center in the 40S subunit, affecting decoding or accommodation, rather than activities in the peptidyl-transferase center of the large subunit. For the optimal

codon pairs for these same amino acid sequences, no pauses are seen in either sample indicating that the pausing at inhibitory codons is due to the codon/tRNA pairing in the A site rather than to the amino acid sequence (Fig 3C, right).

Loss of the ribosomal protein Asc1 inhibits elongation

Several studies in yeast using iterated CGA codons to induce ribosome stalling have shown that the loss of the ribosomal protein Asc1 enables ribosomes to read through these inhibitory sequences^{22, 36, 37}; these data suggest that Asc1 is somehow involved either in facilitating proper decoding or in sensing and stabilizing stalled ribosomes. We asked what role Asc1 plays in the elongation of CGA codon pairs using our *in vitro* system. We first prepared ribosomes from an Asc1 deletion strain and produced initiation complexes programmed with either non-optimal (CGA-CGA) or optimal (CGC-CGC) MFRR mRNAs as before and compared their elongation reactions. Initiation complex formation and the puromycin reactivity of these complexes was indistinguishable from that of complexes formed with wild-type ribosomes (Fig EV3A). Elongation reactions were then performed as described above using ICG tRNA^{Arg} to decode the Arg codons in both mRNAs. We see that for both the inhibitory and optimal di-codon pair complexes, ribosomes lacking Asc1 elongate more slowly and reach a lower elongation endpoint (Fig 4A). These data suggest that ribosomes lacking Asc1 have general defects in elongation. Elongation reactions with ICs lacking Asc1 for the CGA-CCG, Arg-Pro pair show similar defects (Fig EV3B). We also performed high-resolution ribosome profiling in an *asc1Δ* strain using CHX/TIG for the preparation as above³⁴. In this analysis, we observe a genome-wide increase of 21 nt RPFs, consistent with the idea that ribosomes lacking Asc1

broadly struggle with the tRNA decoding step of translation elongation (Fig 4B). Moreover, when we specifically look at the pausing signature of ribosomes at the 17 inhibitory codon pairs, we see that the CGA-CCG and CGA-CGA codon pairs show the largest enrichment in 21 nt RPFs in the *asc1* deletion strain compared to the wild-type strain (Fig 4C). Together, these data provide support for the idea that the ribosomal protein Asc1 makes important contributions to the tRNA selection step of translation elongation.

Decoding-incompatible mRNA conformation causes to inhibitory codon pair-mediated stalling

To investigate the molecular basis of the inhibitory codon pairs involving the problematic CGA codon, we turned to structural studies of complexes stalled at CGA-CCG and CGA-CGA codon pairs. We used a yeast cell-free *in vitro* translation system in which we translated mRNA reporters containing the CGA-CCG or CGA-CGA inhibitory codon pairs. Translation extracts were prepared from yeast cells lacking Ski2p, a component of the 3'-5' mRNA decay system, to enhance mRNA stability. Both mRNA reporters contained sequences coding for an N-terminally His₈-HA-tagged truncated uL4³⁸ followed by the stalling (CGA-CCG)₂ or (CGA-CGA)₂ codon pairs (Appendix Figs S1A, S2A). To avoid capturing read-through products, the stalling sequences were followed by three UAA(A) stop codon quadruplets, one in each reading frame, which would lead to termination upon read-through. Ribosome nascent chain complexes (RNCs) were affinity purified using magnetic beads, separated on a sucrose density gradient and the 80S fractions were subjected to cryo-EM (Appendix Figs S1, S2).

Classification of ribosomal particles for both stalling sequences (CGA-CCG and CGA-CGA) revealed the most abundant classes to be programmed ribosomes in the post-translocation state (POST state) with tRNAs in the P/P and E/E state, but not in the A site (Appendix Figs S3, S4). The structure of the CGA-CCG stalled ribosome was reconstructed to an average resolution of 2.6 Å while the CGA-CGA stalled ribosome was reconstructed to an average resolution of 3.2 Å (Fig EV4B, C). To compare these structures on a molecular level with a canonical A site tRNA decoding situation, we refined our previously produced structure of cycloheximide-stalled ribosomes in the pre-translocation state (PRE state) with A/A and P/P tRNAs to 3.1 Å with focus on the mRNA decoding in the A site (Figs 5A and EV4A) (Buschauer et al. 2019). Molecular models were built and refined for all structures allowing for an in-depth analysis (Fig 5A-I). Structural analysis of the CGA-CCG and the CGA-CGA stalled RNCs revealed no perturbations of the peptidyl-transferase center (PTC), in agreement with the puromycin reactivity of these stalled ribosomes (Appendix Fig S5). On the other hand, we saw a strikingly unusual conformation of the mRNA in the A site of these structures when compared with the canonical decoding situation (Fig 5A-I).

The most striking mRNA structure is formed on the CGA-CCG reporter mRNA. In our 2.6 Å map, we can clearly identify the CGA-codon in the P site and the anticodon of ICG tRNA^{Arg} making standard Watson-Crick interactions as observed before³⁹ at the first two positions of the codon and a purine:purine A:I base pair at the wobble position (Fig 5E). However, the first nucleotide in the A site (the C+4 of the CCG codon) is found in an unusual conformation that is well defined by the cryo-EM density (Fig EV5A). Compared to the control canonical decoding situation (Fig 5A-C), C+4 is flipped by approximately

95° degrees towards the wobble A:I base pair in the P site. Stabilization of C+4 in this position appears to be facilitated by an H-bond formed with C1637 of 18S rRNA helix 44 (C1400 in *E. coli*) which stacks on the I of the ICG tRNA^{Arg} in the P site (Fig 5F). Compared to the canonical decoding situation, accommodation of the purine:purine A:I wobble base pair at position +3 shifts the mRNA backbone by 2.6 Å at the phosphate linking +3 and +4, thus forcing the general path of the downstream mRNA into an unusual direction (Fig EV5B, C). Importantly, this alteration in the mRNA structure moves the crucial A/P kink to occur between positions +4 and +5 (Fig 5F). The A/P kink, normally positioned between positions +3 and +4, was shown to be crucial for A site interaction and proofreading activity, especially for difficult-to-decode near cognate tRNAs⁴⁰. In the flipped-out position seen here, the C+4 seems unlikely to be engaged by a canonical codon:anticodon interaction with the incoming aminoacyl-tRNA (Fig 5C). This rearrangement of the mRNA itself could explain the previously proposed communication between ribosomal P and A sites¹³.

Moreover, following C+4, the mRNA folds into a stable mRNA hairpin structure that directly occludes tRNA binding in the A site. In the hairpin, the C+5 base pairs with G+12 and the G+6 base pairs with C+11, while nucleotides C+7 – C+10 form a rather flexible tetraloop at the tip of the hairpin (Fig EV5D, E). Interestingly, this structure is stabilized by A1756 (A1493 in *E. coli*) of the 18S rRNA which flips out of helix h44 as well as the rearranged A2256 (A1913 in *E. coli*) of the 25S rRNA helix 69. Normally, A2256 forms a dynamic inter-subunit bridge 2A by intercalating into the 18S rRNA helix 44. However, to support the observed mRNA secondary structure formation, A2256 rotates by 101 degrees and stacks with C+7 of the mRNA (Fig EV5E). Taken together, this

structure rationalizes how accommodation of the UGG-tRNA^{Pro} in the A site on the CGA-CCG inhibitory dicodon is prevented: i) by positioning of C+4 in a conformation incompatible with decoding, ii) by shifting the crucial mRNA A/P kink one position downstream and iii) by sterically blocking the tRNA binding site with an mRNA secondary structure.

Analogous to the CGA-CCG situation, we saw a specific inhibitory conformation of C+4 in the CGA-CGA mRNA cryo-EM structure (Fig 5G-I). Again, well supported by cryo-EM density, the conformation of C+4 is essentially the same as observed for the CGA-CCG reporter, with an 84° rotation of the cytosine base (Figs 5I and EV5F). After position +4, however, the mRNA density is weak and does not allow for reliable model building. These observations suggest a more flexible conformation of downstream mRNA in this structure. Nonetheless, the general path of mRNA seems to be shifted in the same direction as seen for the CGA-CCG case and the A/P kink in mRNA is also dislocated downstream as it cannot be observed between positions +3 and +4 (Figs 5I and EV5C). Taken together, these two structures show how rearrangement of the mRNA induced by the wobble-decoded CGA codon in the P site causes perturbations in the A site that disfavor decoding.

Decoding-incompatible mRNA conformation contributes to poly(A) tract-mediated stalling

Next, we wondered whether the CGA-dependent codon pair stalling mechanism is structurally related to poly(A)-mediated stalling. First, using our *in vitro* system, we see slower elongation on a MFK₅ AAA IC as compared to an AAG IC, consistent with earlier observations in *E. coli*²¹. Despite resolution limitations of eTLC with multiple lysines,

when we compare the earliest time points for AAA complexes with those for AAG complexes, the AAA complexes have only elongated to MF and MFK, whereas the AAG complexes are already making MK₂ and larger products as indicated by the fast running smear (Fig EV6). These data are consistent with earlier reports documenting differences in elongation on iterated AAA relative to AAG lysine codons in other systems^{21,23}.

For cryo-EM, we used an analogous approach to that used for CGA-dependent codon pair-mediated stalling with a modified mRNA reporter comprising a 49 nucleotide long poly(A) tract (Appendix Fig S6). As for both inhibitory codon pairs (CGA-CCG and CGA-CGA) discussed above, classification of poly(A) stalled ribosomal particles revealed that a majority (78%) of programmed particles are in the POST state without A-site tRNA (Appendix Fig S7). We reconstructed the poly(A)-stalled ribosome structure to an overall resolution of 3.1 Å, which allowed for building and refinement of a molecular model (Fig 6A, B).

In the resulting structure, we first analyzed the PTC to look for potential structural changes that might rationalize previous arguments that sequential lysines in the peptide tunnel lead to translational stalling due to their basic nature²⁰. We were able to model the last three C-terminal residues of the nascent chain as lysines, consistent with the RNC being stalled on the poly(A) tract. In the PTC we observed the terminal lysine side chain pointing towards the A site and an extra density not explained by the nascent peptide model (Fig 6C). Overall, however, the crucial catalytic bases (U2875 and U2954) did not seem to be hindered from moving into the induced state conformation upon tRNA binding in the A site, therefore hinting that any perturbations of the PTC geometry are relatively modest. Consistent with this hypothesis, these complexes are reactive to puromycin (data not

shown). Moreover, these observations do not provide an explanation for the absence of A site tRNA in 93% of particles. Therefore, we investigated the mRNA conformation in the A site decoding center.

When we examined the molecular details in the decoding center, we clearly saw the structure of the codon-anticodon interaction between the AAA codon and UUU tRNA^{Lys} in the P site with no apparent perturbations (Fig 6D). Strikingly, however, the four downstream adenosines in the A site decoding center are engaged in a π -stacking array, adopting essentially the same single stranded helical conformation recently reported by Passmore and colleagues for isolated poly(A) sequence⁴¹. This +4 to +7 π -stack is stabilized on both sides by flipped out rRNA nucleotides A1756 and C1634. Indeed, C1634 (C1397 in *E. coli*) is found in an unusual, previously unobserved conformation (Fig 6E, F). In this arrangement, the AAA codon in the A site adopts what is clearly a decoding-incompetent conformation that likely directly contributes to poly(A) mediated stalling, although the general path of mRNA does not seem to be as strongly affected as in the case of both inhibitory codon pairs (Fig EV5C). Taken together, for RNCs stalled on poly(A), we observe structural changes assumed by the mRNA in the A site that preclude canonical interactions with the decoding tRNA.

Ribosome collisions on poly(A) tracts affect disome formation

Given that ribosome collisions have been shown to produce crucial substrates for quality control pathways^{26, 42, 43}, we wondered if poly(A) tracts in our system would generate a stable ribosome collision amenable to structural analysis. Therefore, we prepared a disome fraction of the poly(A) stalled RNCs as a minimal ribosome collision

species and determined structural information by cryo-EM (Appendix Fig S6). We processed the data using the 80S extension approach as described previously⁴³ and segregated classes of ribosomal particles stalled in the POST and PRE states (Appendix Fig S9). When we further sorted particles corresponding to the above described poly(A) stalled 80S POST state class, we observed disome structures as expected, however, these POST state ribosomes were found in both the first “stalled” as well as the second “colliding” positions. These collided disomes, which were composed of two POST state ribosomes, are thus strikingly different from previously characterized disomes in both mammalian and yeast systems^{42, 43}. In these previous structures, the second colliding ribosome was always present in a rotated PRE state, with tRNAs in the A/P and P/E states unable to translocate any further downstream. We refined the disome class containing the colliding 80S in the POST state to an overall resolution of 3.8 Å and clearly confirmed that both individual 80S ribosomes are present in the canonical POST state conformation in this disome assembly (Fig 7A–C). Direct comparison of POST-POST with the POST-PRE disome assemblies showed that the second colliding ribosome would have to rotate by 16° to structurally mimic the previously reported POST-PRE conformation (Fig 7D). Taken together, these data indicate that the second colliding ribosome is able to complete the translocation step along the mRNA, a step that would normally be prevented by the stable “roadblock” of the leading stalled ribosome. Therefore, we suggest that poly(A) tracts, which are known to be slippery and allow for sliding, can result in a less rigidly arrested first stalling ribosome.

Discussion

Gene expression can be fine-tuned by the selection of specific codons within the context of the degeneracy of the genetic code. While traditional metrics like the codon adaptation index or tRNA adaptation index take into account how commonly a codon is used or how abundant its cognate tRNA is, respectively, it is not well understood why specific codon pairs are underrepresented in genomes compared to their expected values based on the frequency of each individual codon in the pair^{44, 45}. The work of Grayhack and co-workers¹³ identified 17 codon pairs in *S. cerevisiae* that reduce protein expression, offering experimental insights into how codon pairs affect translation. In particular, they showed that tRNAs in neighboring ribosomal A and P sites can interact to limit protein output in a codon pair-mediated way, and hypothesized that wobble base pairing played a role in this inhibition.

Our results with an *in vitro* reconstituted translation system directly show that elongation rates of inhibitory codon pairs are slower than those of their optimal counterparts, confirming the hypothesis that inhibition is intrinsic to the ribosome and is likely to involve interactions with the tRNA substrates. For both the Arg-Arg (CGA-CGA) and Arg-Pro (CGA-CCG) pairs, strong defects in the rates and endpoints of the reactions are observed (Figs 2A and B). The observation that the strong endpoint defects are not affected by increased tRNA concentration suggests that there are fundamental structural defects that preclude A site binding/reactivity for some fraction of the ribosome complexes. Consistent with previous work by Grayhack and co-workers¹³, the unique I-A wobble associated with decoding CGA codons by the ICG tRNA^{Arg} has a strong effect on

interactions in the P site that structurally extend into perturbations of the A site (Figs 5F, I). We additionally find that these defects are partially rescued by substitution of a UCG tRNA^{Arg} that no longer relies on I:A pairing (Fig 2C), consistent with previous *in vivo* studies¹³.

The observation that the kinetics of decoding are retarded by inhibitory codon pairs in biochemical assays was corroborated by our high resolution ribosome profiling studies. We see an enrichment of 21 nt RPFs, corresponding to ribosomes lacking a tRNA in the A site, when the first codon of the pair is in the ribosomal P site and the second codon is in the A site (Fig 3A and B). Comparing the results from the CHX/ANS library with the CHX/TIG library, we see the same level of these 21 nt RPFs, indicating that peptide bond formation is not limiting the inhibitory codon pair-stalled ribosomes (Fig 3C). This observation is consistent with the fact that the optimal codon pairs (which encode the same amino acid residues and use the same tRNAs) elongate at normal rates both *in vivo* and *in vitro*. These data indicate that the inhibitory codon pairs affect the decoding center of the 40S subunit rather than the peptidyl-transferase center of the 60S subunit. Overall, our data are consistent with the idea that the major mechanism of inhibition on most of these inhibitory codon pairs is through impairment of tRNA binding/accommodation.

Previous studies argue that ribosomes lacking the ribosomal protein Asc1 are able to readthrough CGA-CGA codons, thus effectively increasing protein output^{22, 36, 37}. Our data argue that this apparent gain of function may originate in part from defects in the biochemical activity of ribosomes lacking Asc1. First, we find that ribosomes lacking Asc1 are less efficient at elongating on mRNAs with both inhibitory and optimal pairs *in vitro* (Fig 4A and EV3B). Second, by ribosome profiling, we observe a higher fraction of 21 nt

RPFs in cells lacking Asc1 suggesting a general defect in tRNA decoding within the A site of the ribosome (Fig 4B, C). While this finding is somewhat surprising from a structural perspective, given that Asc1 is located on the 40S subunit far away from the decoding center, one possibility is that the loss of Asc1 affects the conformation of Rps3, a ribosomal protein that directly interacts with Asc1 and forms a part of the mRNA entry channel^{46,47}. Asc1 is also positioned such that it may be involved in sensing ribosome collisions that lead to ribosome rescue pathways^{42,43,48}. It seems likely that the increased read-through on inhibitory sequences in the Asc1 deletion strain arises from initial defects in the decoding step (promoting frameshifting) as well as by the loss of cellular responses to ribosome pausing.

Detailed mechanistic insight into the origins of A site accommodation defects was ultimately provided by our structural analysis. In our cryo-EM structures of ribosome-nascent chain complexes stalled on the CGA-CGA or CGA-CCG codon pairs, we identified several structural details that likely directly affect tRNA binding/accommodation activity. Interestingly, in each case these alterations are mediated by the structure of the mRNA itself and readily explain the previously proposed communication between the ribosomal A- and P sites (Figs 5 and EV5)¹³. In particular, for both the CGA-CCG and CGA-CGA inhibitory pairs, the C+4 mRNA nucleotide is dramatically flipped away from the A site decoding center of the ribosome. The C+4 nucleotide instead makes contact with the P site codon and interacts with C1637 of 18S rRNA which stacks to the anticodon inosine decoding the wobble position (A+3) of mRNA in the P site. The path of the mRNA is also affected by the purine:purine A:I wobble base pair at position +3 and shifts towards C1637. This perturbation involving the A:I wobble interaction provides an immediate

explanation for why the CGA codon in particular confers the strongest elongation defect. Moreover, the A/P kink of the mRNA, which was shown to be crucial for A site interaction and proofreading⁴⁰, is moved downstream in these structures as a consequence (Fig 5F, I). This critical structure is typically stabilized by an ammonium ion in X-ray structures⁴⁹ and was proposed to be essential for frame maintenance by preventing slippage⁵⁰. Finally, in the case of CGA-CCG, we observe a hairpin structure formed by mRNA nucleotides between positions +5 and +14 (Fig EV5D, E). This structure may be particular to this reporter mRNA sequence since no equivalent stable mRNA secondary structure is formed in the case of the CGA-CGA stalled RNC. Interestingly, a similar A site hairpin was observed previously in a structure implicated in translational bypassing⁵¹.

Consistent with the earlier work¹³, we see a specific deleterious effect of I:A wobble decoding on translation efficiency in inhibitory codon pairs containing the 5' CGA codon. Previously, the purine:purine I:A base pair was analyzed in the A site only, where its accommodation affects and alters mainly the anticodon of tRNA, due to its unique “wide” purine-purine geometry³⁰. In contrast, in our structure of the I:A wobble pair in the P site, we find that its accommodation affects not the anticodon of tRNA but rather the mRNA backbone (Figs 5E and H). This mRNA distortion apparently imposes allosteric effects on the neighboring region resulting in the unusual mRNA conformation in the A site. The modification of adenosine to inosine⁵² expands the decoding range of the ICG tRNA^{Arg} as inosine is able to base-pair with cytidine, uridine and even adenosine at the wobble position. It is intriguing to observe that this seemingly elegant evolutionary decoding mechanism has certain associated disadvantages as the non-optimal CGA codon

(decoded via the I:A interaction with the ICG tRNA^{Arg}) is slow to decode and leads to deleterious effects on mRNA stability⁵³.

In the case of translation of poly(A) tracts, previous studies proposed that electrostatic interactions between the poly-basic nascent chain and the peptide exit tunnel of the ribosome might elicit ribosomal stalling²⁰. Using our detailed structural information, we were able to reveal that an mRNA-mediated mechanism is directly contributing to stalling. Consecutive adenosines are engaged in a π -stacking array in the A site, stabilized on both sides by rRNA base stacking interactions, and adopt a helical conformation typical for single stranded poly(A) stretches (Fig 6E, F)⁴¹. This π -stacking array represents a decoding-incompetent structure. Conversely, the crucial catalytic bases in the peptidyl-transferase center (PTC) did not seem to be hindered from moving into the induced state conformation despite the presence of extra density which is not clearly interpretable (Fig 6C). This extra density adopts a defined shape next to the last nascent amino acid residue and could potentially be assigned to a mixed nascent chain state or even a small molecule. However, the observed geometry of the PTC cannot explain the highly efficient stalling on poly(A) tracts and the absence of any A site tRNA in 93% of particles in the dataset. Therefore, we argue that the inhibitory conformation of mRNA in the A site is at the basis of the poly(A)-mediated stalling mechanism. These ideas agree with previous observations that consecutive AAG codons are less efficient in stalling than AAA codons²¹ despite encoding for the same amino acid residue and that the intrinsic π -stacked helical structure of poly(A) single strand tract is efficiently disrupted by inclusion of guanosines⁴¹. Taken together, while we can't exclude the possibility that the basic nascent chain also

contributes, the stalling mechanism employed at poly(A) stretches mainly depends on the specific inhibitory conformation of the mRNA in the A site.

Interestingly, when studying ribosomal collisions as a consequence of poly(A)-mediated stalling, we found a large fraction of the disomes in a novel POST-POST state that was distinct from the previously characterized disome structures in both mammalian and yeast systems (Fig 7A, B) ^{42, 43}. In both previous structures, the second colliding ribosome is captured in a rotated PRE state unable to translocate further. Finding both collided ribosomes in the POST state indicates that the second colliding ribosome completed the translocation step, likely due to a weaker “roadblock” presented by the first stalled ribosome. Since poly(A) tracts were characterized as slippery ²¹, it is tempting to speculate that applying force on the first stalled ribosome by the colliding ribosome(s) could contribute to ribosome sliding on the mRNA and loss of reading frame. This model is consistent with recent findings that directly implicate ribosomal collisions in +1 frameshifting ⁵⁴. Ribosomal collisions could, in principle, disrupt the interaction between the P site tRNA and the mRNA in the first ribosome and contribute to +1 frameshifting observed after ribosomal pausing ⁵⁵. We speculate that the loss of reading frame in the case of collisions on poly(A) tracts is facilitated by (i) the fact that the P site tRNA is the only one left on the stalled ribosome after the E site tRNA dissociates and (ii) the fact that the P site tRNA only interacts with the mRNA via relatively less stable A:U base pairs. These ideas are consistent with earlier studies arguing that reading frame maintenance is predominantly affected by the energetics of the P-site codon-anticodon interaction ⁵⁶.

Taken together, our work combines *in vitro* and *in vivo* methods to study the effects of inhibitory mRNA sequences, and shows for the first time detailed mechanistic insight into mRNA-mediated translation stalling via decoding obstruction.

Figures

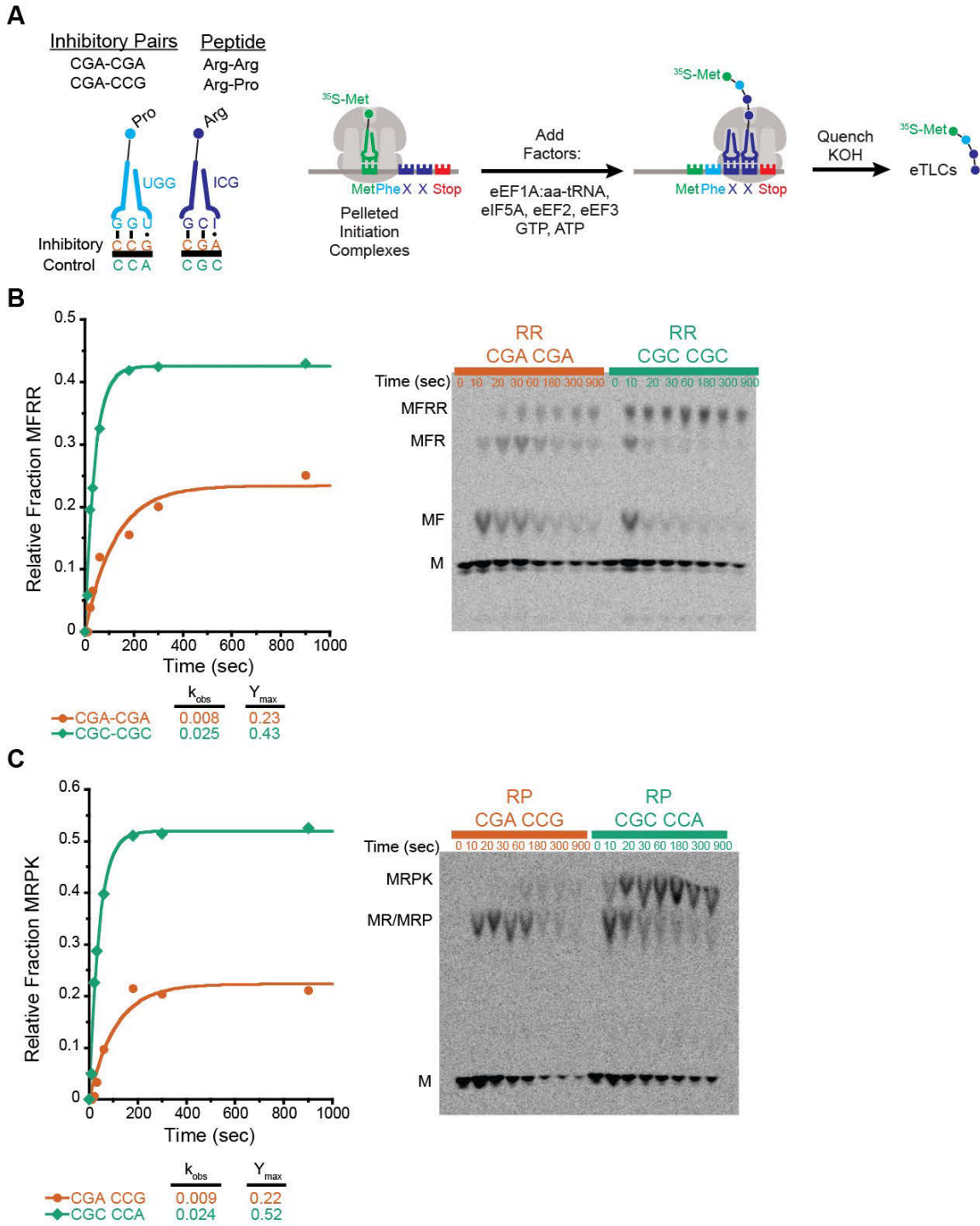


Figure 1

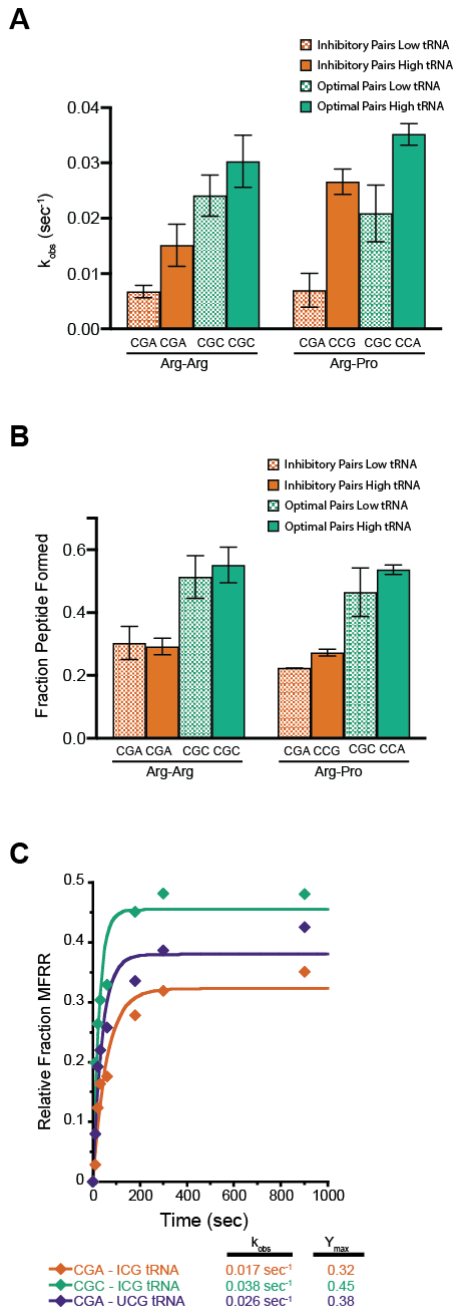


Figure 2

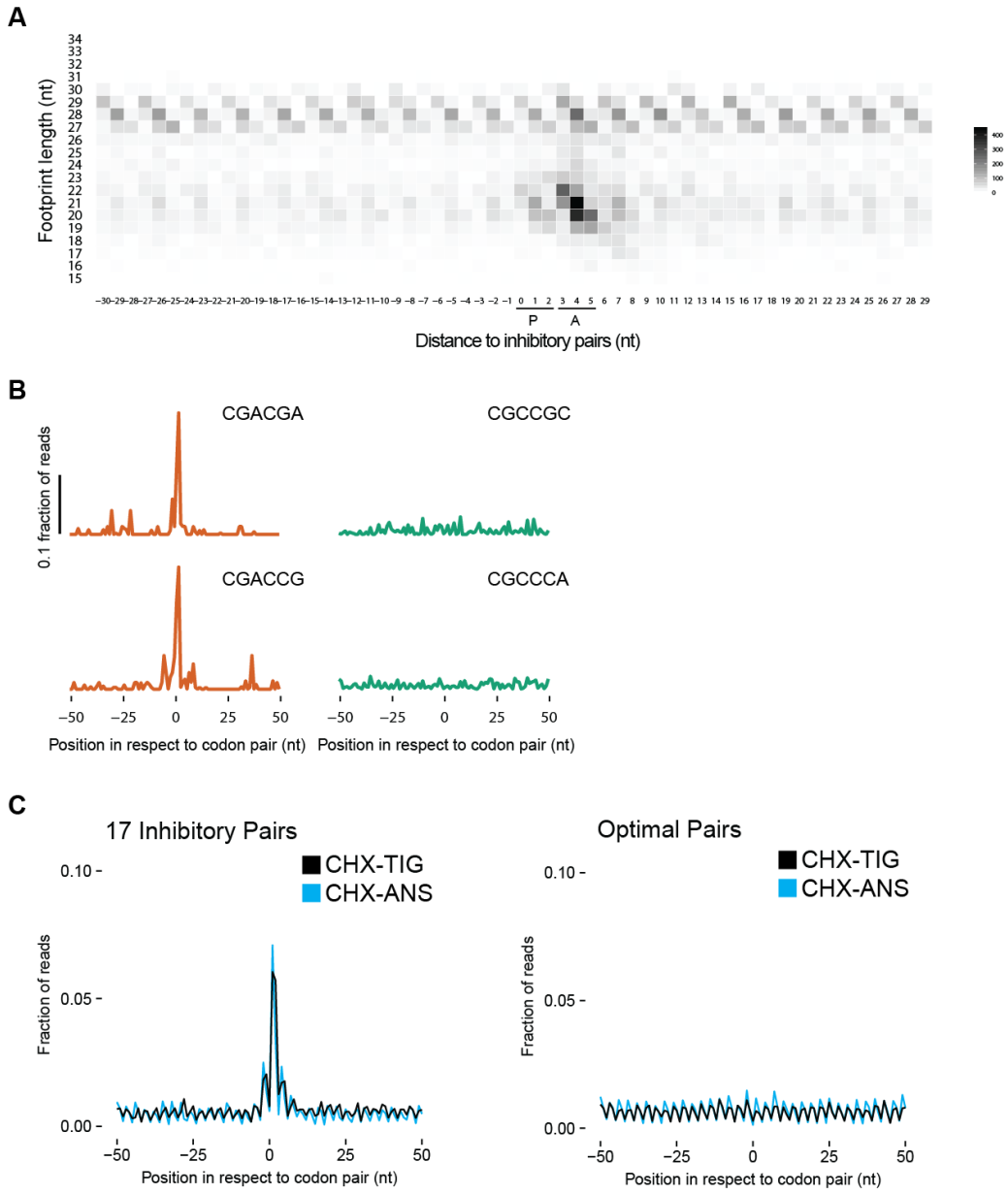


Figure 3

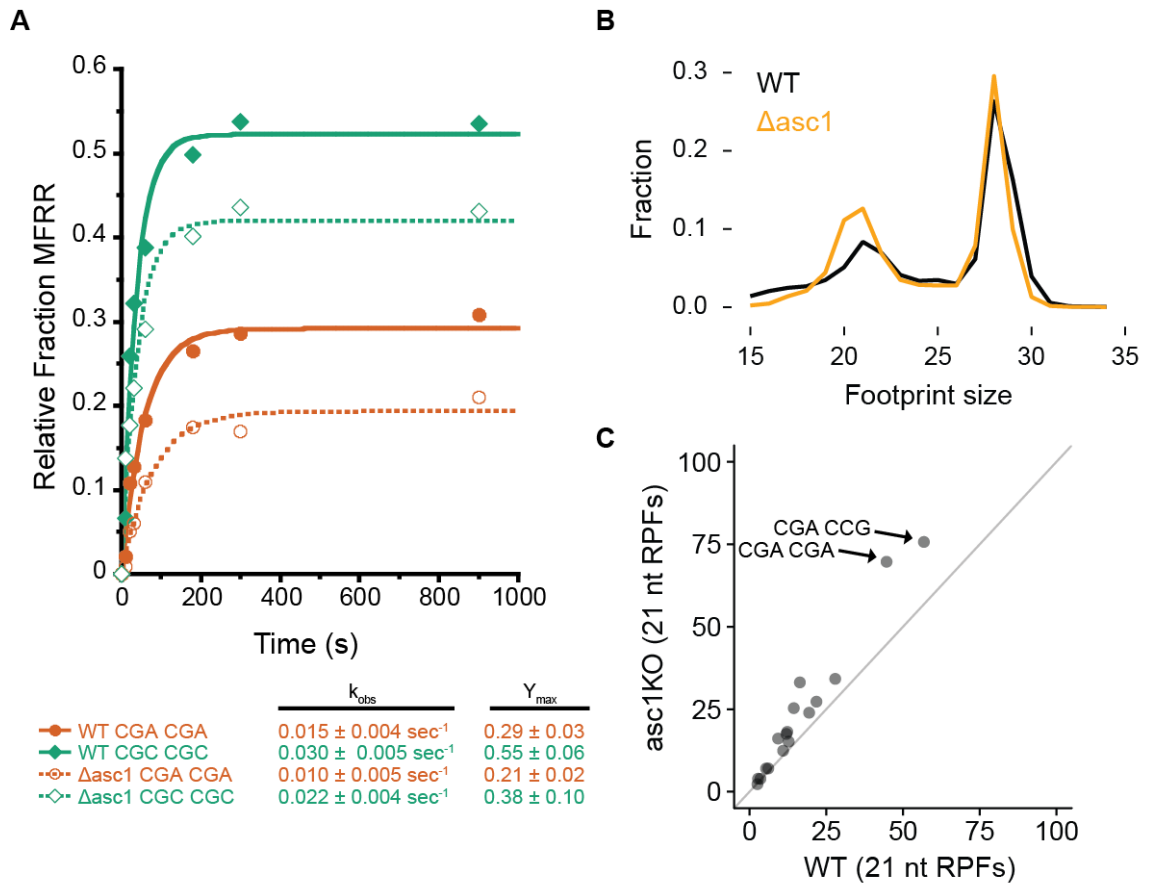


Figure 4

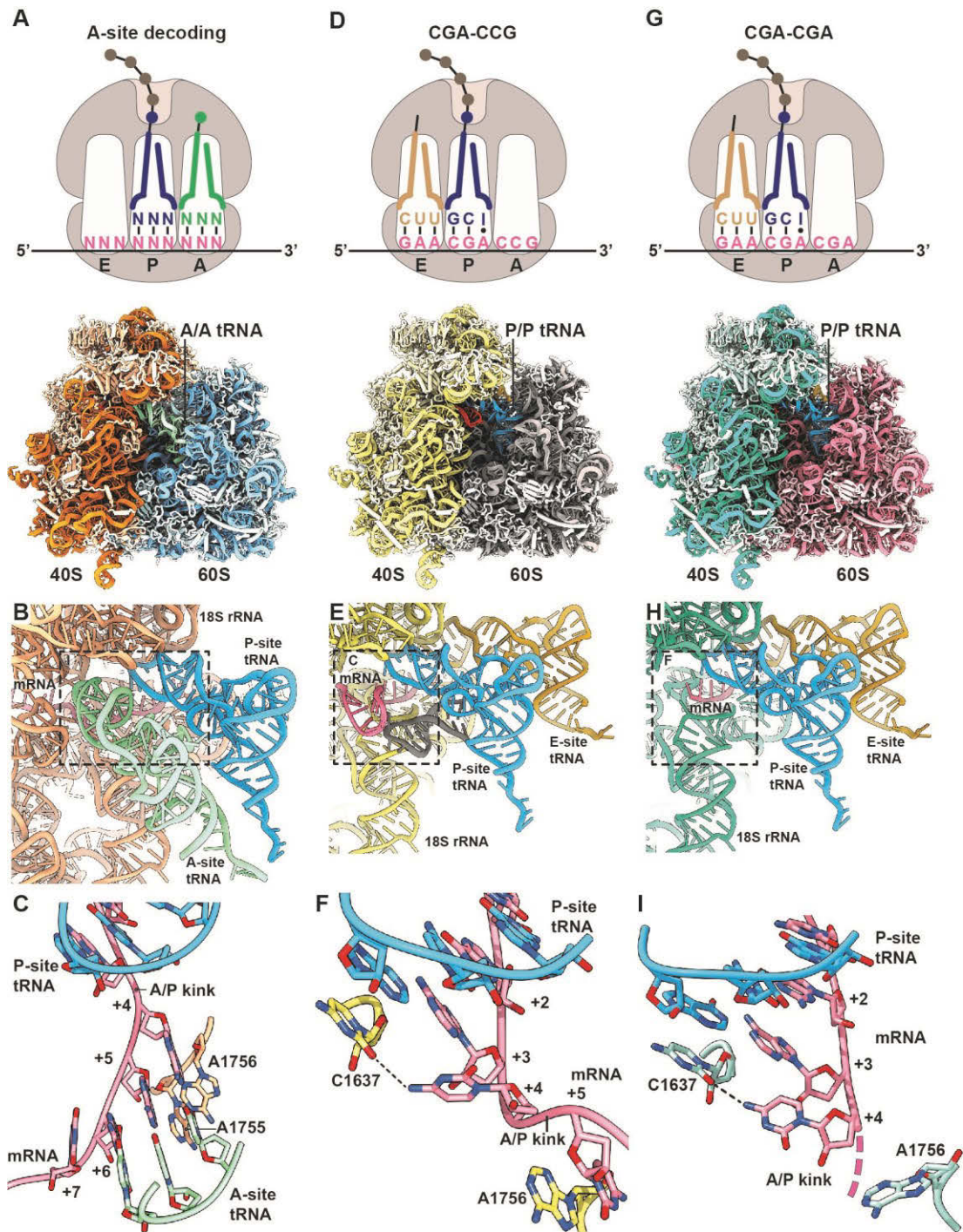


Figure 5

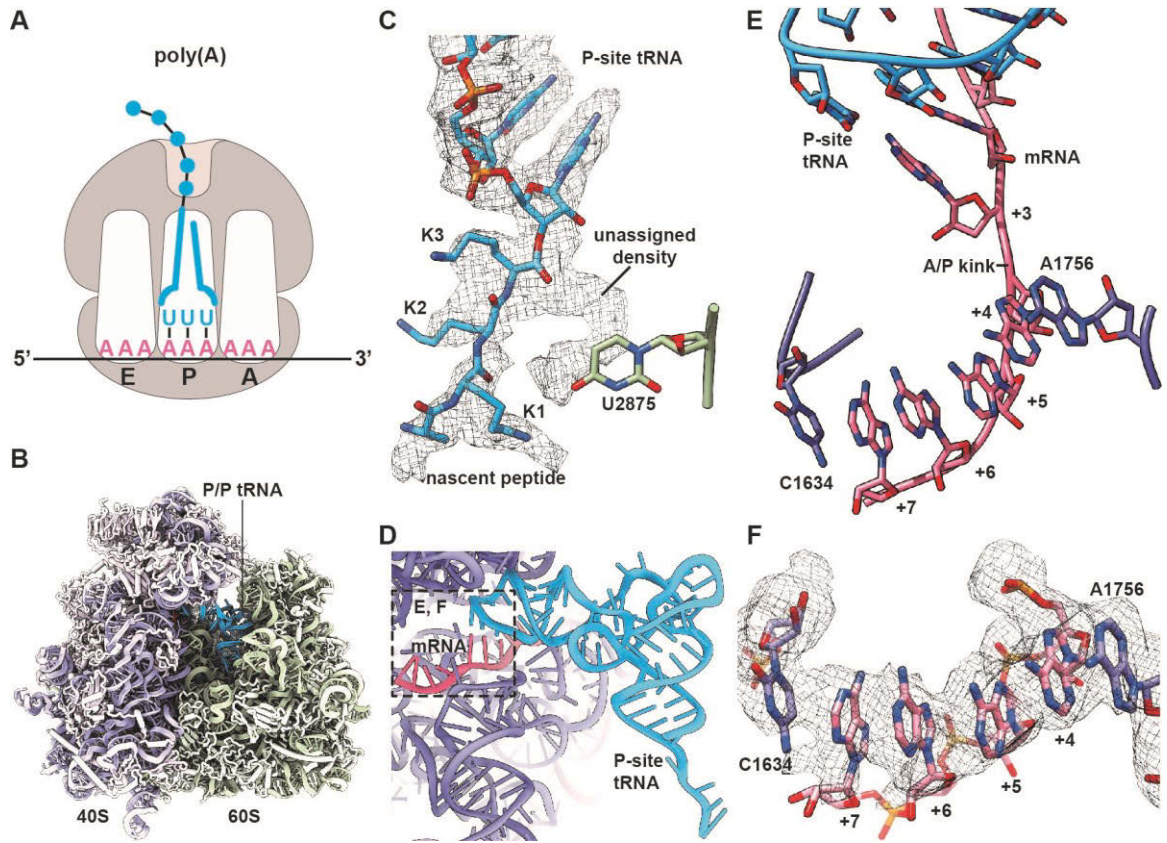


Figure 6

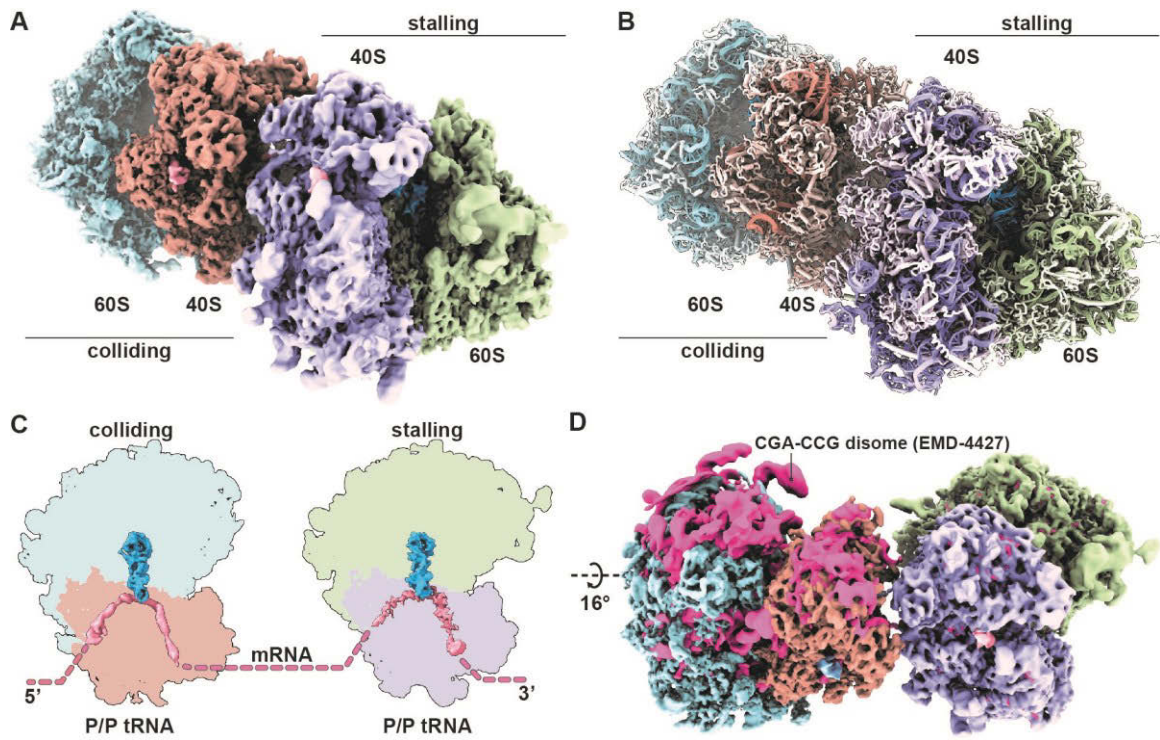
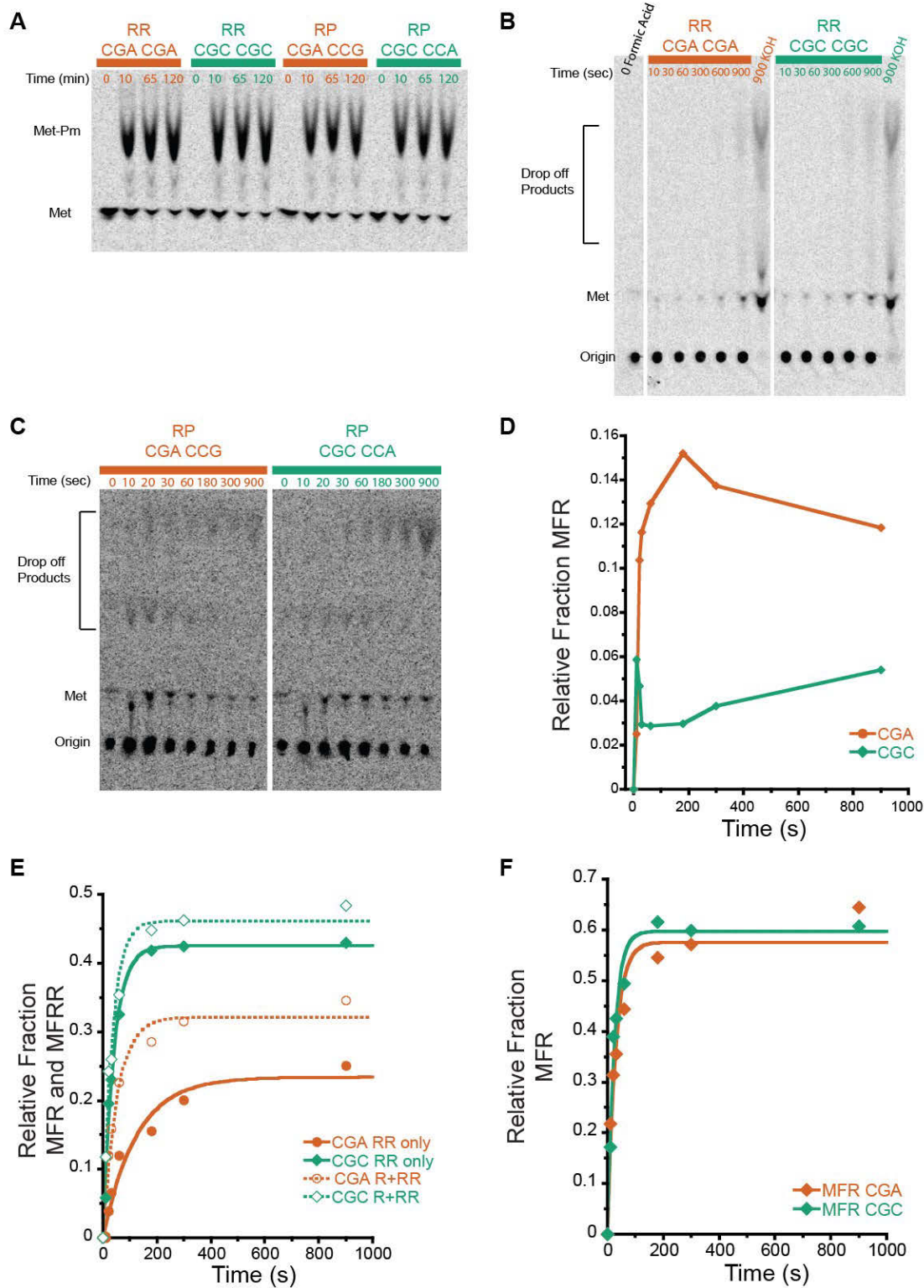
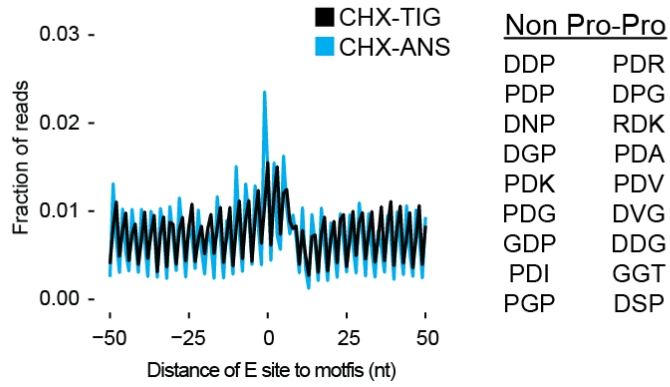


Figure 7



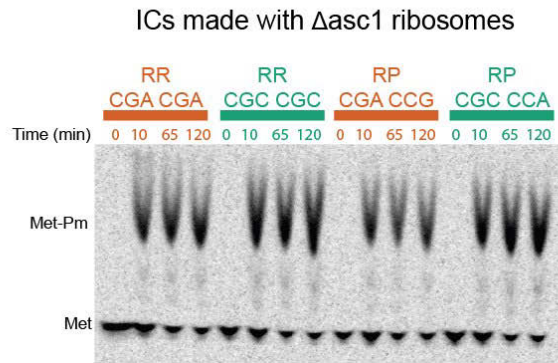
Expanded View Figure 1

A Peptide Transfer Problem

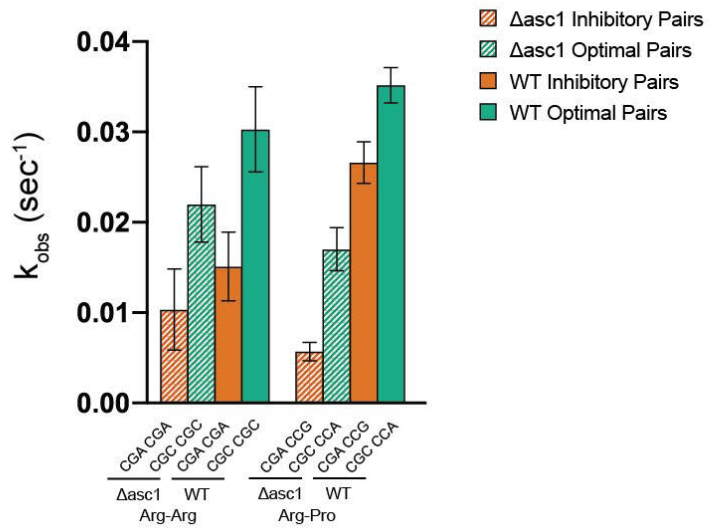


Expanded View Figure 2

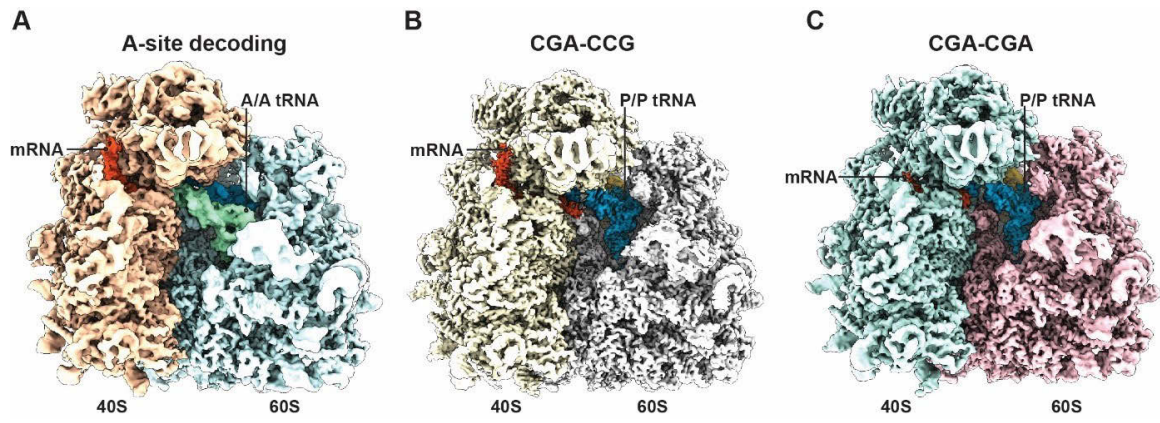
A



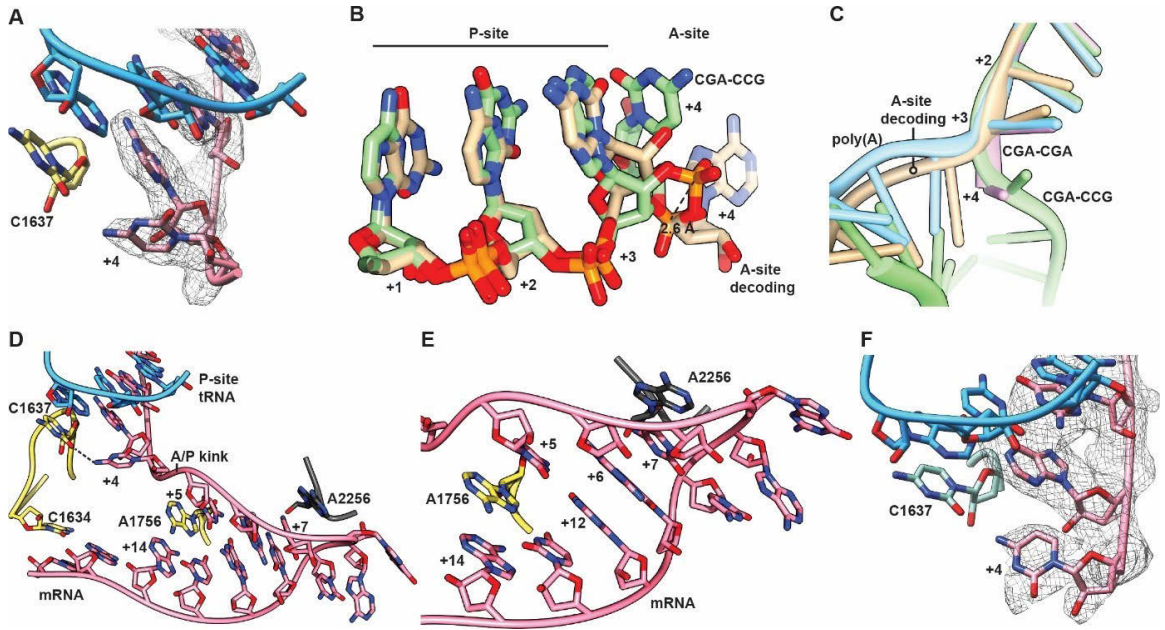
B



Expanded View Figure 3

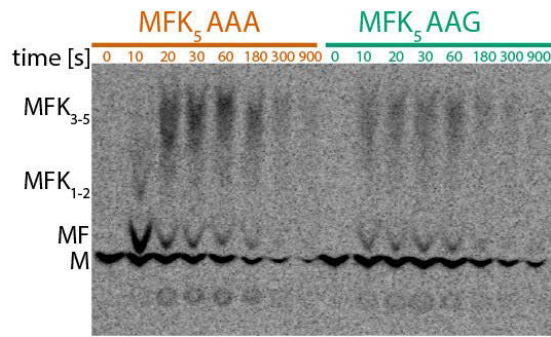


Expanded View Figure 4

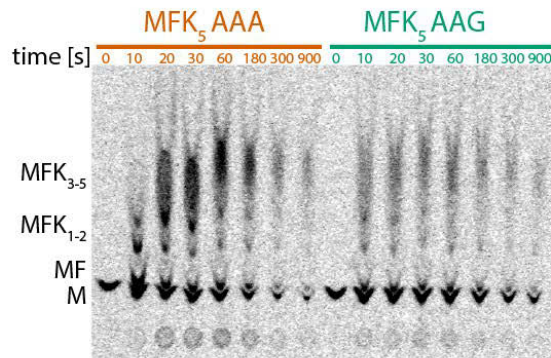


Expanded View Figure 5

A

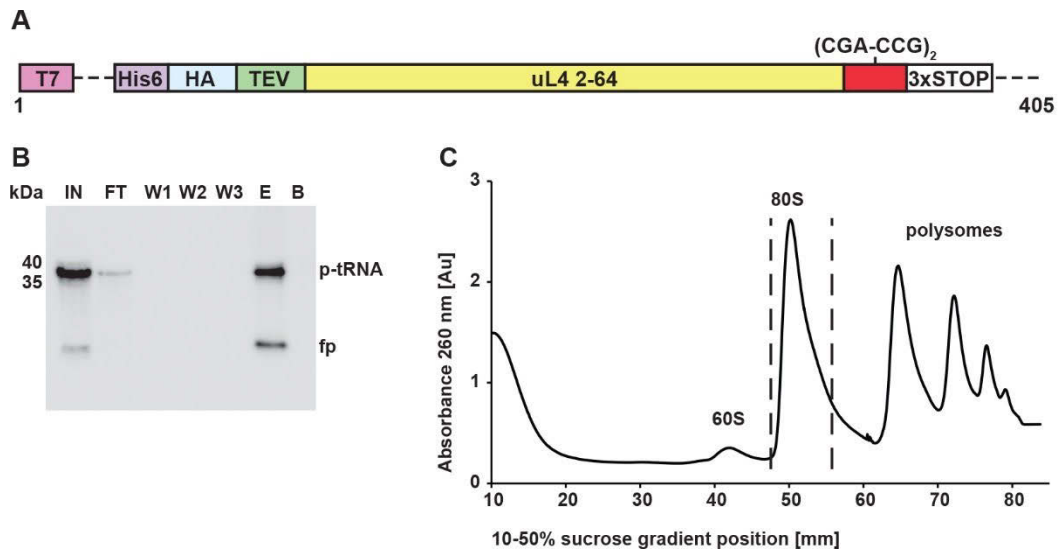


Diluted samples

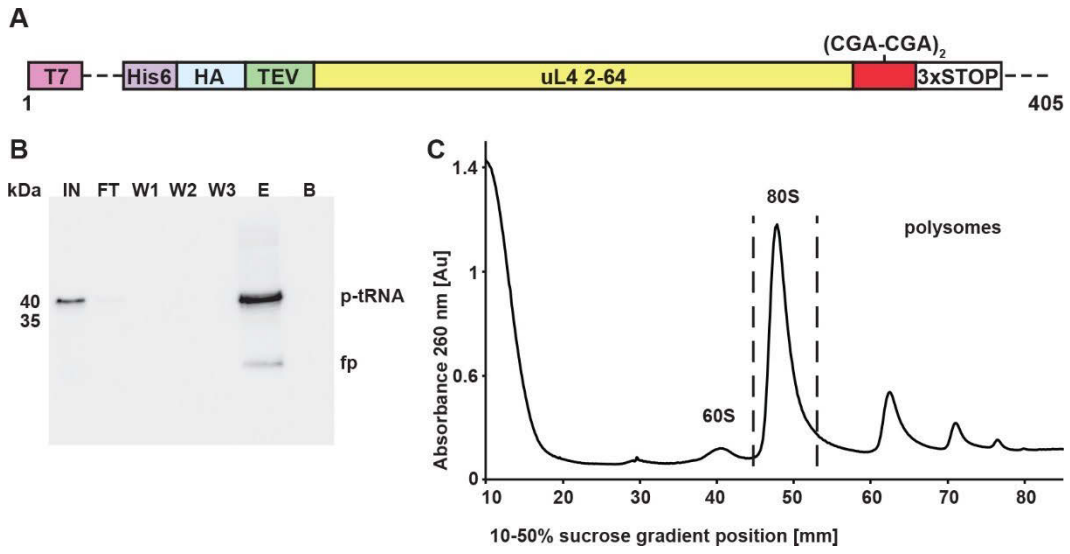


Un-diluted samples

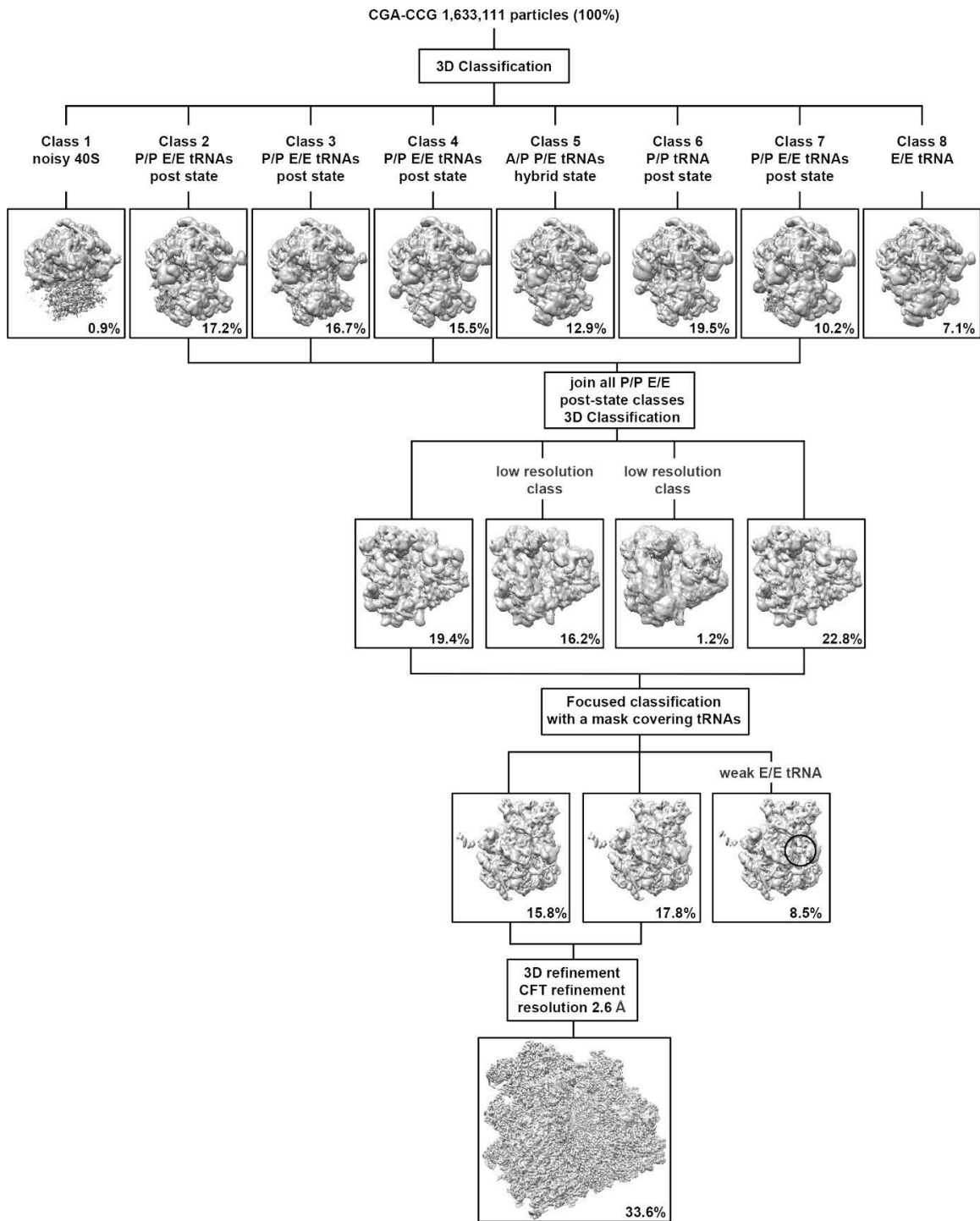
Expanded View Figure 6



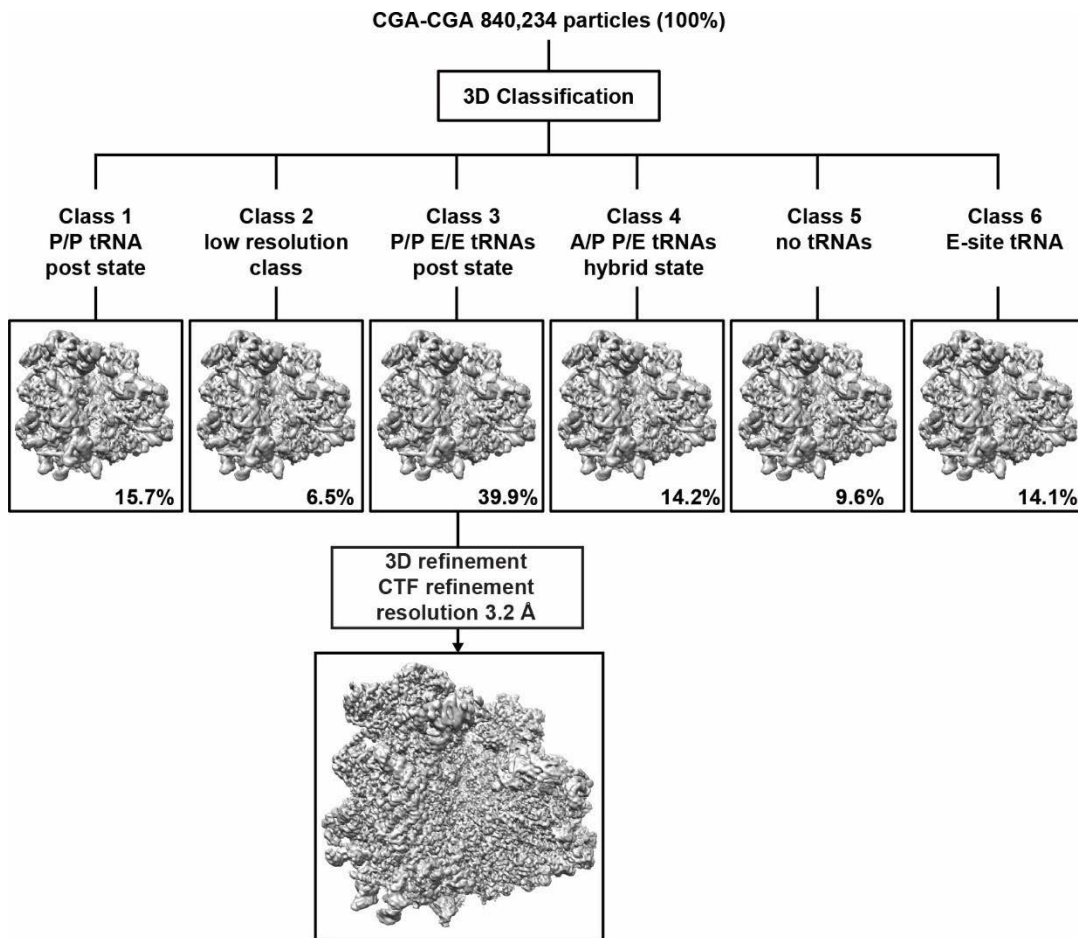
Appendix Figure S1



Appendix Figure S2



Appendix Figure S3



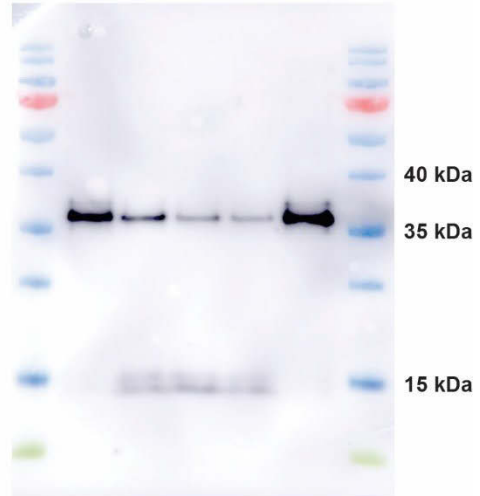
Appendix Figure S4

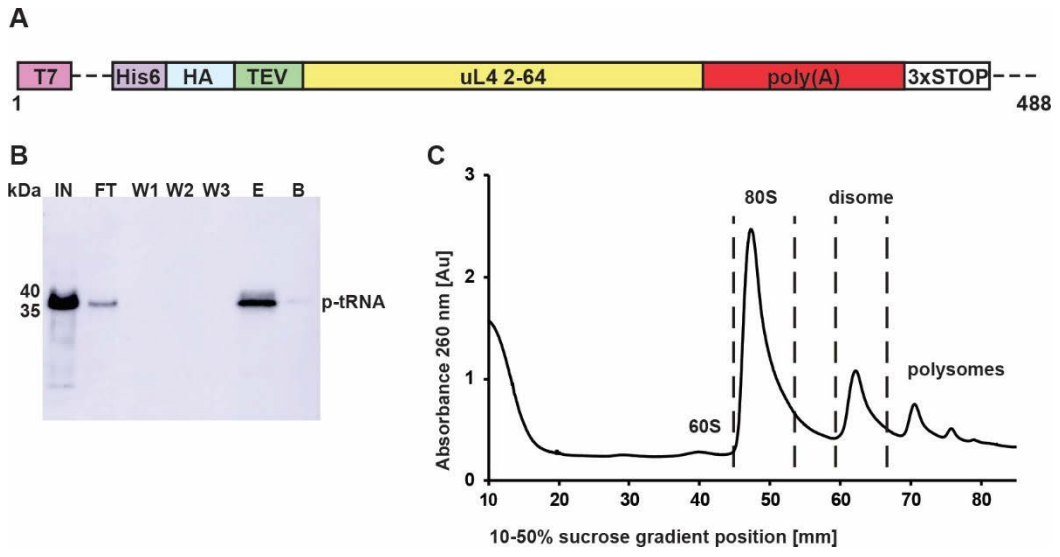
A

	CGA-CGA			
puromycin	+	+	+	-
time [min]	0	5	10	10

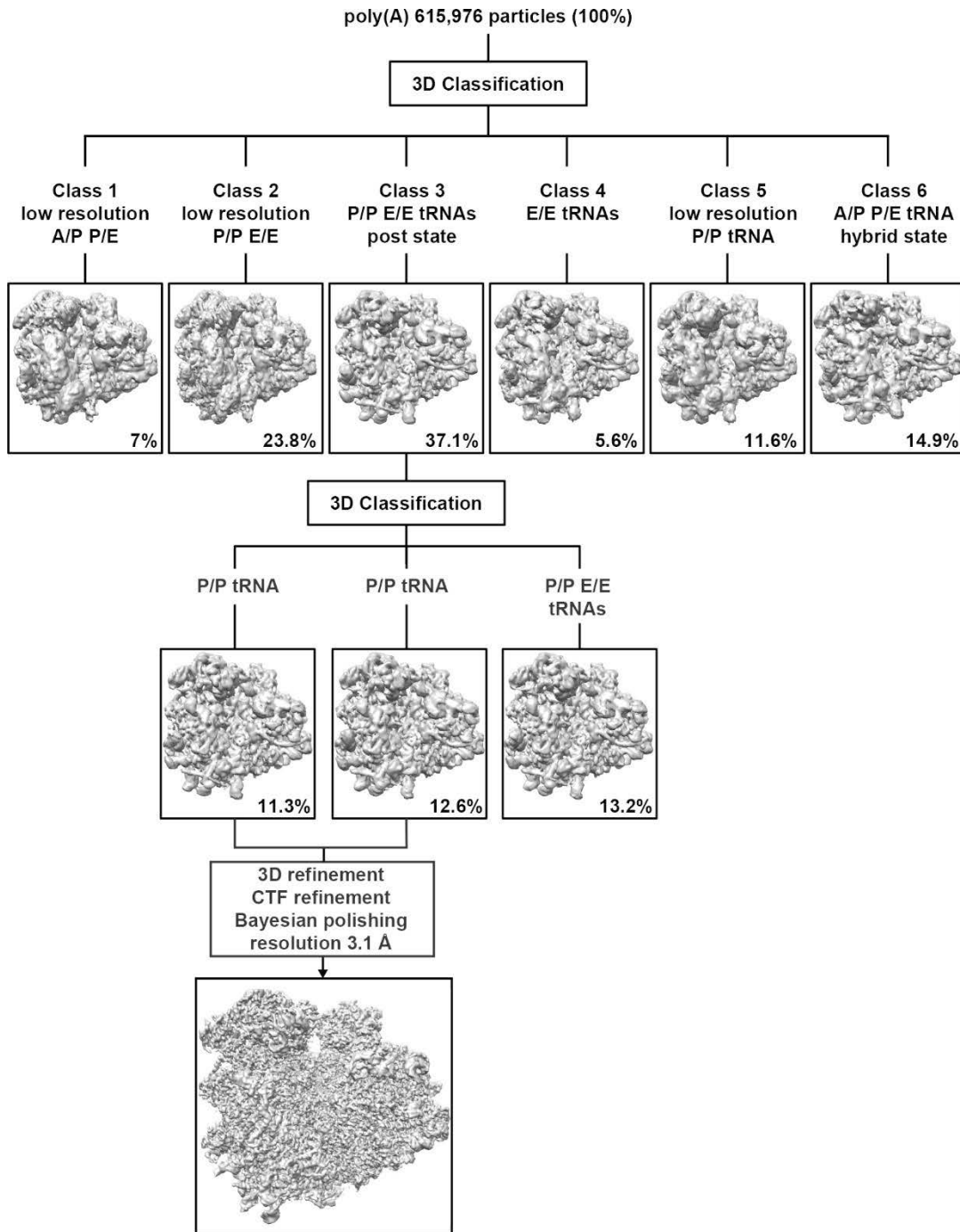
**B**

	CGA-CCG				
puromycin	+	+	+	+	-
time [min]	0	5	10	15	15

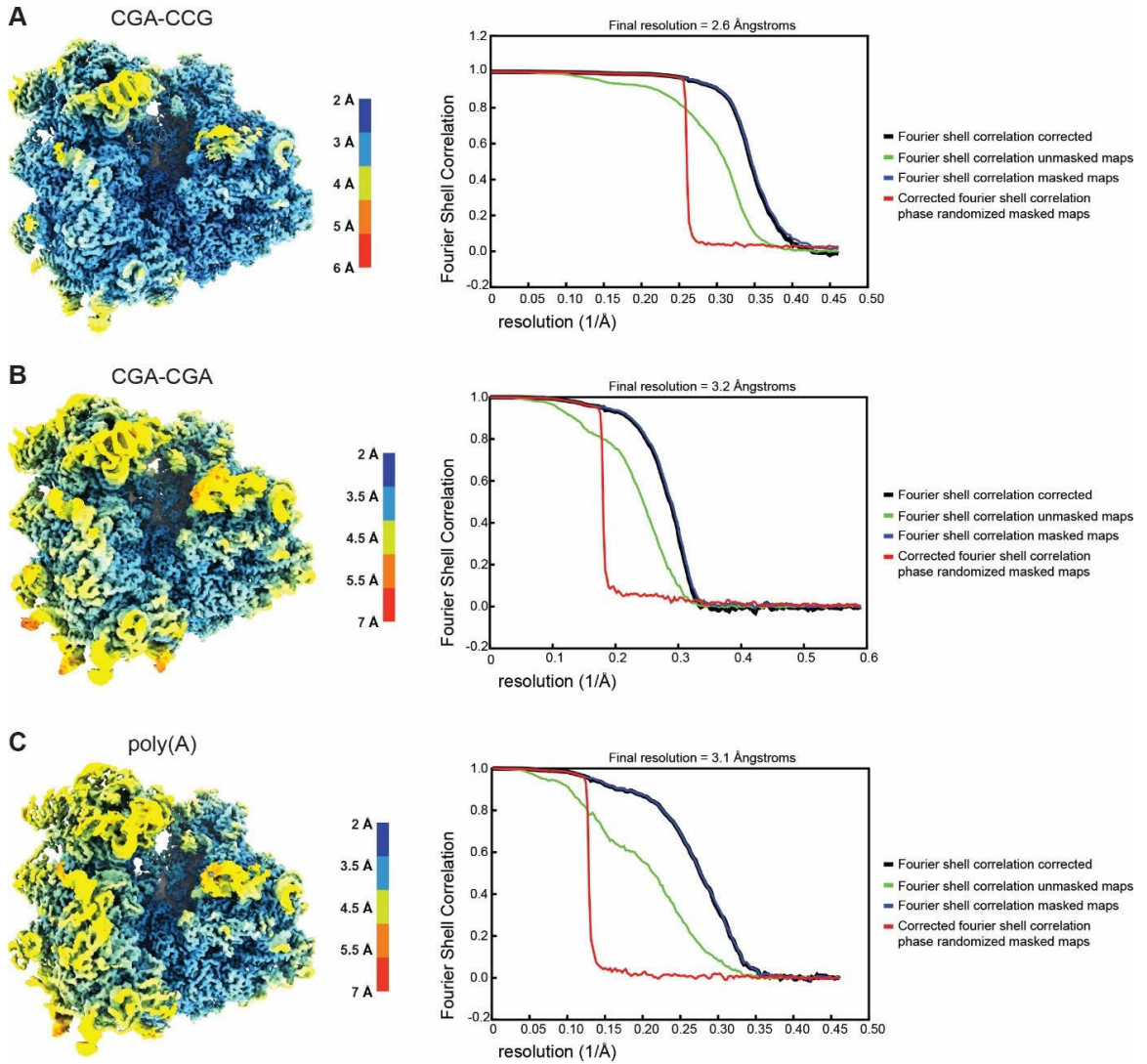
**Appendix Figure S5**



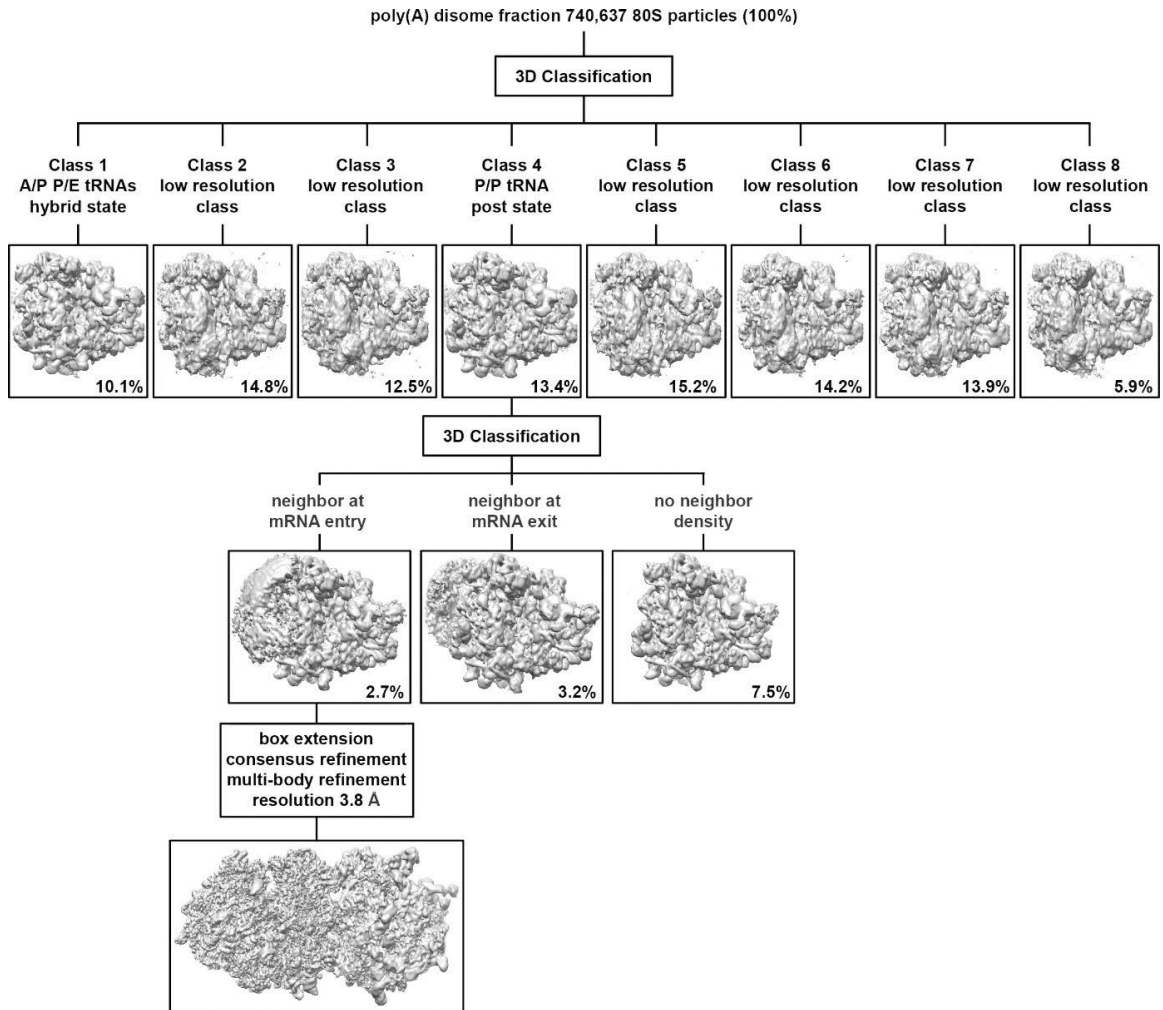
Appendix Figure S6



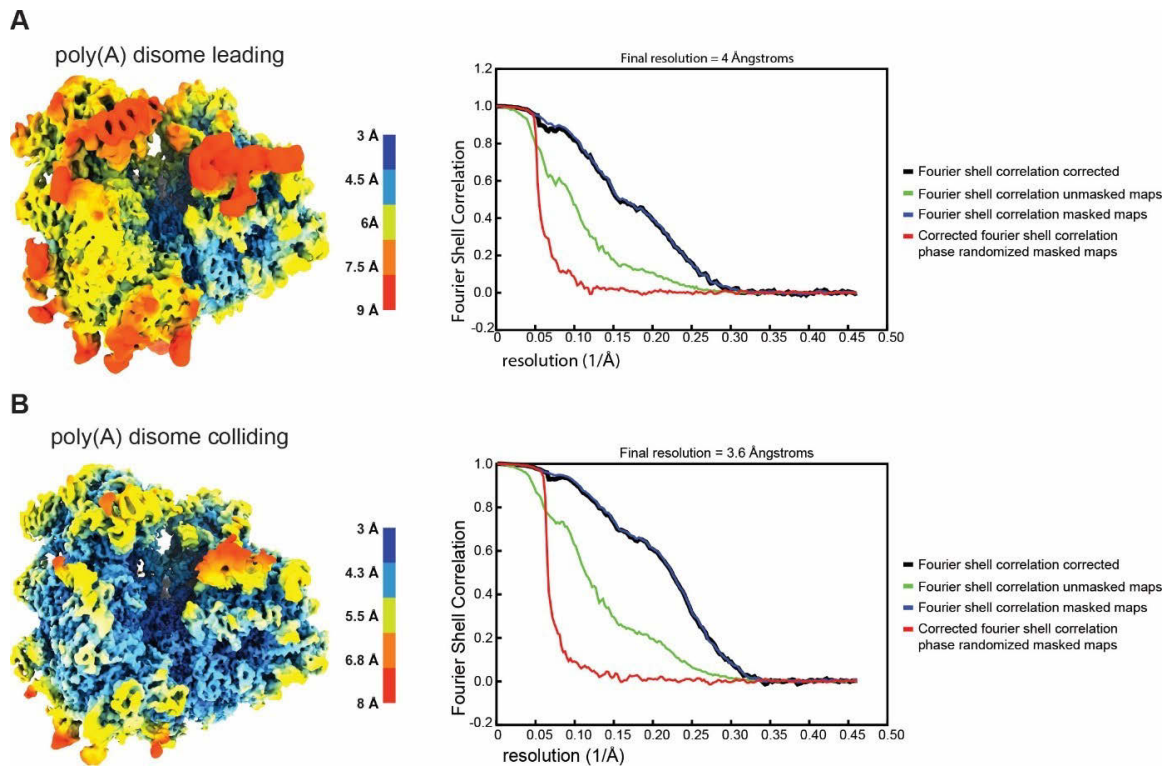
Appendix Figure S7



Appendix Figure S8



Appendix Figure S9



Appendix Figure S10

Figure Legends

Figure 1. Inhibitory codon pairs slow elongation *in vitro*. (A) Inhibitory pairs showing the inhibitory mRNA codons (red) and the optimal codons (green). Schematic representation of the *in vitro* elongation reactions performed using the reconstituted yeast translation system. (B) Representative eTLCs (left) and corresponding elongation kinetics (right) for the CGA-CGA inhibitory pair (red) and the CGC optimal pair (green). (C) Representative eTLCs (left) and corresponding elongation kinetics (right) for the CGA-CCG inhibitory pair (red) and the CGC-CCA optimal pair (green). Product formation in (C) and (D) are normalized to the fraction of Met ICs that form Met-Puro when reacted with puromycin (Fig EV1A).

Figure 2. Effects of tRNA concentration on elongation rates and endpoints.

(A) Comparison of observed rates of elongation for inhibitory pairs (red) and their optimal controls (green) at limiting tRNA concentrations (hatched bars) and saturating tRNA concentrations (solid bars). (B) Comparison of total peptide formation for inhibitory pairs (red) and their optimal controls (green) at limiting tRNA concentrations (hatched bars) and saturating tRNA concentrations (solid bars). (C) Elongation kinetics for the CGA-CGA inhibitory codon pair with the native ICG tRNA^{Arg} (red) or the non-native UCG tRNA^{Arg} (purple) and for the CGC-CGC optimal control pair with the native ICG tRNA^{Arg} (green). Error bars represent standard deviations calculated from at least three experimental replicates.

Figure 3. Increased 21 nt RPFs on inhibitory pairs indicate an empty ribosomal A site. (A) Meta-analysis of footprint size of all 17 inhibitory pairs identified by Grayhack and coworkers (Gamble et al., 2016), aligning the first codon of the pair in the ribosomal P site. **(B)** Metacodon analysis of 21 nt RPFs centered at the first codon of each inhibitory pair (red) compared to their corresponding optimal pair (green). **(C)** Comparison of 21 nt RPFs aligned at all 17 inhibitory codons from libraries made with CHX/ANS (blue) and CHX/TIG (black) (left) to their corresponding optimal pairs with the same antibiotic combination (right).

Figure 4. Loss of the ribosomal protein Asc1 inhibits elongation. (A) Elongation kinetics for the CGA-CGA inhibitory codon pair (red) and the CGC-CGC optimal control (green) from WT ribosomes (solid) or the *asc1Δ* strain ribosomes (dashed) at saturating tRNA concentrations. Average observed rates and elongation endpoints from three or more replicate experiments shown below the graph. **(B)** Size distributions of ribosome footprints for WT cells (black) and *asc1Δ* cells (gold). **(C)** Scatter plot of ribosome occupancies for 21 nt RPFs at the 17 inhibitory codon pairs (Gamble et al., 2016) comparing WT cells to *asc1Δ* cells with the two inhibitory codon pairs further investigated in this study labeled.

Figure 5. CGA-CCG and CGA-CGA induce stalling through decoding-incompatible mRNA conformations in the A site. (A-C) Cryo-EM structural characterization of the pre-state RNC with A site tRNA in the decoding center. **(A)** Schematic representation of the decoding situation (top) and molecular model for the pre-state RNC with A site tRNA in the decoding center. **(B)** General overview of the A, P and E sites with A/A and P/P tRNAs and mRNA. **(C)** Detailed view of the mRNA in the A site using sticks model with cartoon phosphate backbone representation. The 18S rRNA bases A1755 and A1756 recognize the minor groove of A site tRNA – mRNA interaction during tRNA decoding. **(D-F)** Cryo-EM structural characterization of the CGA-CCG stalled RNC. **(D)** Schematic representation of the stalling situation (top) and molecular model of the CGA-CCG stalled RNC (bottom). **(E)** General overview of the A, P, and E sites with P/P and E/E tRNAs and mRNA. **(F)** Detailed view of the mRNA in the A site using sticks model with cartoon phosphate backbone representation. The mRNA positions +2 to +5 and their interactions are shown. The C +4 is flipped by approximately 95° degrees towards the wobble A:I base pair in the P site and stabilized by interaction with the C1637 of the 18S rRNA helix 44. The C +5 is stabilized by stacking interaction with the A1756 of the 18S rRNA which normally recognizes the minor groove of A site tRNA – mRNA interaction during decoding **(L).** **(G-I)** Cryo-EM structural characterization of the CGA-CGA stalled RNC. **(G)** Schematic representation of the stalling situation (top) and molecular model of the CGA-CGA stalled RNC (bottom). **(H)** General overview of the A, P and E sites with P/P and E/E tRNAs and mRNA. **(I)** Detailed view of the mRNA in the A site as in (E). Downstream mRNA is indicated by the dotted line. Note the rotation of the C+4 base compared to the CGA-CCG mRNA.

Figure 6. Ribosomes stalled on poly(A) stretches reveal alterations in both the peptidyl-transferase and decoding centers. (A) Schematic representation of the stalling situation on poly(A) tract mRNA. Cryo-EM density map of the poly(A) stalled RNC filtered according to local resolution and used to build the molecular model **(B)**. **(C)** Cryo-EM density (mesh) and stick model with cartoon phosphate backbone representing the peptidyl-tRNA in the peptidyl-transferase center (PTC). **(D)** General overview of the A, P, and E sites with the P/P tRNA and mRNA. **(E, F)** Detailed view of the mRNA in the A site using sticks model with cartoon phosphate backbone representation and cryo-EM density (mesh). The poly adenine mRNA sequence forms a π -stacking array between positions +4 and +7, which is stabilized from both sides by stacking of 18S rRNA bases C1634 and A1756.

Figure 7. Disomes stalled on poly(A) tracts form a novel POST-POST assembly.

(A) Composite cryo-EM density map of the POST-POST disome stalled on the poly(A) mRNA reporter filtered according to local resolution and used to build the molecular model **(B)**. **(C)** Cut top views of both the first (stalling) and the second (colliding) ribosomes forming the disome. Observed ribosomal and tRNA translocation states are indicated. **(D)** Comparison of ribosomal assemblies between the previously described CGA-CCG stalled yeast disome in pink (EMD-4427, Ikeuchi, Tesina et al., 2019a) and the novel POST-POST assembly observed in poly(A) stalling. The EMD-4427 density map was fitted into the density of the first stalling ribosome on the poly(A) reporter. The indicated rotation was calculated using the 60S subunit, as the compared colliding ribosomes are not in the same translocation state (PRE vs. POST).

Expanded View Figure 1. Initiation complex test of Met-Pm activity and individual product analysis of MFRR elongation. (A) Met-Pm activity for all the ICs formed with WT ribosomes on inhibitory mRNAs (red) and optimal mRNAs (green). There is no significant difference in activity at the last time point for any of the ICs. **(B)** TLC showing peptidyl tRNA drop off using the PTH assay on MFRR ICs with the inhibitory (CGA-CGA) pair (red) and the optimal (CGC-CGC) pair (green). Time points were quenched with formic acid to assess drop off and time points quenched with KOH were to monitor peptide formation as a control. There is no significant accumulation of peptidyl tRNA drop off products. **(C)** TLC showing peptidyl tRNA drop off using the PTH assay on MRPK ICs with the inhibitory (CGA-CCG) pair (red) and the optimal (CGC-CCA) pair (green). Time points were quenched with formic acid to assess drop off. There is no significant accumulation of peptidyl tRNA drop off products. **(D)** Elongation kinetics for the MFR product within the context of MFRR elongation for the inhibitory (CGA-CGA) pair (red) and the optimal (CGC-CGC) pair (green). MFR peptide builds up on the inhibitory pair as compared to the optimal pair indicative of slow formation of the next peptide bond. **(E)** Elongation kinetics for the MFR and MFRR products together versus the final MFRR product alone for the inhibitory (CGA-CGA) pair (red) and the optimal (CGC-CGC) pair (green). The increased rate and amount of product formed for the MFR and MFRR data compared to the MFRR alone suggest that the addition of the second arginine is slower than the first. **(F)** Elongation kinetics for the addition of a single arginine MFR CGA (red) and CGC (green). The addition of the first arginine is only slightly slower for CGA again suggesting that the addition of the second arginine is the slower step.

Expanded View Figure 2. Ribosome profiling analysis showing defects in peptide bond formation. (A) Metacodon analysis of 21 nt RPFs in libraries prepared with CHX/ANS (blue) showing an increase in ribosome density at tripeptide motifs that undergo slow peptide bond formation (Schuller et al., 2017) compared to libraries prepared with CHX/TIG.

Expanded View Figure 3. Initiation complex test of Met-Pm activity with ribosomes lacking Asc1 and their corresponding elongation rates. (A) Met-Pm activity for all the ICs formed with ribosomes from *asc1Δ* strain on inhibitory mRNAs (red) and optimal mRNAs (green). There is no significant difference in activity at the last time point for any of the ICs as compared to one another or to the Met-Pm activity for WT ICs (Figure S1A). (B) Comparison of observed rates of elongation at saturating tRNA concentrations for all inhibitory pairs (red) and their optimal controls (green) by ICs formed with ribosomes lacking Asc1 (hatched bars) versus WT ribosomes (solid bars). Error bars represent the standard deviation calculated from three replicate experiments with the exception of the MFRP inhibitory and optimal pairs (two replicates).

Expanded View Figure 4. Cryo-EM structures of RNCs stalled on inhibitory codon pairs in comparison with the A site decoding situation. (A-C) Cryo-EM density maps filtered according to local resolution used to build molecular models. (A) Cryo-EM map of the pre-state RNC with tRNA in the A site. (B) Cryo-EM map of the CGA-CCG stalled RNC. (C) Cryo-EM map of the CGA-CGA stalled RNC.

Expanded View Figure 5. Structural details of the codon-based stalling. (A) Cryo-EM density (mesh) and stick model with cartoon phosphate backbone representing the mRNA positions +1 to +4 and their interactions in the CGA-CCG stalled ribosome. (B) Comparison between the A site tRNA decoding situation and the CGA-CCG stalled situation of the mRNA in positions +1 to +4. In the CGA-CCG A site, the C+4 is flipped by approximately 95° degrees towards the wobble A:I base pair and the mRNA backbone is shifted by 2.6 Å at the phosphate linking A+3 and C+4. (C) The effect of flipped C+4 on the general path of the mRNA in the A site. A cartoon representation of mRNAs in all four discussed 80S structures is compared. (D) Overview of the mRNA and its interactions in the A site of CGA-CCG reporter stalled ribosome using stick model with cartoon phosphate backbone representation. (E) Detail of the tip of the hairpin from (C) with stabilizing stacking interactions between A2256 of the 25S rRNA and the C+7 of the mRNA and among A1756 of the 18S rRNA intercalated between the C+5 and the A+14 of the mRNA. (F) Cryo-EM density (mesh) and stick model with cartoon phosphate backbone representing the mRNA positions +1 to +4 and their interactions in the CGA-CGA stalled ribosome.

Expanded View Figure 6. Elongation of AAA is slower than AAG on MFK₅ initiation complexes. (A) TLC showing peptide bond formation of MFK₅ messages on inhibitory AAA codons (red) and control AAG codons (green). Samples were diluted 1 to 4 µL in water (top) or undiluted (bottom). MFK₅ AAG complexes are making longer lysine peptides (indicated by higher bands on the TLC) than AAA at early timepoints.

Appendix Figure S1. CGA-CCG reporter mRNA and purification of the stalled 80S RNCs. (A) Schematic representation of the CGA-CCG mRNA reporter used for the structural studies. (B) *In vitro* translation reaction (IN) using a yeast translation extract from a *ski2Δ* strain and subsequent affinity purification of His-tagged ribosome-nascent chain complexes. Fractions representing input (IN), flow through (FT), washing steps (W1 – W3), elution (E) and beads (B) were visualized by immunoblotting using anti-HA antibody. Peptidyl-tRNA (p-tRNA) and free peptide (fp) bands are indicated. (C) The eluate was loaded on a 10-50 % sucrose gradient and fractionated. The indicated peak representing the 80S fraction was collected and concentrated using a sucrose cushion. Resuspended ribosomal pellet was used for cryo-EM sample preparation.

Appendix Figure S2. CGA-CGA reporter mRNA and purification of the stalled 80S RNCs. (A) Schematic representation of the CGA-CGA mRNA reporter used for the structural studies. (B) *In vitro* translation reaction (IN) using a yeast translation extract from a *ski2Δ* strain and subsequent affinity purification of His-tagged ribosome-nascent chain complexes. Fractions representing input (IN), flow through (FT), washing steps (W1 – W3), elution (E) and beads (B) were visualized by immunoblotting using anti-HA antibody. Peptidyl-tRNA (p-tRNA) and free peptide (fp) band sizes are indicated. (C) The eluate was loaded on a 10-50 % sucrose gradient and fractionated. The indicated peak representing the 80S fraction was collected and concentrated using a sucrose cushion. Resuspended ribosomal pellet was used for cryo-EM sample preparation.

Appendix Figure S3. 3D classification and processing scheme of the 80S ribosomes stalled on the CGA-CCG reporter mRNA. The first 3D refined map was sorted into 8 classes. Classes 2, 3, 4 and 7 represented a vast majority of programmed ribosomal particles exhibiting the non-rotated post state with P/P and E/E site tRNAs. These classes were joined and further sub-classified, sorting out low resolution and weak E site tRNA occupancy particles. This particle category was further refined and processed as indicated (for details, see Methods).

Appendix Figure S4. 3D classification and processing scheme of the 80S ribosomes stalled on the CGA-CGA reporter mRNA. The first 3D refined map was sorted into 6 classes. Class 3 represented a vast majority of programmed ribosomal particles exhibiting the non-rotated post state with P/P and E/E site tRNAs. This class was further refined and processed as indicated (for details, see Methods).

Appendix Figure S5. Puromycin reactivity of CGA-CGA and CGA-CCG stalled RNCs.

(A-B) 80S fractions of RNCs isolated from sucrose density gradients (Appendix Figs 1c and 2c) were treated with 1 mM puromycin. Nascent chain species were visualized by immunoblotting using anti-HA antibody. Peptidyl-tRNA and free peptide band sizes are indicated. (A) 80S RNCs stalled on the CGA-CGA reporter mRNA readily reacted with puromycin releasing all detectable nascent chains within the first five minutes of the reaction. (B) 80S RNCs stalled on the CGA-CCG reporter mRNA reacted with puromycin slower than the CGA-CGA ones with a small fraction of unreacted peptidyl-tRNA still detectable after 15 minutes of the reaction.

Appendix Figure S6. Poly(A) reporter mRNA and purification of the stalled 80S RNCs.

(A) Schematic representation of the poly(A) mRNA reporter comprising 49 consecutive adenines as a stall-inducing sequence used for the structural studies. (B) *In vitro* translation reaction (IN) using a yeast translation extract from a *ski2Δ* strain and subsequent affinity purification of His-tagged ribosome-nascent chain complexes. Fractions representing input (IN), flow through (FT), washing steps (W1 – W3), elution (E) and beads (B) were visualized by immunoblotting using anti-HA antibody. Peptidyl-tRNA (p-tRNA) band size is indicated. (C) The eluate was loaded on a 10-50 % sucrose gradient and fractionated. The indicated peaks representing the 80S and disome fractions were collected and concentrated using a sucrose cushion. Resuspended ribosomal pellets were used for cryo-EM sample preparation.

Appendix Figure S7. 3D classification and processing scheme of the 80S ribosomes stalled on the poly(A) reporter mRNA. The first 3D refined map was sorted into 6 classes. With the exception of classes 1 and 6 accounting for approximately 22% of particles, all other classes represented a vast majority of programmed ribosomal particles exhibiting the non-rotated post state. Class 3 was further subsorted sorting out a minor population of particles with both P/P and E/E tRNAs and two classes with P/P tRNA. These two classes were joined, resulting in a clean major population of particles with P/P tRNA. This particle category was further refined and processed as indicated (for details see Methods).

Appendix Figure S8. Local resolution and FSC curves for the 80S cryo-EM density maps of stalled ribosomes. Cryo-EM density maps filtered and colored according to local resolution as estimated by Relion 3 with Fourier Shell Correlation (FSC) plots for the refined and post-processed maps of 80S ribosomes stalled on the CGA-CCG (**A**), CGA-CGA (**B**) and poly(A) (**C**) mRNA reporters.

Appendix Figure S9. 3D classification and processing scheme of the disomes stalled on the poly(A) reporter mRNA. 740,637 80S particles were 3D refined and initially separated into eight classes partly representing different translational states of the ribosome. Class 4 represented the previously characterized poly(A) stalled 80S in the non-rotated post state with P/P tRNA. This class was further sub-classified, sorting out particles with no neighboring ribosome and revealing two subclasses with approximately the same share of particles. These two classes represented the first stalling and the second colliding ribosome judging by the density of the neighbor ribosome. Further processing of the first stalling post state ribosome (with neighbor density at mRNA exit) yielded a standard post-hybrid disome assembly. However, further processing of the second colliding ribosome in the post state (with neighbor density at mRNA entry) revealed a novel post-post disome assembly. The indicated processing procedure is described in more detail in Methods.

Appendix Figure S10. Local resolution and FSC curves for the individually refined 80S cryo-EM density maps of poly(A) stalled disomes. Cryo-EM density maps filtered and colored according to local resolution as estimated by Relion 3 with Fourier Shell Correlation (FSC) plots for the individually refined and post-processed maps of the first stalling **(A)** and second colliding **(B)** ribosomes stalled on the poly(A) mRNA reporter.

Methods

Ribosome Preparation

WT Ribosomes were purified and isolated as subunits as previously described ²⁷. Asc1 depleted ribosomes were purified similarly from strain AW768 (MATa his3- Δ 1, leu2- Δ 0, met15- Δ 0, ura3- Δ 0, asc1- Δ ::spHIS5, pURA3, ASC1) gifted from the Grayhack lab ³⁶.

Purification of translation factors

Translation initiation factors eIF1, eIF1A, eIF5, eIF5B were expressed and purified from *E. coli* and eIF2 was expressed and purified from *S. cerevisiae* as previously described ^{27, 57}. The translation elongation factor, eIF5A was purified from *E. coli* as previously described ^{28, 58}. The translation elongation factors eEF2 and eEF3 were purified from *S. cerevisiae* as previously described ²⁸.

Purification of amino-acyl synthetases

Plasmids gifted from the Grayhack lab containing the arginine and proline synthetases were transformed into BY4741 yeast strain and grown initially in CSM –ura glucose media (Sunrise Science) and induced in –ura galactose media overnight. Harvested cells grown in small scale (500 mL) were lysed by vortexing with acid washed glass beads (sigma) in extraction buffer (50mM Tris-Cl, pH 7.5, 1M NaCl, 1mM EDTA, 4mM MgCl₂,

5mM DTT, 10% glycerol). Larger scale preparations (2 L) were lysed by CryoMill and lysate was flowed over 5mL Ni column (GE) and batch eluted in 5 to 10 mLs (extraction buffer used for lysis with 5mM BME rather than DTT). Lysates were then diluted in IPP0 buffer (10mM Tris-Cl, pH 8, 0.1% NP40) and incubated for a minimum of 2 hours with IgG sepharose beads at 4°C. Beads were spun down at low speed (2 krpm) and unbound supernatant was removed. The beads were then washed with multiple times with IPP150 buffer (10 mM Tris-Cl, pH 8, 150mM NaCl, 0.1% NP40) to remove all unbound protein and washed subsequently with cleavage buffer (10 mM Tris-Cl, pH 8, 150 mM NaCl, 0.1% NP40, 0.5mM EDTA, 1 mM DTT). The protein was then cleaved from the beads using 3C protease in cleavage buffer overnight at 4°C. Cleaved protein was removed from beads, flash froze in small aliquots and stored at -80°C for use.

Purification of bulk yeast tRNA

tRNA isolation protocol was derived from a protocol to isolate RNA from *E. coli*⁵⁹ with minor changes and an added LiCl precipitation to remove rRNA and mRNA. Briefly, 3L of BY4741 yeast alone or expressing a plasmid of interest were grown to an OD600 of 1 and harvested by centrifugation. Cell pellets were resuspended in 20 mL Buffer A (50mM NaOAc, pH 7.5, 10mM MgOAc). Phenol:chloroform extraction of RNA and DNA was performed using an equal volume of acid phenol:chloroform, pH 4.5 (VWR). rRNA and mRNA was then pelleted by LiCl precipitation and tRNA and DNA was then ethanol precipitated. DNA was then removed by isopropyl alcohol precipitation. tRNA was then deacylated by incubation in 1M Tris-Cl, pH 9 for 3 hours at room temperature.

Deacylated tRNA was then purified by ethanol precipitation and resuspended in water for acylation and use in *in vitro* assays.

Purification and charging of tRNAs

Initiator methionine and lysine tRNAs were purchased from tRNA probes (College Station, TX). Phenylalanine tRNA was purchased from Sigma. Arginine and proline tRNAs were isolated from bulk yeast tRNA using 3' biotinylated oligonucleotides (listed below) as previously described ²⁹.

Oligo for A(I)CG-tRNA^{Arg} : 5' – CGC AGC CAG ACG CCG TGA CCA TTG GGC – 3'
Biotin

Oligo for UGG-tRNA^{Pro} : 5' – CCA AAG CGA GAA TCA TAC CAC TAG AC – 3' Biotin

Leu-2um plasmids for overexpressing native and exact match tRNAs were received from the Grayhack lab (ECB0873 ACG-tRNA^{Arg}, ECB0874 UCG-tRNA^{Arg}). tRNA sequences were moved to pRS316 vector by Gibson cloning for lower level overexpression. The low copy CEN plasmids containing the tRNA sequences were transformed into the BY4741 yeast strain. Bulk tRNA was then purified by the protocol above and the non-native tRNA was then isolated by the same 3' biotinylated oligonucleotide method previously ²⁹ using the specific oligonucleotides listed below.

Oligo for A(I)CG-tRNA^{Arg} : 5' – CGC AGC CAG ACG CCG TGA CCA TTG GGC – 3'
Biotin

Oligo for UCG-tRNA^{Arg} : 5' – CGA AGC CAG ACG CCG TGA CCA TTG GGC – 3'

Biotin

All isolated tRNAs were subjected to CCA addition as described previously⁵⁸. Isolated tRNA^{Lys} was charged using S100 extract and tRNA^{Phe}, tRNA^{Arg}, and tRNA^{Pro} were charged using purified synthetases as previously described with minor changes²⁷. Briefly, reactions contained 1X buffer 517 (30 mM HEPES-KOH pH 7.4, 30 mM KCl, 15 mM MgCl₂), 4 mM ATP, 5 mM DTT, 10-20 μM amino acid, 3 μM CCA-added tRNA and a 1/5 th volume of an S100 extract or 10 μM tRNA synthetase. Reactions were incubated at 30°C for 30 minutes, then extracted twice with acid phenol and once with chloroform. tRNA was precipitated with ethanol, resuspended in 20 mM KOAc, 2 mM DTT, pH 5.2, and stored in small aliquots at -80°C.

***In vitro* 80S initiation complex formation**

80S initiation complexes were formed as previously described²⁸ with minor differences. Briefly, 3 pmol of 35S-Met-tRNA^{iMet} was mixed with 50 pmol of eIF2 and 1 mM GTP in 1X Buffer E (20 mM Tris pH 7.5, 100 mM KOAc pH 7.6, 2.5 mM Mg(OAc)₂, 0.25 mM Spermidine, and 2 mM DTT) for 10 min at 26°C. Next a mixture containing 25 pmol 40S subunits, 200 pmol mRNA (purchased from IDT), 125 pmol eIF1, and 125 pmol eIF1A in 1X Buffer E was added for 5 min. To form the 80S complex, a mixture containing 25 pmol 60S subunits, 150 pmol eIF5, 125 pmol eIF5b, and 1 mM GTP in 1X Buffer E was added for 1 min. Complexes were then mixed 1:1 with buffer E containing 17.5 mM Mg(OAc)₂ to yield a final magnesium concentration of 10 mM.

Ribosomes were then pelleted through a 600 μ L sucrose cushion containing 1.1 M sucrose in buffer E with 10 mM Mg(OAc)₂ using a MLA-130 rotor (Beckmann) at 75,000 rpm for 1 hr at 4°C. After pelleting, ribosomes were resuspended in 15-25 μ L of 1X Buffer E containing 10 mM Mg(OAc)₂ and stored at -80°C.

***In vitro* reconstituted translation elongation**

Translation elongation reactions were performed as previously described^{27, 28} with minor differences. Briefly, aa-tRNA ternary complex was formed by incubating aa-tRNA (1.5 - 2 μ M), eEF1A (5 μ M), 1 mM GTP, in 1X Buffer E for 10 minutes at 26°C. Limited amounts of 80S initiation complexes (3 nM) were then mixed with aa-tRNA ternary complex (varying concentrations), eEF2 (500 nM), eEF3 (1 μ M), eIF5A (1 μ M), ATP (3 mM) and GTP (2 mM). Reactions were incubated at 26°C and time points quenched into 500mM KOH. Samples were diluted 1 μ L into 3 μ L water before monitoring peptide formation electrophoretic TLC (Millipore). TLC plates were equilibrated with pyridine acetate buffer (5 mL pyridine, 200 mL acetic acid in 1 L, pH 2.8) before electrophoresis at 1200 V for 25 to 30 minutes. Plates were developed using a Typhoon FLA 9500 Phosphorimager system (GE Healthcare Life Sciences) and quantified using ImageQuantTL (GE Healthcare Life Sciences). Time courses were fit to single exponential kinetics using Kaleidagraph (Synergy Software).

***In vitro* Met-Puromycin assay**

Reactions were set up as previously described²⁸. Reactions were performed for each set of initiation complexes made and used to normalize peptide formation from elongation. Briefly, 2 nM initiation complexes and 1 μ M eIF5A in 1X Buffer E (20 mM Tris pH 7.5, 100 mM KOAc pH 7.6, 2.5 mM Mg(OAc)₂, 0.25 mM Spermidine, and 2 mM DTT) were incubated at 26°C in the presence of 4 mM puromycin. Time points over the course of 120 min were quenched into 500 mM KOH and analyzed by electrophoretic TLC (Millipore). TLC plates were equilibrated with pyridine acetate buffer (5 mL pyridine, 200 mL acetic acid in 1 L, pH 2.8) before electrophoresis at 1200 V for 25 min. Plates were developed using a Typhoon FLA 9500 Phosphorimager system (GE Healthcare Life Sciences) and quantified using ImageQuantTL (GE Healthcare Life Sciences).

***In vitro* PTH assay to access peptidyl-tRNA drop-off**

Translation elongation reactions were performed in the presence of 27 μ M peptidyl-tRNA hydrolase (PTH) to monitor drop-off of peptidyl-tRNAs from translating ribosomes as described previously²⁸. Time points for drop-off products were quenched with 10% formic acid and were analyzed by electrophoretic TLC in pyridine acetate buffer (see above) at 1200 V for 30 minutes.

Preparation of ribosome footprint libraries and analysis of aligned footprints

WT and Δ asc1 cells were grown to OD ~ 0.5 in 1 L of YPD media (sample 1) or transferred to YPGR media (2% galactose and 2% raffinose) for 6 hr (sample 2) and harvested by fast filtration followed by flash frozen in liquid nitrogen. Cell pellets were ground with 1 mL footprint lysis buffer [20 mM Tris-Cl (pH8.0), 140 mM KCl, 1.5 mM MgCl₂, 1% Triton X-100 0.1 mg/mL CHX, 0.1 mg/mL TIG] in a Spex 6870 freezer mill. Lyzed cell pellets were diluted to 15 mL in footprint lysis buffer and clarified by centrifugation. Polysomes were isolated from sucrose cushions for library construction as described previously³⁴.

3' adapter (NNNNNNCACTCGGGCACCAAGGA) was trimmed, and 4 random nucleotides included in RT primer were removed from the 5' end of reads (RNNNAGATCGGAAGAGCGTCGTGTAGGGAAAGAGTGTAGATCTCGGTGGTC GC/iSP18/TTCAGACGTGTGCTCTTCCGATCTGTCCTTGGTGCCCGAGTG).

Trimmed reads longer were aligned to yeast ribosomal and non-coding RNA sequence. Unmapped reads were mapped to R64-1-1 S288C reference genome assembly (SacCer3) from the *Saccharomyces* Genome Database Project using STAR⁶⁰ as described previously³⁴. Data shown in Figs 3 and 4 for WT are identical to those published previously³⁴. Relative ribosome occupancies for codon pairs were computed by taking the ratio of the ribosome density in a 3-nt window at the di-codon over the density in the coding sequence (excluding the first and the last 15 nt).

Preparation of stalled ribosome-nascent chain complexes

We generated a series of mRNA reporters containing three different stalling sequences (CGA-CCG)₂, (CGA-CGA)₂, and poly(A) (Appendix Figs S1A, S2A and S6A). These sequences were placed downstream of a sequence coding for TEV-cleavable N-terminal His- and HA tags and the first 64 amino acid residues of truncated uL4. Corresponding mRNAs were produced using the mMessage mMachine Kit (Thermo Fischer) utilizing an upstream T7 promoter and translated in a yeast cell-free translation extract from *ski2Δ* cells.

This yeast translation extract was prepared, and *in vitro* translation was performed essentially as described before⁶¹. In brief, the cells were grown in YPD medium to OD₆₀₀ of 1.5–2.0. Spheroplasts were prepared from harvested washed cells using 10 mM DTT for 15 min at room temperature and 2.08 mg zymolyase per 1 g of cell pellet for 75 min in 1 M sorbitol at 30°C. Spheroplasts were then washed and lysed in a Dounce homogenizer as described⁶¹ before using lysis buffer comprising 20 mM Hepes pH 7.5, 100 mM KOAc, 2 mM Mg(OAc)₂, 10% glycerol, 1 mM DTT, 0.5 mM PMSF and complete EDTA-free protease inhibitors (GE Healthcare). The S100 fraction of lysate supernatant was passed through PD10 column (GE Healthcare) and used for *in vitro* translation. *In vitro* translation was performed at 17°C for 75 min using great excess of template mRNA (38 μg per 415 μl of extract) to prevent degradation of resulting stalled ribosomes by endogenous response factors.

Respective stalled RNCs were affinity-purified using the His₆-tag of the nascent polypeptide chain essentially as described before^{43,62}. After *in vitro* translation, the extract was applied to Ni-NTA DynabeadsTM (Invitrogen) and incubated while rotating for 15 min

at 4°C. The beads were washed three times with excess of a wash buffer containing 50 mM HEPES/KOH, pH 7.5, 100 mM KOAc, 25 mM Mg(OAc)₂, 250 mM sucrose, 0.1% Nikkol and 5 mM β-Mercaptoethanol and eluted in 400 μl of the same buffer containing 300 mM imidazole. The elution was applied to a 10-50% sucrose gradient in wash buffer, and ribosomal fractions were separated by centrifugation for 3 h at 172,000 g at 4°C in a SW40 rotor. For gradient fractionation, a Piston Gradient Fractionator™ (BIOCOMP) was used. The 80S (mono)ribosome (and for poly(A) also the disome) fractions were collected, applied onto 400 μl of sucrose cushion buffer and spun at 534,000 g for 45 min at 4°C in a TLA110 rotor. The resulting ribosomal pellets were resuspended carefully on ice in 25 μl of grid buffer (20 mM HEPES/KOH, pH 7.2, 50 mM KOAc, 5 mM Mg(OAc)₂, 125 mM sucrose, 0.05% Nikkol, 1 mM DTT and 0.01 U/μl SUPERase-IN™ (Invitrogen).

Collected 80S fractions of CGA-CCG and CGA-CGA stalled RNCs were also subjected to puromycin reactions with 1 mM puromycin at 20°C. Time point samples were heated 5 minutes at 60°C with reducing sample buffer and analyzed by SDS-PAGE and western blotting.

Electrophoresis and Western blotting

Protein samples of *in vitro* translation reactions and subsequent purifications were separated on SDS-PAGE at neutral pH condition (pH 6.8, for purified protein samples) and were transferred on PVDF membrane (Immobilon-P, Millipore). After blocking with 5% skim milk in PBS-T, the membranes were incubated with anti-HA-peroxidase antibody (1:5,000; Roche, Cat# 12013819001, clone 3F10) for 1 h at room temperature followed by

washing with PBS-T for three times. Chemiluminescence was detected using SuperSignal® substrate (Thermo Fischer) in a LAS4000 mini (GE Healthcare).

Cryo-EM

Freshly prepared samples (stalled monosomes or disomes) were applied to 2 nm pre-coated Quantifoil R3/3 holey carbon support grids and vitrified. Data were collected at Titan Krios TEM (Thermo Fisher) equipped with a Falcon II direct detector at 300 keV under low-dose conditions of about 25 e-/Å² for 10 frames in total and defocus range of -1.3 to -2.8 μm. Magnification settings resulted in a pixel size of 1.084 Å/pixel. In the case of CGA-CGA RNCs, a higher magnification was used resulting in a pixel size of 0.847 Å/pixel. Original image stacks were summed and corrected for drift and beam-induced motion at the micrograph level by using MotionCor2⁶³. The Contrast transfer function (CTF) estimation and resolution range of each micrograph were performed with Gctf⁶⁴.

Cryo-EM Data processing

All datasets were processed using standard procedures with programs GAUTOMATCH (<http://www.mrc-lmb.cam.ac.uk/kzhang/>) used for particle picking and RELION-3 for data processing and 3D reconstruction⁶⁵. For each dataset, picked particles were extracted for 2D classification using a box of 400 pixels rescaled to 70 pixels. After selection of suitable 2D classes, particles were extracted for initial 3D refinement followed by 3D classification using a box of 400 pixel rescaled to 120 pixels and a mask diameter of 300 Å.

The CGA-CCG dataset was described before with focus on the Xrn1 factor bound⁶². We now re-processed this dataset with focus on the ribosome itself. Individual translation states were separated as before with around 60% of the particles containing tRNAs in the P/P and E/E conformation (Appendix Fig S3). These classes were joined and separated into four subclasses sorting out low resolution particles. Further subclassification was performed using a mask covering tRNAs. This approach sorted out a population of particles without the E site tRNA. The cleaned population of particles was further processed using particle CTF refinement yielding a final resolution of 2.6 Å. This cryo-EM density map was filtered according to local resolution and used for interpretation (Appendix Fig S8A).

For the CGA-CGA dataset, 840,234 particles were used after 2D classification and sorted into six classes in 3D classification. A vast majority of programmed ribosomal particles in the dataset were found in the post translocation state while a single class containing tRNAs in P/P E/E conformation represented 39.9% of the whole dataset (Appendix Fig S4). As further classification of this class was mainly yielding volumes sorted based on position of expansion segment 27 on the periphery of the ribosome, the class was further processed as a whole. The final cryo-EM density map reaching an overall resolution of 3.2 Å after particle CTF refinement was filtered according to local resolution and used for interpretation (Appendix Fig S8B).

For the poly(A) 80S dataset, 840,234 particles were used after 2D classification and sorted into six classes in 3D classification (Appendix Fig S7). Analogous to previous datasets, a vast majority of programmed ribosomal particles represented classes in the post translocation state. Class 3 containing tRNAs in P/P E/E conformation was subsorted based

on tRNA presence into classes containing only P/P tRNA and a class containing both P/P and E/E tRNAs. The dominant classes of P/P tRNA state were joined and further processed using particle CTF refinement and Bayesian polishing. The resulting cryo-EM density map reached an overall resolution of 3.1 Å. This volume was subjected to focused refinement using a mask covering the 60S subunit and the decoding center. This yielded a better resolved density map (3.0 Å) in the region of interest and was used for interpretation after filtering according to local resolution (Appendix Fig S8C).

Reconstruction of the poly(A) disome

The poly(A) disome dataset was collected as described above. The dataset was processed using the “80S extension” approach as described previously⁴³. Initial 3D classification yielded in a class of ribosomes in the POST state with P/P tRNA as described above for the poly(A) monosome. Surprisingly, subsorting of this class revealed that approximately the same share of particles in this class represented the first stalling and the second colliding ribosome judging by the density of the neighboring ribosome close to the mRNA entry and exit site, respectively (Appendix Fig S9). Further processing of the leading POST state ribosome (with neighbor density at mRNA exit) yielded a standard POST-PRE hybrid disome assembly as observed for the CGA-CCG-stalled disome⁴³. On the other hand, processing of the second colliding ribosome in the POST state (with neighbor density at mRNA entry) revealed a novel POST-POST disome assembly. Both these volumes were obtained by stepwise box extension and refinement with particle re-centering (first 500 pixels rescaled to 120 pixels followed by 700 pixels rescaled to 506 pixels). Soft masks covering individual ribosomal bodies were used for multi-body

refinement to obtain a more detailed information ⁶⁶. The resulting volumes were filtered according to local resolution (Appendix Fig S10) and fitted into the consensus refinement yielding a composite cryo-EM density map at 3.8 Å overall resolution.

Model building

To generate molecular models for our structures, we used our previously refined models for stalled yeast ribosomes ⁶² PDB ID: 6Q8Y and ⁴³ PDB ID: 6I7O). First, individual subunits and tRNAs were fitted as rigid bodies into the densities. These models were then refined and remodeled in COOT ⁶⁷ and Phenix ⁶⁸. Cryo-EM structures and models were displayed with UCSF Chimera ⁶⁹ and ChimeraX ⁷⁰.

Data availability

The cryo-EM structures reported here have been deposited in the Protein Data Bank and in the Electron Microscopy Data Bank. Ribosome profiling datasets have been deposited under GSE136202 (reviewer access with secure token: mfwfweqatvmlfkt).

References

1. Gingold, H. & Pilpel, Y. Determinants of translation efficiency and accuracy. *Molecular systems biology* **7**, 481 (2011).
2. Tuller, T., Waldman, Y.Y., Kupiec, M. & Ruppin, E. Translation efficiency is determined by both codon bias and folding energy. *Proceedings of the National Academy of Sciences of the United States of America* **107**, 3645-3650 (2010).
3. Presnyak, V. *et al.* Codon optimality is a major determinant of mRNA stability. *Cell* **160**, 1111-1124 (2015).
4. Pechmann, S. & Frydman, J. Evolutionary conservation of codon optimality reveals hidden signatures of cotranslational folding. *Nature structural & molecular biology* **20**, 237-243 (2013).
5. Thanaraj, T.A. & Argos, P. Ribosome-mediated translational pause and protein domain organization. *Protein science : a publication of the Protein Society* **5**, 1594-1612 (1996).
6. Elf, J., Nilsson, D., Tenson, T. & Ehrenberg, M. Selective charging of tRNA isoacceptors explains patterns of codon usage. *Science (New York, N.Y.)* **300**, 1718-1722 (2003).
7. Dana, A. & Tuller, T. The effect of tRNA levels on decoding times of mRNA codons. *Nucleic acids research* **42**, 9171-9181 (2014).
8. Burgess-Brown, N.A. *et al.* Codon optimization can improve expression of human genes in Escherichia coli: A multi-gene study. *Protein expression and purification* **59**, 94-102 (2008).
9. dos Reis, M., Savva, R. & Wernisch, L. Solving the riddle of codon usage preferences: a test for translational selection. *Nucleic acids research* **32**, 5036-5044 (2004).
10. Sharp, P.M. & Li, W.H. The codon Adaptation Index--a measure of directional synonymous codon usage bias, and its potential applications. *Nucleic acids research* **15**, 1281-1295 (1987).
11. Quax, T.E., Claassens, N.J., Söll, D. & van der Oost, J. Codon Bias as a Means to Fine-Tune Gene Expression. *Molecular cell* **59**, 149-161 (2015).
12. Brule, C.E. & Grayhack, E.J. Synonymous Codons: Choose Wisely for Expression. *Trends in genetics : TIG* **33**, 283-297 (2017).
13. Gamble, C.E., Brule, C.E., Dean, K.M., Fields, S. & Grayhack, E.J. Adjacent Codons Act in Concert to Modulate Translation Efficiency in Yeast. *Cell* **166**, 679-690 (2016).
14. Letzring, D.P., Dean, K.M. & Grayhack, E.J. Control of translation efficiency in yeast by codon-anticodon interactions. *RNA (New York, N.Y.)* **16**, 2516-2528 (2010).
15. Arthur, L.L. & Djuranovic, S. PolyA tracks, polybasic peptides, poly-translational hurdles. *Wiley Interdiscip Rev RNA*, e1486 (2018).
16. Frischmeyer, P.A. *et al.* An mRNA surveillance mechanism that eliminates transcripts lacking termination codons. *Science* **295**, 2258-2261 (2002).
17. Ozsolak, F. *et al.* Comprehensive polyadenylation site maps in yeast and human reveal pervasive alternative polyadenylation. *Cell* **143**, 1018-1029 (2010).
18. Brandman, O. & Hegde, R.S. Ribosome-associated protein quality control. *Nature structural & molecular biology* **23**, 7-15 (2016).
19. Joazeiro, C.A.P. Mechanisms and functions of ribosome-associated protein quality control. *Nat Rev Mol Cell Biol* **20**, 368-383 (2019).
20. Lu, J. & Deutsch, C. Electrostatics in the ribosomal tunnel modulate chain elongation rates. *J Mol Biol* **384**, 73-86 (2008).
21. Koutmou, K.S. *et al.* Ribosomes slide on lysine-encoding homopolymeric A stretches. *Elife* **4** (2015).
22. Letzring, D.P., Wolf, A.S., Brule, C.E. & Grayhack, E.J. Translation of CGA codon repeats in yeast involves quality control components and ribosomal protein L1. *RNA (New York, N.Y.)* **19**, 1208-1217 (2013).
23. Arthur, L. *et al.* Translational control by lysine-encoding A-rich sequences. *Sci Adv* **1** (2015).
24. Juszkiwicz, S. *et al.* ZNF598 Is a Quality Control Sensor of Collided Ribosomes. *Molecular cell* **72**, 469-515032704 (2018).

25. Ikeuchi, K. *et al.* Collided ribosomes form a unique structural interface to induce Hel2-driven quality control pathways. *The EMBO journal* (2019).
26. Simms, C.L., Yan, L.L. & Zaher, H.S. Ribosome Collision Is Critical for Quality Control during No-Go Decay. *Molecular cell* **68**, 361-373 (2017).
27. Eyler, D.E. & Green, R. Distinct response of yeast ribosomes to a miscoding event during translation. *RNA* **17**, 925-932 (2011).
28. Schuller, A.P., Wu, C.C., Dever, T.E., Buskirk, A.R. & Green, R. eIF5A Functions Globally in Translation Elongation and Termination. *Molecular cell* **66**, 194-205 (2017).
29. Yokogawa, T., Kitamura, Y., Nakamura, D., Ohno, S. & Nishikawa, K. Optimization of the hybridization-based method for purification of thermostable tRNAs in the presence of tetraalkylammonium salts. *Nucleic acids research* **38** (2010).
30. Murphy, F.V. & Ramakrishnan, V. Structure of a purine-purine wobble base pair in the decoding center of the ribosome. *Nat Struct Mol Biol* **11**, 1251-1252 (2004).
31. Shoemaker, C.J., Eyler, D.E. & Green, R. Dom34:Hbs1 Promotes Subunit Dissociation and Peptidyl-tRNA Drop-Off to Initiate No-Go Decay. *Science* **330**, 369-372 (2010).
32. Zaher, H.S. & Green, R. Fidelity at the Molecular Level: Lessons from Protein Synthesis. *Cell* **136**, 746-762 (2009).
33. Gromadski, K.B. & Rodnina, M.V. Kinetic determinants of high-fidelity tRNA discrimination on the ribosome. *Molecular cell* **13**, 191-200 (2004).
34. Wu, C.C., Zinshteyn, B., Wehner, K.A. & Green, R. High-Resolution Ribosome Profiling Defines Discrete Ribosome Elongation States and Translational Regulation during Cellular Stress. *Molecular cell* (2019).
35. Matsuo, Y. *et al.* Ubiquitination of stalled ribosome triggers ribosome-associated quality control. *Nature communications* **8**, 159 (2017).
36. Wolf, A.S. & Grayhack, E.J. Asc1, homolog of human RACK1, prevents frameshifting in yeast by ribosomes stalled at CGA codon repeats. *RNA (New York, N.Y.)* **21**, 935-945 (2015).
37. Wang, J., Zhou, J., Yang, Q. & Grayhack, E.J. Multi-protein bridging factor 1 (Mbf1), Rps3 and Asc1 prevent stalled ribosomes from frameshifting. *eLife* **7** (2018).
38. Knorr, A.G. *et al.* Ribosome-NatA architecture reveals that rRNA expansion segments coordinate N-terminal acetylation. *Nat Struct Mol Biol* **26**, 35-39 (2019).
39. Schmidt, C. *et al.* The cryo-EM structure of a ribosome-Ski2-Ski3-Ski8 helicase complex. *Science* **354**, 1431-1433 (2016).
40. Keedy, H.E., Thomas, E.N. & Zaher, H.S. Decoding on the ribosome depends on the structure of the mRNA phosphodiester backbone. *Proc Natl Acad Sci U S A* **115**, E6731-E6740 (2018).
41. Tang, T.T.L., Stowell, J.A.W., Hill, C.H. & Passmore, L.A. The intrinsic structure of poly(A) RNA determines the specificity of Pan2 and Caf1 deadenylases. *Nat Struct Mol Biol* **26**, 433-442 (2019).
42. Juszkiwicz, S. *et al.* ZNF598 Is a Quality Control Sensor of Collided Ribosomes. *Mol Cell* **72**, 469-481 (2018).
43. Ikeuchi, K. *et al.* Collided ribosomes form a unique structural interface to induce Hel2-driven quality control pathways. *EMBO J* **38** (2019).
44. Yarus, M. & Folley, L.S. Sense codons are found in specific contexts. *Journal of molecular biology* **182**, 529-540 (1985).
45. Fedorov, A., Saxonov, S. & Gilbert, W. Regularities of context-dependent codon bias in eukaryotic genes. *Nucleic acids research* **30**, 1192-1197 (2002).
46. Limoncelli, K.A., Merrikh, C.N. & Moore, M.J. ASC1 and RPS3: new actors in 18S nonfunctional rRNA decay. *RNA (New York, N.Y.)* **23**, 1946-1960 (2017).
47. Simms, C.L., Kim, K.Q., Yan, L.L., Qiu, J. & Zaher, H.S. Interactions between the mRNA and Rps3/uS3 at the entry tunnel of the ribosomal small subunit are important for no-go decay. *PLoS genetics* **14** (2018).
48. Ikeuchi, K. & Inada, T. Ribosome-associated Asc1/RACK1 is required for endonucleolytic cleavage induced by stalled ribosome at the 3' end of nonstop mRNA. *Scientific reports* **6**, 28234 (2016).
49. Rozov, A. *et al.* Importance of potassium ions for ribosome structure and function revealed by long-wavelength X-ray diffraction. *Nat Commun* **10**, 2519 (2019).
50. Selmer, M. *et al.* Structure of the 70S ribosome complexed with mRNA and tRNA. *Science* **313**, 1935-1942 (2006).

51. Agirrezabala, X. *et al.* Ribosome rearrangements at the onset of translational bypassing. *Sci Adv* **3**, e1700147 (2017).
52. Gerber, A.P. & Keller, W. An adenosine deaminase that generates inosine at the wobble position of tRNAs. *Science* **286**, 1146-1149 (1999).
53. Presnyak, V. *et al.* Codon optimality is a major determinant of mRNA stability. *Cell* **160**, 1111-1124 (2015).
54. Simms, C.L., Yan, L.L., Qiu, J.K. & Zaher, H.S. Ribosome Collisions Result in +1 Frameshifting in the Absence of No-Go Decay. *Cell Rep* **28**, 1679-1689 e1674 (2019).
55. Dinman, J.D. Mechanisms and implications of programmed translational frameshifting. *Wiley Interdiscip Rev RNA* **3**, 661-673 (2012).
56. Baranov, P.V., Gesteland, R.F. & Atkins, J.F. P-site tRNA is a crucial initiator of ribosomal frameshifting. *RNA* **10**, 221-230 (2004).
57. Acker, M.G., Kolitz, S.E., Mitchell, S.F., Nanda, J.S. & Lorsch, J.R. Reconstitution of yeast translation initiation. *Methods in enzymology* **430**, 111-145 (2007).
58. Gutierrez, E. *et al.* eIF5A promotes translation of polyproline motifs. *Molecular cell* **51**, 35-45 (2013).
59. Ehrenstein, G. [76] *Isolation of sRNA from intact Escherichia coli cells*, Vol. 12. (Elsevier, 1967).
60. Dobin, A. *et al.* STAR: ultrafast universal RNA-seq aligner. *Bioinformatics (Oxford, England)* **29**, 15-21 (2013).
61. Waters, M.G. & Blobel, G. Secretory protein translocation in a yeast cell-free system can occur posttranslationally and requires ATP hydrolysis. *J Cell Biol* **102**, 1543-1550 (1986).
62. Tesina, P. *et al.* Structure of the 80S ribosome-Xrn1 nuclease complex. *Nat Struct Mol Biol* **26**, 275-280 (2019).
63. Zheng, S.Q. *et al.* MotionCor2: anisotropic correction of beam-induced motion for improved cryo-electron microscopy. *Nature methods* **14**, 331-332 (2017).
64. Zhang, K. Gctf: Real-time CTF determination and correction. *Journal of structural biology* **193**, 1-12 (2016).
65. Zivanov, J. *et al.* New tools for automated high-resolution cryo-EM structure determination in RELION-3. *Elife* **7** (2018).
66. Nakane, T., Kimanius, D., Lindahl, E. & Scheres, S.H. Characterisation of molecular motions in cryo-EM single-particle data by multi-body refinement in RELION. *Elife* **7** (2018).
67. Brown, A. *et al.* Tools for macromolecular model building and refinement into electron cryo-microscopy reconstructions. *Acta crystallographica. Section D, Biological crystallography* **71**, 136-153 (2015).
68. Adams, P.D. *et al.* PHENIX: a comprehensive Python-based system for macromolecular structure solution. *Acta crystallographica. Section D, Biological crystallography* **66**, 213-221 (2010).
69. Pettersen, E.F. *et al.* UCSF Chimera--a visualization system for exploratory research and analysis. *Journal of computational chemistry* **25**, 1605-1612 (2004).
70. Goddard, T.D. *et al.* UCSF ChimeraX: Meeting modern challenges in visualization and analysis. *Protein Sci* **27**, 14-25 (2018).

Chapter 3: Development of a single molecule system to investigate the molecular mechanisms of translation termination, ribosome rescue and recycling

Abstract

Translation termination and recycling as well as ribosome rescue are crucial steps in translation that are required for continued cell viability replenishing the pool of ribosomes available to make proteins throughout the cell. While years of structural and biochemical studies have provided detailed information into these processes, single molecule fluorescence studies have begun to help sort out the more detailed mechanistic pathways involved. To develop a single molecule assay to investigate these processes we began with the fluorescent labeling of the ribosome and the factors involved in termination, rescue and recycling. Using an *in vitro* biochemical system in yeast, all the labeled factors were then tested for functionality before performing the more in-depth single molecule studies. Initial experiments observing canonical translation termination have begun to reveal complex interactions between eRF1, eRF3 and the ribosome. With this assay set up and the functional protein factors labeled we hope to perform a more comprehensive investigation into the similarities and differences between canonical translation termination and recycling and ribosome rescue.

Introduction

Dynamic processes throughout cells are traditionally measured using bulk methods on large numbers of molecules in solution. While these experiments have provided us a wealth of information regarding the processes of translation, some information is lost due to ensemble averaging. Single molecule methods allow instead for individual molecules to be tracked to tease out the details of these highly dynamic processes¹⁻³. Fluorescence spectroscopy is a vital tool to track and further understand biological phenomena. In order to use single molecule fluorescence approaches, the biological molecules to be studied must first be labeled with bright, stable dyes. These organic dyes allow for the emission of millions of photons before they undergo irreversible photochemical and photophysical processes that lead to termination of fluorescence (photobleaching)⁴. Further understanding of the properties of these dyes has led to the development of even brighter and more stable dyes for use in single molecule experiments^{5, 6}.

To further distinguish the fluorescence signal of interest for single molecule experiments from background or noise, total internal reflection fluorescence (TIRF) and zero mode waveguide (ZMW) techniques are frequently used⁷⁻⁹. TIRF microscopy creates an evanescent field that only extends ~100 nm above the surface therefore limiting the fluorescent molecules in solution from being excited. ZMWs, on the other hand, reduce the excitation volume by orders of magnitude to allow the use of higher concentrations of fluorescently labeled ligands. For both of these techniques to be successful, the biomolecules to be studied are spatially constrained to the surface of a slide or coverslip.

In translation experiments, surface immobilization is often done using biotin and streptavidin interactions on mRNAs or ribosomes.

Through the use of these techniques and multiple colored dyes two main types of single molecule analysis can be performed – localization and Förster resonance energy transfer (FRET). Localization experiments can be performed without having to synchronize the biomolecules in the experiment. Instead, postsynchronization is performed by aligning single molecule traces to a defined zero time point. This can be done for many differentially labeled molecules which can then be sorted from one another to track multiple events^{1, 10}. Through the use of this analysis method the order of binding events, and the kinetics of association and dissociation of different molecules, as well as the binding overlap between molecules can be directly visualized and measured¹¹. Single molecule FRET experiments, on the other hand, allow for the investigation of conformational dynamics as the efficiency of energy transfer between a donor and acceptor dye depend on the relationship $1/R^6$ where R is the distance between the dyes^{7, 12, 13}. FRET efficiency varies from 1 (when all energy is transferred from the donor to the acceptor) below distances of ~20 Å to 0 (no energy transfer occurs) at distances above ~80 Å¹⁴. This method is therefore highly sensitive to conformational changes in the range of 30 to 70 Å which is especially well suited for translational studies of the ribosome (diameter ~250 Å)^{1, 2}. Single molecule experiments have greatly enhanced our knowledge of translation events over the past two decades especially in prokaryotes and now beginning to expand further to eukaryotes and live cell imaging¹⁵⁻²².

As reviewed in chapter 1, the processes of translation termination, ribosome rescue and recycling in eukaryotes are complex, dynamic processes that involve many different

factors. The canonical termination factors eRF1 and eRF3 recognize stop codons at the ends of ORFs, whereas the homologous rescue factors DOM34 and HBS1 recognize stalled ribosomes. In both cases the ribosomes then need to be recycled back to the cytoplasm for continued translation on other mRNA transcripts^{23, 24}. Many mechanistic questions regarding the ordering, timing and interactions between these factors during termination, rescue and recycling remain to be answered. Through the development of a single molecule fluorescence system for eukaryotic translation termination, rescue and recycling using the model system *S. cerevisiae*, we hope to begin to deepen our understanding of these processes.

Results

Construction of single molecule TIRF microscope for 3 color visualization

In order to measure the kinetic processes of translation via smTIRF, we first had to setup a microscope capable of this type of visualization. The microscope we began with in the laboratory of Dr. James Berger, an objective based TIRF system, had a single excitation laser at 532 nm. This was a starting point, but many of the experiments we planned to do would require more than one color to follow multiple crucial components in the processes of translation termination, ribosome rescue and ribosome recycling. We first added an excitation laser at 640 nm. This wavelength was chosen based on the fluorescent properties of readily available organic dyes as well as its suitability for FRET experiments with the 532 nm laser. The excitation pathway of the microscope was constructed based on previously published protocols^{25, 26}. The emission pathway was constructed using an

OptoSplit device (Cairn Research Ltd). This device contains built in mirrors with set positions for filters to separate the emission pathways corresponding to the two lasers (Figure 1). We were also able to add a third laser with the excitation wavelength of 488 nm to expand the capabilities of this system further.

Sample chamber preparation

In order to move towards observing processes of translation via single molecule fluorescence we had to have an efficient and specific way to immobilize substrates onto the surface of a coverslip and a system to quickly deliver sample onto the surface. First, the surface of the glass slide and coverslip needed to be cleaned of fluorescent impurities. Two methods were used to clean the slides and coverslips. One is the first step, or organic and particle cleaning step, of the RCA cleaning method often used on silicon wafers²⁷ (detailed in the methods section). The second method used was oxygen plasma cleaning (Harrick Plasma). Coverslips showed similar levels of background fluorescence using either cleaning method (Figure 2A).

Following cleaning of the surface, coverslips needed to be functionalized to allow the specific attachments of biomolecules of interest²⁸. First, the glass surface of the coverslips were amino-modified and then the amine covered glass surface was coated with PEG. Ratios of biotinylated and non-biotinylated PEG were added to allow the specific attachment of biotinylated molecules through the interaction with streptavidin or neutravidin while also minimizing the non-specific interactions of other biomolecules with the surface of the glass coverslip (Figure 2B).

Finally, an efficient and fast method to deliver sample onto the surface of the coverslip was needed to later perform experiments involving many different factors involved in translation termination, rescue and ribosome recycling. Sample chambers were assembled using NanoPort assemblies (IDEX Health & Science) epoxied to the surface of the slide with the functionalized coverslip epoxied to the opposite slide surface for biomolecule visualization (Figure 2C). These assemblies allowed for the efficient introduction of sample without leaking using a syringe and syringe pump to minimize the volume of sample needed. The cleaning, functionalization and assembly of slides allowed for the specific visualization of biotinylated molecules on the surface of the coverslips by objective-based TIRF microscopy.

Ribosome labeling and function tests

To be able to follow the steps of translation, we needed to be able to visualize the catalytic core of these processes – the ribosome. Working with our collaborators, we received a construct with a SNAP tag incorporated at the N-terminus of the ribosomal protein RPL5 on the 60S subunit of the yeast ribosome (Figure 3A). The SNAP tag is a 20 kDa mutant of the human DNA repair protein, O6-alkylguanine- DNA alkyltransferase that reacts specifically with benzylguanine derivatives. When organic dye derivatives are made with a benzylguanine modification, the SNAP tag is covalently labeled with a fluorescent probe²⁹⁻³². The incorporation of this tag into the large subunit of the ribosome will allow for the purification of specifically labeled ribosomal subunits (see methods for purification details).

A major concern when labeling proteins with any tag, especially large ones, is that the tag will inhibit the natural function of the protein itself. Therefore, it is necessary to test the specific activity of the labeled construct as compared to a functional, unlabeled protein. To test the activity of ribosomes labeled with the SNAP tag, initiation complexes (ICs) were first assembled using our *in vitro* reconstituted yeast translation system. ICs were prepared stepwise using labeled 60S subunits on a simple MFX mRNA with [³⁵S]-Met-tRNA^{iMet} loaded in the ribosomal P site. Pelleted ICs were then mixed with elongation factor eEF1A and Phe-tRNA^{Phe}, quenching time points of the peptide transfer reaction using KOH and then running formed peptide products on electrophoretic TLC (Figure 3B). Quantifying the amount of MF product formed allowed the functional comparison of labeled and unlabeled 60S subunits (Figure 3D, E). From these experiments we can conclude that our labeled ribosomes are as functional as their unlabeled counterparts and are therefore able to be used for single molecule studies.

Single molecule visualization of initiation complexes with labeled ribosomes

To allow for single molecule visualization of ICs the constructs were modified by initiating on similar MF-Stop or M-Stop mRNAs with a biotin at their 5' end and non-radioactive Met-tRNA^{iMet} in the P-site (Figure 4A). These ICs with DY-549 dye (NEB) incorporated in the large subunit of the ribosome were flowed onto functionalized coverslips in a buffer containing oxygen scavengers and triplet state quenchers to minimize blinking and delay photobleaching of the fluorophores in solution^{4, 33-35}. The unbound complexes were then removed by washing and the bound complexes were visualized after excitation with the 532 nm laser. Individually labeled ICs were clearly observed on the

coverslip surface, but were photobleaching at a rapid rate (Figure 4B). This fast photobleaching is problematic for the ribosome termination, rescue and recycling events we are hoping to measure given previously published rates for these processes from bulk experiments³⁶⁻³⁸.

To increase the lifetime of the fluorophores in our experiments we began using “ultra-stable” organic dyes to label our ribosomal subunits^{5, 39} and began using a dye excited by the 640 nm laser as this channel has less fluorescent background. We received this dye from the Blanchard lab (Cy5-M-BG) which is a Cy5 dye conjugated to the triple state quencher COT and benzylguanine for SNAP labeling. Ribosomes were labeled with the new dye, ICs were synthesized with the labeled subunits and these complexes were shown to be functional in bulk experiments (Supplementary Figure 1A). The new complexes were then flowed into chambers for single molecule visualization as described previously and were visualized after excitation with the 640 nm laser (Figure 5A). The fluorescence lifetimes observed for these complexes lasted much longer than previously seen with some molecules fluorescing throughout the entire visualization time (Figure 5B). To ensure that the lifetime would allow for observation of translation processes we wanted to characterize the lifetime of the fluorophore further. By measuring the fluorescence lifetimes of the labeled ICs at different excitation laser powers, we are able to show that the lifetime of the fluorophore decreases with increasing excitation power as expected (Supplementary Figure 1B). Using a low laser excitation power (2.5 mW) we were able to quantify the lifetime of the fluorophore on ICs bound to the coverslip surface (Figure 5C). The fluorophore lifetime of 0.598 min^{-1} will now allow us to observe the kinetics of ribosome rescue and recycling as predicted by bulk studies³⁸.

Labeling and testing of protein factors involved in termination, rescue, and release

With a functional assay for single molecule studies established we turned to labeling the protein factors important for termination, rescue and recycling. As introduced previously, the main factors involved in eukaryotic translation termination are eRF1 and eRF3. eRF1 recognizes the stop codon in the ribosomal A site. The GTPase activity of eRF3 promotes the structural rearrangement of eRF1 to allow it to catalyze the peptide hydrolysis reaction, releasing the polypeptide from the P site tRNA⁴⁰⁻⁴². These proteins are functionally homologous to the rescue factors DOM34 and HBS1 with these factors functioning to rescue ribosomes stalled on codons within the ORF^{37, 43, 44}. Ribosomes are then recycled by the protein factor RLI1 which splits the ribosomal subunits through the hydrolysis of ATP^{38, 45, 46} following either canonical termination or ribosome rescue. Therefore, we wanted to incorporate tags into these five proteins in order to allow us to specifically label them with different color fluorophores.

We incorporated a SNAP tag onto the C terminus of RLI1 to allow for fluorescent labeling and visualization (Supplementary Figure 2A). The recycling function of the labeled protein was then tested using the *in vitro* translation system described previously with an assay using peptidyl tRNA hydrolase (PTH). In this assay elongation complexes are formed by mixing initiation factors, 35S-Met-tRNA^{iMet} as above on a simple MF-Stop mRNA and then adding aminoacyl-tRNA, and elongation factors, eEF2, eEF3 and eIF5A to elongate prior to pelleting. The elongation complexes are then mixed with rescue factors, labeled or unlabeled RLI1 and PTH. Time points of the reaction are quenched using 10% formic acid. If RLI1 is functional, it will split the ribosomal subunits apart making released peptidyl tRNAs accessible by PTH for peptide hydrolysis and these peptide are resolved

by electrophoretic TLC (Figure 6A). Using this assay, the SNAP-labeled RL11 is as functional as a WT version without the SNAP tag (Figure 6B). The rate of release quantified from the TLCs for this assay, 0.83 min^{-1} is comparable to the release rates previously measured in bulk³⁸.

To label the termination factors and rescue factors for single molecule studies we used a different labeling strategy with the ybbR protein tag to reduce the size of the label. This method inserts a much smaller, 11 residue peptide tag (ybbR), onto the protein. An organic dye conjugated to CoA is then covalently attached to a serine residue in the ybbR tag using the SFP phosphopantetheinyl transferase⁴⁷. In collaboration with the Puglisi lab, we received labeled constructs for both eRF1 and eRF3. eRF1 and eRF3 constructs both with N terminal ybbR tags were successfully labeled with Cy3 and Cy5, respectively, with about 40% labeling efficiency (Supplementary Figure 3A, B).

Both proteins were then tested in a termination assay for activity. Because eRF1 catalyzes peptide hydrolysis from the P site tRNA this assay does not require the addition of the PTH enzyme. Instead, pelleted ICs (in this case on a simple MFD-Stop mRNA) are elongated through phenylalanine and aspartic acid using aa-tRNA, eEF1A ternary complex, eEF2, eEF3 and eIF5A. The elongated complexes are then mixed with the labeled or unlabeled termination factors of interest and time points of the reaction are taken quenching with 10% formic acid to run the peptides that were hydrolyzed by the termination factors on electrophoretic TLC (Figure 7A). As a negative control, the catalytically inactive mutant of eRF1 with its GGQ motif mutated to AGQ was also used in this assay⁴⁸. The fraction of MFD peptide released from ribosomes shows that the Cy3-

eRF1 and Cy5-eRF3 constructs are both similarly active in release as their WT counterparts and as compared to the catalytically dead eRF1-AGQ mutant (Figure 7B).

Additionally, labeled mutant constructs of both eRF1 and eRF3 were constructed to use as controls in single molecule experiments. The eRF1 N terminal ybbR construct was mutated at glycine 108 to alanine and labeled with Cy3 for a Cy3-eRF1 AGQ construct. Similarly, the eRF3 N terminal ybbR construct was mutated at histidine 348 to glutamic acid and labeled with Cy5 for a Cy5-eRF3 H348E construct. The eRF3 mutant is not catalytically dead as with the eRF1 AGQ mutant, but has been shown to be defective in termination⁴⁹. Both mutant proteins were tested for function using the previously described termination assay and showed decreased activity compared to their WT controls. The labeled eRF1 AGQ mutant is almost completely inactive and the H348E mutant of eRF3 shows a significantly slower release rate (Figure 7C).

The rescue factors, DOM34 and HBS1 were also tagged with ybbR for labeling at both the N and C terminal ends. Small scale labeling tests for both constructs of HBS1 yielded successfully labeled protein (Supplementary Figure 3C). The N terminal ybbR HBS1 construct was purified in large scale and labeled with Cy5 with a labeling efficiency of about 22%. Although this labeling efficiency is lower, single molecule experiments will allow only the analysis of labeled factors making experiments feasible. Labeling of both the N and C terminal ybbR constructs of DOM34 is currently being optimized before large scale preparations of this protein can be performed. Once these conditions are optimized both proteins will be tested for activity using the PTH assay outlined above before use in single molecule experiments.

Discussion

With the feasibility of this single molecule assay established and many of the protein factors involved in translation termination, rescue and ribosome recycling fluorescently labeled, it can be used to answer many open questions regarding the various kinetic steps in these processes. These experiments are more feasible on the advanced imaging systems developed by the Puglisi lab. Their use of ZMW fluorescence microscopy in combination with the four-color detection power of an in-house Pacific Biosciences's RS sequencer allows for the simultaneous collection of larger amounts of data⁵⁰. This will be especially useful and more efficient than collecting data for one slide at a time as is done on a more traditional TIRF setup. Initial experiments using the RS system have begun in the Puglisi lab and will allow many of the complex questions discussed below to be addressed.

Although it is suggested from structural and bulk biochemical studies that eRF1 and eRF3 associate with ribosomes as a complex^{51, 52}, it has never been demonstrated directly during association. Single molecule experiments following fluorescently labeled constructs of both of these factors will allow direct observation of their association either individually or as a complex. These experiments are already underway in the Puglisi lab and will also allow for the measurement of the rates of association for these two factors during termination. From structural studies, it is also suggested that the binding of eRF3 and RL11 to the ribosome are mutually exclusive events as they share a binding site⁴⁶. The dissociation of eRF3 and the binding of RL11 can be measured directly using this assay to

confirm this hypothesis. Furthermore, the effect of RLI1 binding on the dissociation of eRF3 can be measured.

The mechanism of peptide release and subunit separation can also be explored further using a single molecule assay with the development of a few more features. Using peptide binding antibodies fused to fluorescent proteins, peptide release could be monitored at the single molecule level. While this will require elongation of much longer peptides than shown here using *in vitro* bulk studies, this experiment will allow further understanding of the role of RLI1 in the enhancement of peptide release by eRF1. Similarly, if ribosome labels on the small and large subunit that report on the functional state of the ribosome using FRET are developed, as they have been in *E. coli*^{20, 21, 53}, the mechanism of RLI1 splitting through eRF1 could be investigated further. Previous studies suggest that RLI1 uses the force of ATP hydrolysis to push eRF1 into the intersubunit space of the ribosome to separate the subunits⁵⁴. Use of a FRET pair on eRF1 and RLI1 simultaneously with a FRET pair that reports on the state of the ribosome could give further insight into the mechanistic details of this process.

Given the homology of the canonical termination and recycling process with eRF1, eRF3, and RLI1, there are many open questions analogous to these regarding the process of ribosome rescue and recycling by DOM34, HBS1, and RLI1. Do DOM34 and HBS1 bind as a complex or individually in a sequential manner? Is the binding of RLI1 precluded by HBS1 and does the presence of RLI1 enhance the dissociation of HBS1 from the ribosome? Does the GTP hydrolysis of HBS1 lead to conformational changes to DOM34? How does RLI1 interact with DOM34 to split the ribosomal subunits? Is the association rate of RLI1 rescue substrates targeted by DOM34 similar to the association rate for

terminating ribosomes bound by eRF1 or does peptidyl tRNA in the P site of the ribosome slow RLI1 binding in the case of rescue? Does RLI1 make similar conformational changes when associated with eRF1 bound and DOM34 bound ribosomes? All of these questions can begin to be addressed using the *in vitro* single molecule assay developed in this study. This will allow significant clarification of many of the kinetic steps carried out during the processes of termination, rescue and recycling that are crucial for cellular function and viability.

Figures

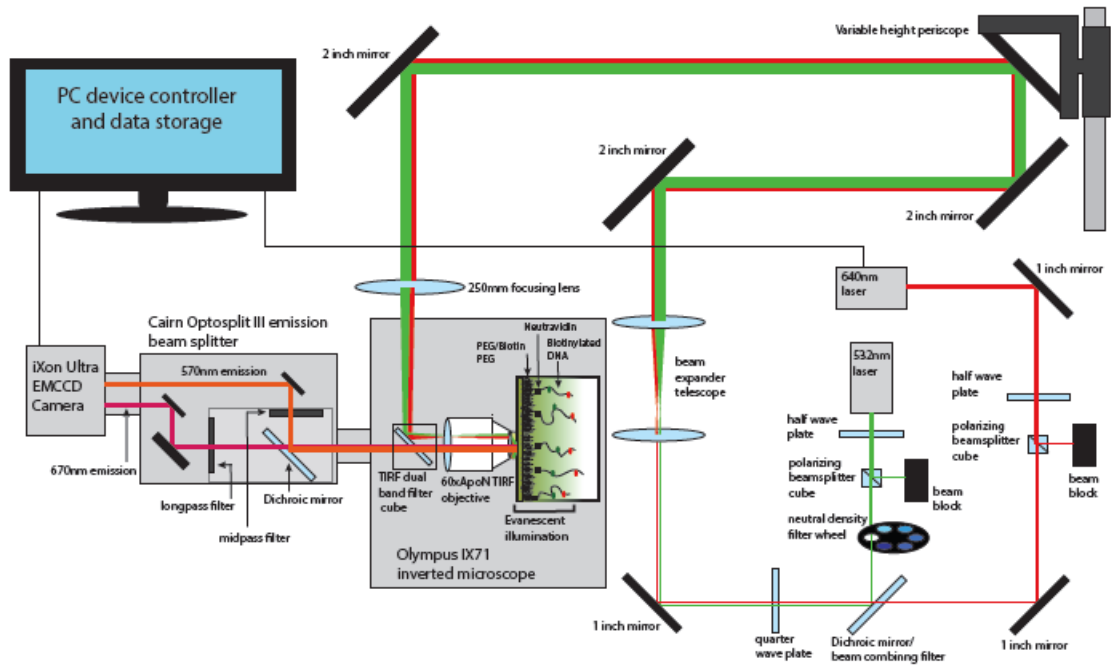
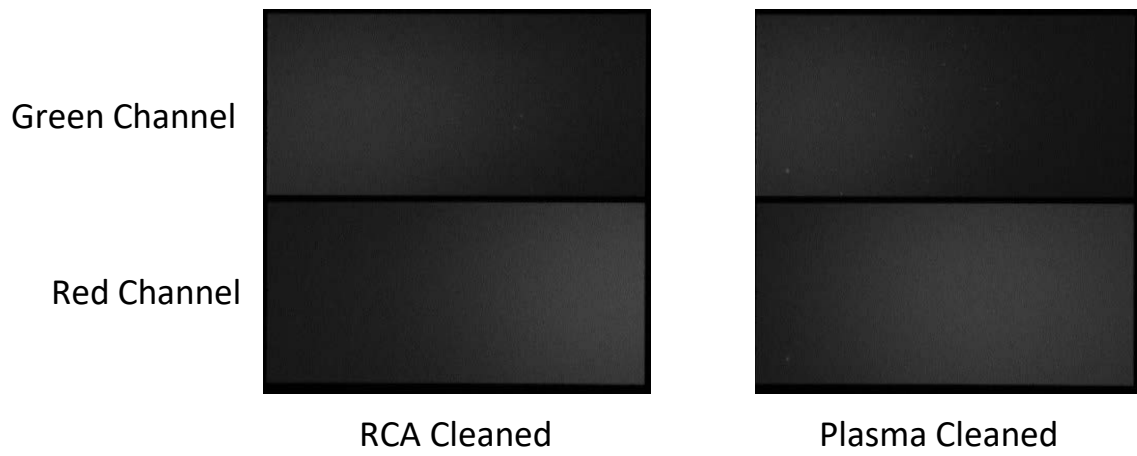
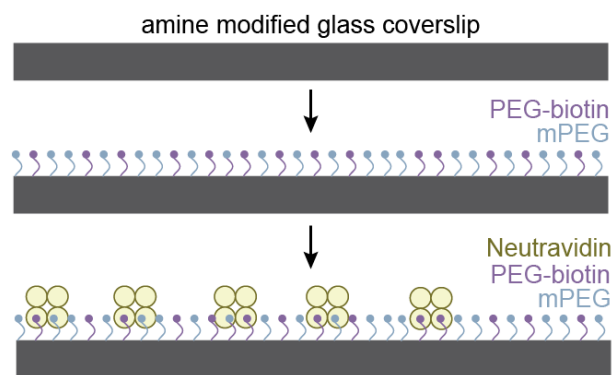


Figure 1

A



B



C

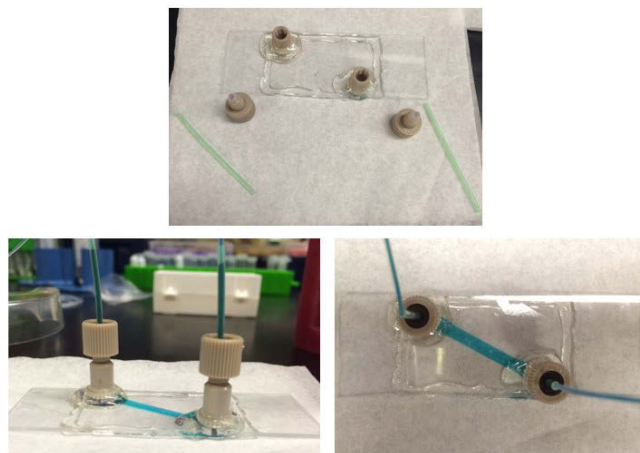
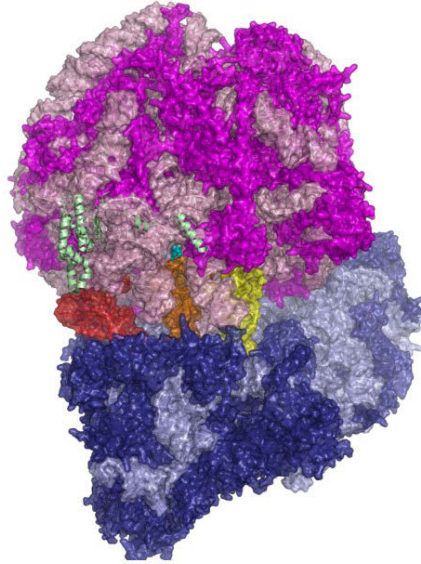
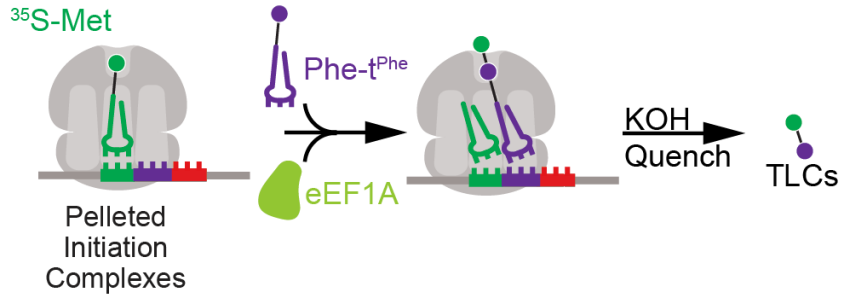
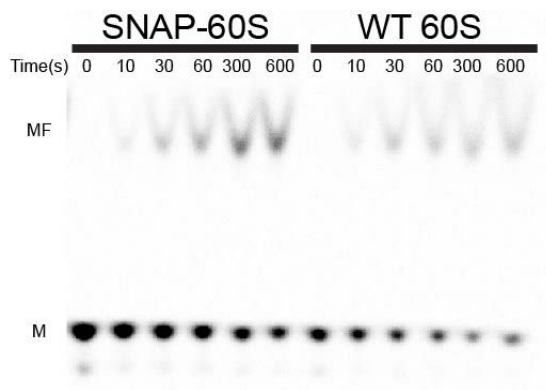
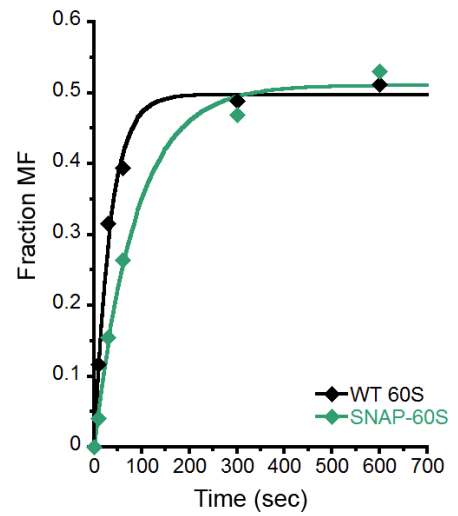
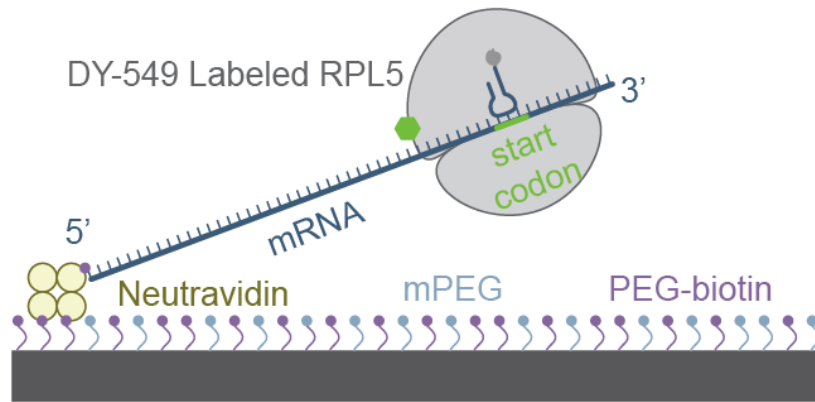


Figure 2

A**B****C****D****Figure 3**

A



B

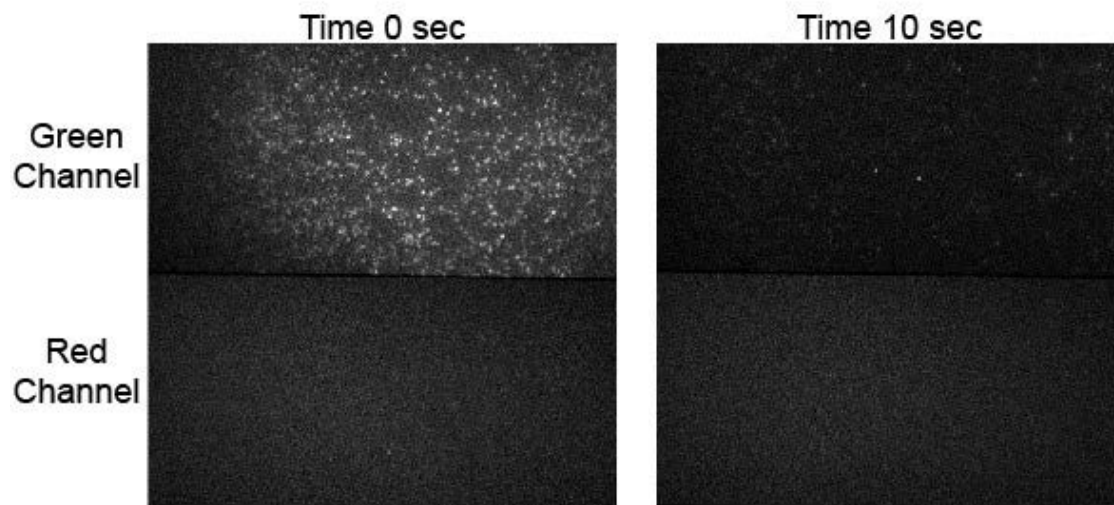
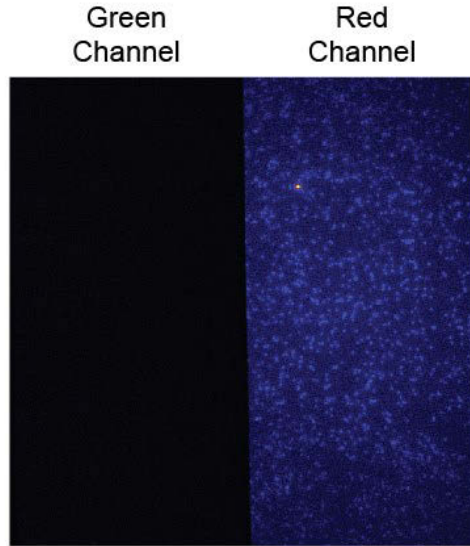
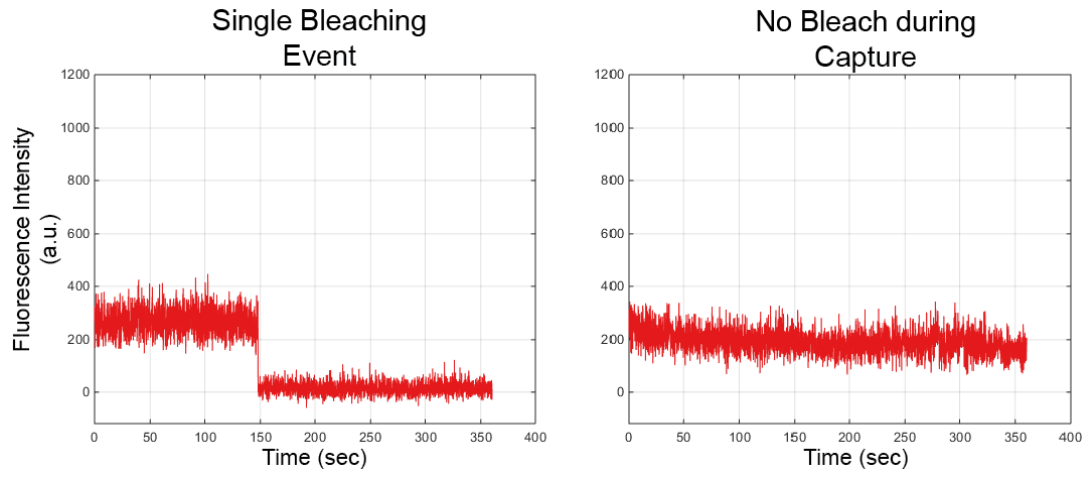


Figure 4

A



B



C

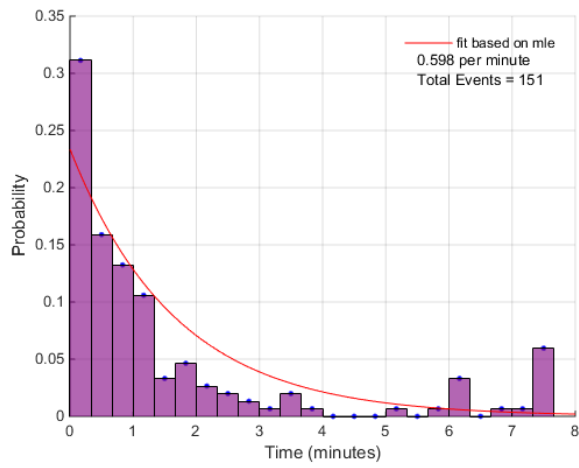
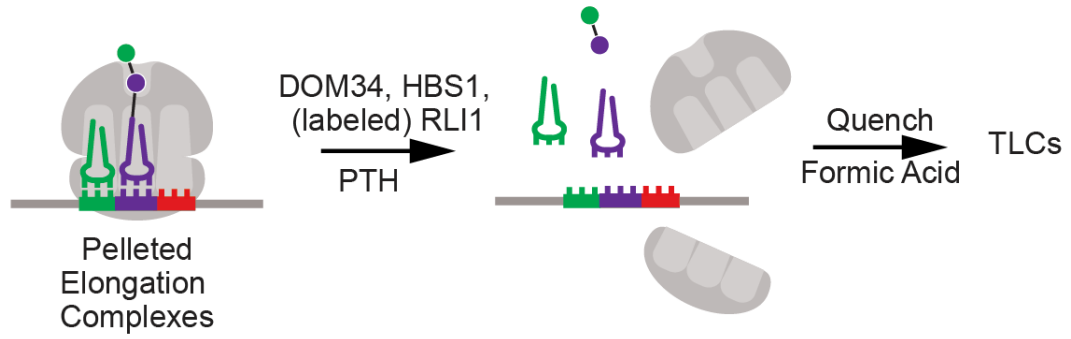


Figure 5

A



B

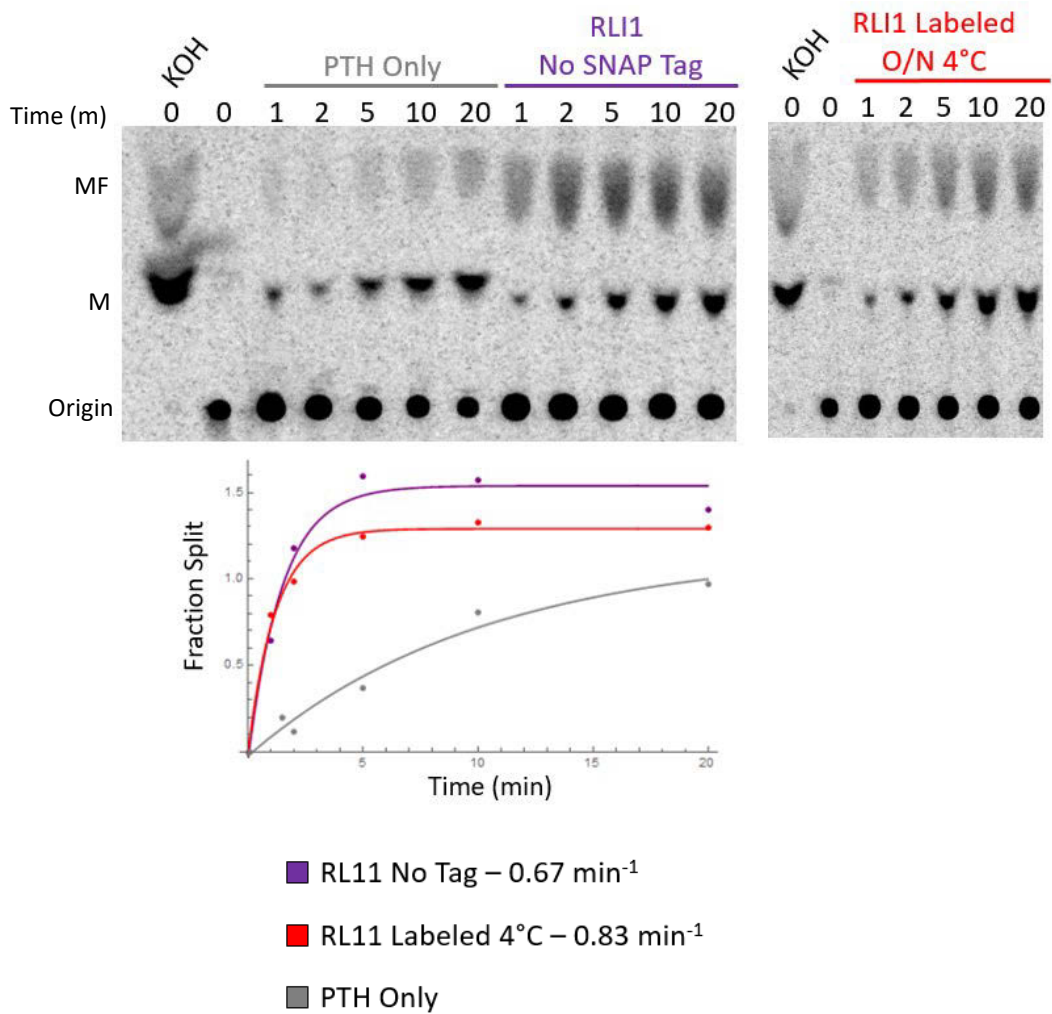
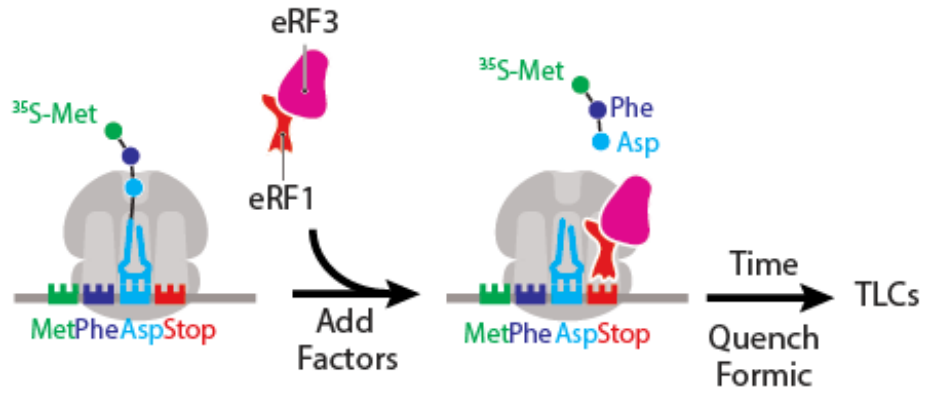
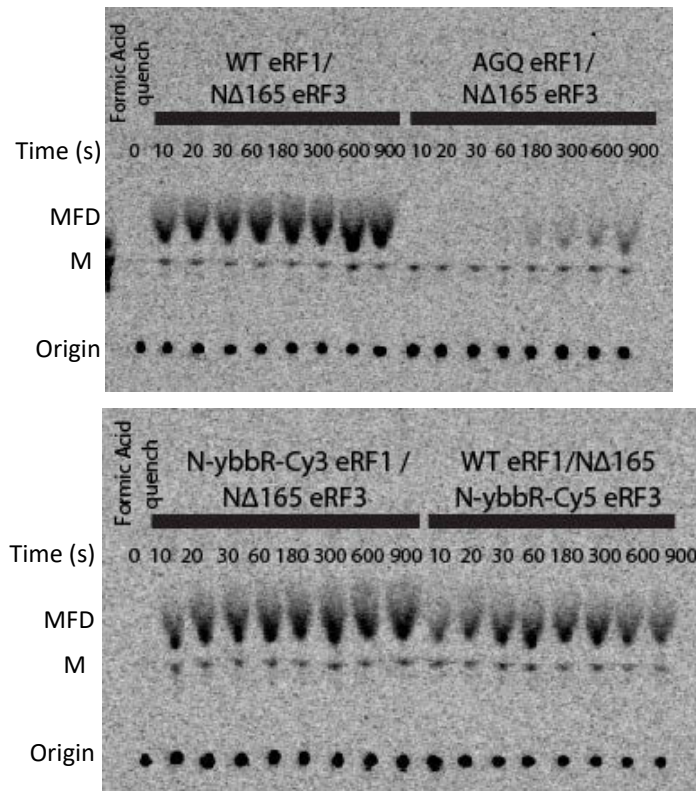


Figure 6

A



B



C

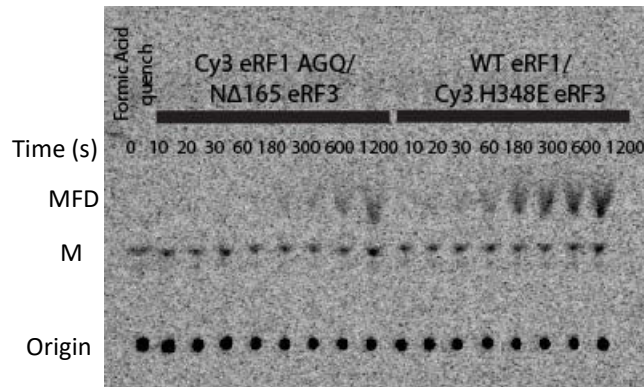
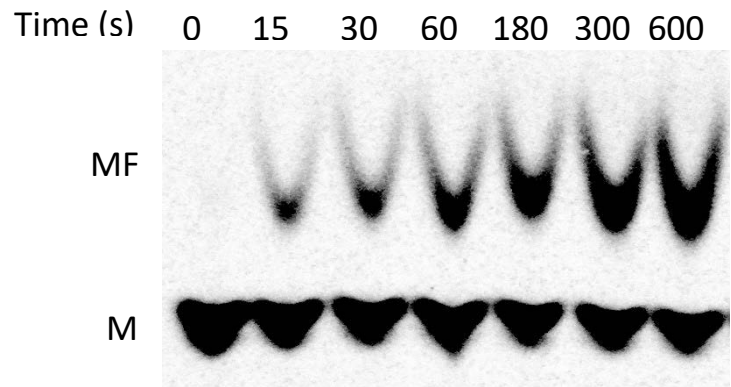
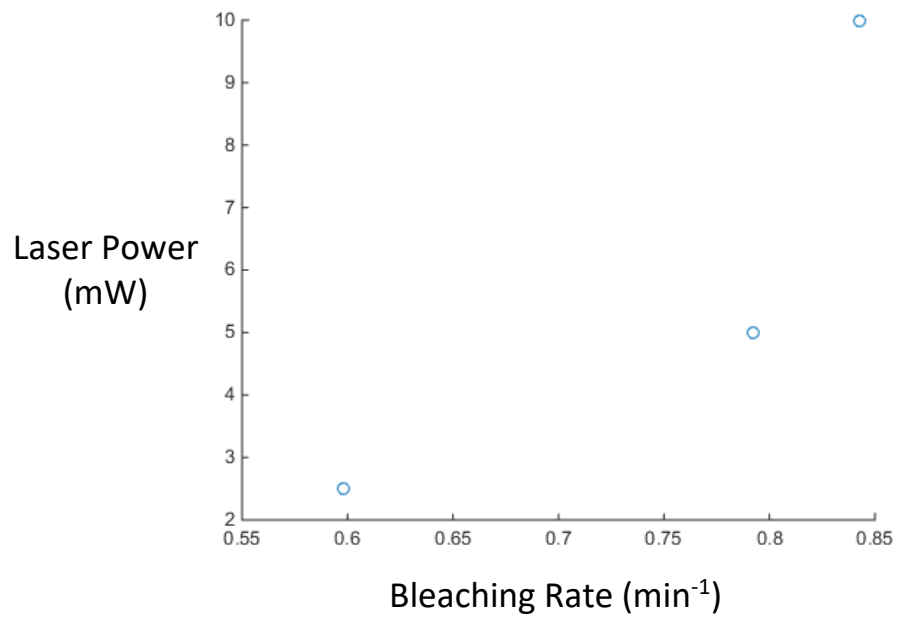


Figure 7

A

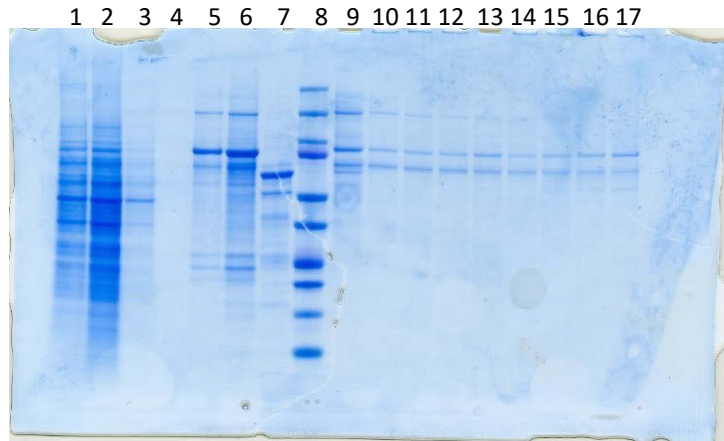


B



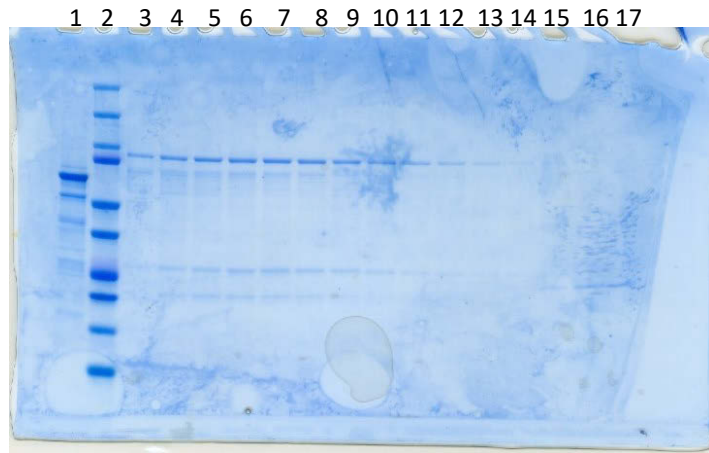
Supplementary Figure 1

A



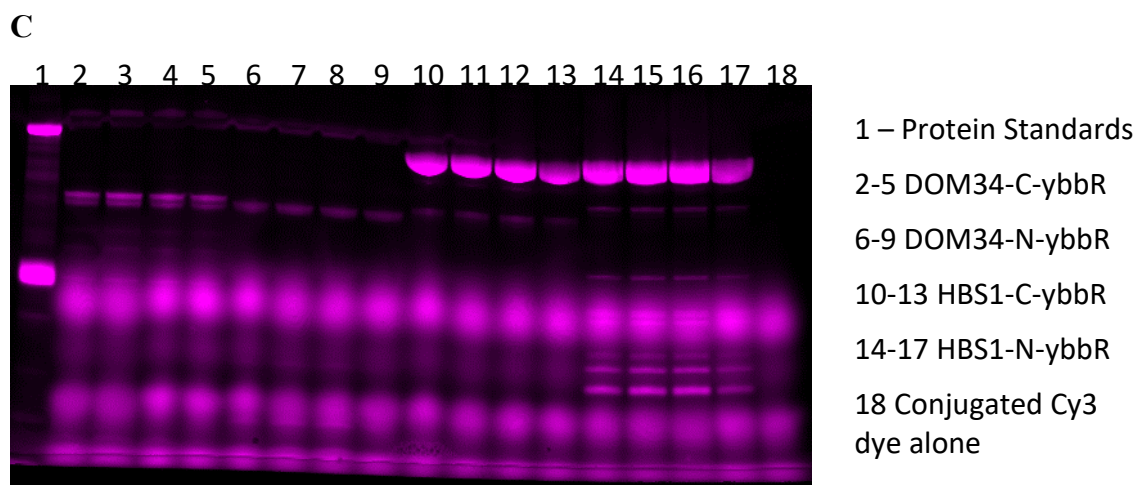
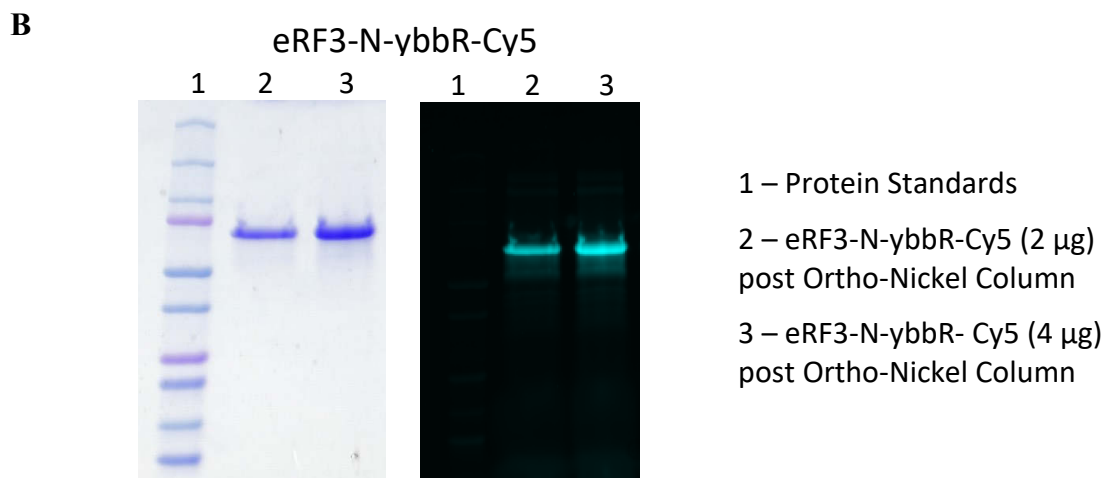
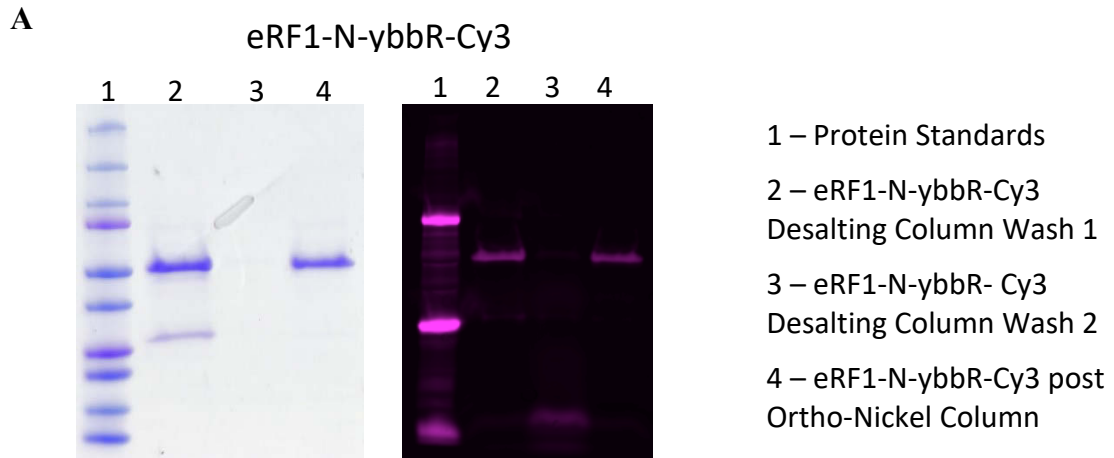
- 1 – Lysate
- 2 – Nickel Column FT
- 3 – Nickel Column Wash 1
- 4 – Nickel Column Wash 2
- 5 – Nickel Column Elute
- 6 – S200 Load
- 7 – RLI1 control no SNAP tag
- 8 – Protein Standards
- 9 – 17 S200 Fractions

B



- 1 – RLI1 control no SNAP tag
- 2 – Protein Standards
- 3 – 17 S200 Fractions

Supplementary Figure 2



Supplementary Figure 3

Figure Legends

Figure 1. Construction of single molecule TIRF microscope. Schematic representing the smTIRF microscope built in the laboratory of James Berger highlighting the optical components necessary for visualization. The excitation pathway is shown on the right of the diagram with the 532 nm and 640 nm lasers depicted as green and red lines, respectively. The emission pathway is shown on the left of the diagram with the emissions from the 532 nm (green) laser and 640 nm (red) laser depicted as orange and magenta, respectively. (Schematic modified from Timothy Wendorff – unpublished)

Figure 2. Steps of sample chamber preparation. (A) Images of coverslips following cleaning to remove fluorescence impurities from the glass surface. The image on the left shows a coverslip cleaned using the RCA cleaning method while the image on the right shows a coverslip cleaned using a plasma cleaner. **(B)** Schematic representation of the surface passivation to enable molecules to be bound to the coverslip surface for TIR visualization. **(C)** Images of sample chambers constructed using NanoPorts to allow the efficient delivery of sample material to the coverslip surface. Food coloring was flowed through the sample chamber to allow for ease of visualization of the setup.

Figure 3. Ribosome labeling and function tests. (A) Crystal structure of the yeast 80S ribosome modeled with tRNAs in the E, P and A sites (shown in red, orange and yellow, respectively). The proteins of the 40S subunit are colored in dark blue, while the RNA of the 40S subunit is colored in light blue and the proteins of the 60S subunit are colored in dark magenta, while the RNA of the 60S subunit is colored in light magenta. The recycling factor RL11 is rendered as a cartoon and shown in light green with the insertion site for the SNAP tag label highlighted by cyan spheres. (B) Schematic representation of the elongation assay using on eEF1A to follow the incorporation of phenylalanine to ICs. (C) Representative TLCs and their corresponding elongation kinetics testing the functionality of WT yeast ribosomes as compared to 60S-SNAP labeled yeast ribosomes.

Figure 4. Single molecule visualization of initiation complexes with labeled ribosomes.

(A) Schematic representation of the single molecule experiment showing 5' biotinylated mRNA ICs bound to the functionalized surface of the coverslip. (B) Example TIR image of DY-549 labeled ribosome complexes bound to the surface of the coverslip excited by the 532 nm laser. **Left:** Visualization at time zero. **Right:** Visualization after continuous laser excitation for 10 seconds, highlighting the rapid photobleaching of the fluorescent ribosomal complexes.

Figure 5. Characterization of a Cy5-M labeled ribosomes by single molecule visualization. (A) Representative image of single molecule visualization of ICs synthesized with ribosomes labeled with Cy5-M – a longer lived fluorophore. The emission channel for the 532 nm (green) excitation laser is shown on the left and the emission channel for the 640 nm (red) excitation laser is shown on the right. The image was captured using on the 640 nm (red) excitation laser. (B) Representative traces of individually tracked IC molecules. **Left:** Trace showing a single photobleaching event around 150 seconds of continuous excitation by the 640 nm (red) excitation laser. **Right:** Trace showing an individual molecule fluorescing for the length of the capture, around 360 seconds, with continuous excitation by the 640 nm (red) excitation laser. (C) Histogram of fluorescence lifetimes of individually traced molecules. Individual traces were manually examined and a single photobleaching even was selected to quantify the lifetimes of the individual molecules. All 151 molecules represented in the histogram were collected under 2.5 mW 640 nm (red) laser excitation. A maximum likelihood estimation was used to quantify the overall lifetime of the fluorophore at these conditions yielding a photobleaching rate of about 0.6 min^{-1} .

Figure 6. Testing of labeled RLI1 for ribosome recycling activity. (A) Schematic representation of the PTH assay performed *in vitro* to test the functionality of labeled RLI1. Pelleted elongation complexes are mixed with the rescue factors, DOM34 and HBS1, as well as the labeled or unlabeled recycling factor RLI1 and the enzyme PTH. As ribosomes are split, PTH cleaves the peptidyl tRNA releasing the peptide which is quenched with formic acid and run on electrophoretic TLC. (B) TLC and quantification of splitting kinetics by RLI1. The TLC on the left shows the PTH alone control and the activity of the untagged, unlabeled RLI1 construct. The TLC on the right shows the activity of the C terminally SNAP tagged version of RLI1 labeled with a Cy3 conjugated dye. The KOH quench lanes are controls to show that the ICs used in the experiment are elongating as expected.

Figure 7. Testing of labeled eRF1 and eRF3 for canonical termination by peptide release. (A) Schematic representation of the *in vitro* termination assay used to test labeled and unlabeled constructs of eRF1 and eRF3. Pelleted initiation complexes are elongated to their stop codons and then mixed with either labeled or unlabeled termination factors. Time points were quenched with formic acid to assess the amount of peptide released by electrophoretic TLC. (B) TLCs of peptide release assay on a variety of labeled or unlabeled termination factors. The top TLC shows the activity of both WT eRF1 and eRF3 compared to the catalytically dead mutant eRF1 AGQ which shows little to no activity. The bottom TLC shows the peptide release activity of labeled eRF1-N-ybbR with WT eRF3 and labeled eRF3-N-ybbR with WT eRF1. (C) TLCs of peptide releases assay for the labeled mutant termination factors – eRF1-AGQ-N-ybbR-Cy3 with WT eRF3 and eRF3-H348E-N-ybbR-Cy3 with WT eRF1.

Supplementary Figure 1. Function of Cy5-M complexes *in vitro* and further characterization of their lifetimes. (A) TLC showing the peptide transfer activity of ICs made with the Cy5-M labeled ribosomes according to the assay shown in Figure 3B. Time points were quenched with KOH and run on electrophoretic TLC. (B) Cy5-M complex lifetimes quantified at various laser powers showing that lifetime decreases with increasing excitation laser power. Individual lifetimes for each laser power were calculated using a maximum likelihood estimation from a histogram of individually quantified photobleaching events as in Figure 5C.

Supplementary Figure 2. Purification of RLI1-SNAP construct. (A) Coomassie stained protein gel showing fractions from Nickel column purification and the beginning of sizing column purification. (B) Coomassie stained protein gel showing the remaining fractions from sizing column purification. Tagged RLI1 from lanes 4-9 were pooled and concentrated for fluorescent labeling. Purified, untagged RLI1 was run on both gels (S1A lane 7 and S1B lane 1) as a control and runs about 20 kDa smaller as expected for the protein lacking the SNAP tag.

Supplementary Figure 3. Purification of labeled termination and rescue factors. (A)

Left: Coomassie stained protein gel showing purified and labeled eRF1-N-ybbR-Cy3 following desalting column purification to remove free dye and a final ortho-nickel column clean up. **Right:** Protein gel scanned for Cy3 fluorescence using a Typhoon imager of the same eRF1-N-ybbR-Cy3 samples as on the coomassie stained gel to assess the efficiency of protein labeling. **(B) Left:** Coomassie stained protein gel showing purified eRF3-N-ybbR-Cy5 following the final ortho-nickel column purification. **Right:** Protein gel scanned for Cy5 fluorescence using a Typhoon imager of the same eRF3-N-ybbR-Cy5 samples as on the coomassie stained gel to assess the efficiency of protein labeling. Two concentrations of protein were run on both gels for better quantification. **(C)** Protein gel showing small scale labeling test of DOM34-C-ybbR, DOM34-N-ybbR, HBS1-C-ybbR and HBS1-N-ybbR constructs (from left to right) with Cy3 conjugated dye. Four labeling conditions were tested for each construct: room temperature labeling for 30 minutes, 30°C labeling for 30 minutes, 37°C labeling for 30 minutes, and 4°C labeling for 2 hours. Both HBS1 constructs show efficient labeling (lanes 10-17) with some protein degradation for the HBS1-N-ybbR construct as shown by the fluorescent laddering between the top protein band corresponding to full length HBS1 (lanes 14-17). Neither DOM34 construct showed efficient labeling (lanes 2-9). Conjugated Cy3 dye alone was also run as a comparative control (lane 18).

Methods

Purification and labeling of ribosomal subunits

Yeast strain AL63 (parental strain is JWY3733 - MAT α ura3-52 trp1 Δ 101 leu2 Δ 1 ade1 his3 Δ 200 rp11::TRP1 + pRS315-rp15-SNAP) from the Puglisi lab was grown, lysed and pelleted over a sucrose cushion as described previously⁵⁵. Pellets were resuspended in the cold room in 1 mL (each) of subunit separation buffer (50 mM HEPES-KOH pH 7.4, 2 mM MgCl₂, 500 mM KCl, 2 mM DTT) with or without 10 μ M dye. Subunits were then separated by treatment with 1mM puromycin and allowed to label at 37°C for 30 minutes. A260 measurements were taken and 200 A260 units of ribosome were layered onto 5-20% sucrose gradients. Gradients were spun in a Beckman SW28 rotor at 24,000 rpm for 10 hours. Separated 40S and labeled or unlabeled 60S subunits were collected via an in-line UV detector. Subunits were pooled, concentrated and buffer exchanged into ribosome storage buffer (20 mM HEPES-KOH, pH 7.4, 2.5 mM magnesium acetate, 100 mM KOAc, 250 mM sucrose and 2 mM DTT). A260 measurements were taken to approximate concentration along with UV/Vis measurements of labeled subunits to approximate the extent of labeling. Aliquots of subunits were stored at -80°C until use.

Purification of translation factors

Translation initiation factors eIF1, eIF1A, eIF5, eIF5B were expressed and purified from *E. coli* and eIF2 was expressed and purified from *S. cerevisiae* as previously described^{55, 56}. The translation elongation factor, eIF5A was purified from *E. coli* as previously

pelleting, ribosomes were resuspended in 15-25 μL of 1X Buffer E containing 10 mM $\text{Mg}(\text{OAc})_2$ and stored at -80°C .

To form elongation complexes, initiation complexes were formed as above and elongated before pelleting as described previously⁵⁸.

***In vitro* reconstituted peptide transfer assay**

Translation elongation reactions were performed as previously described^{55, 58} with minor differences. Briefly, aa-tRNA ternary complex was formed by incubating aa-tRNA (1.5 μM), eEF1A (5 μM), 1 mM GTP, in 1X Buffer E for 10 minutes at 26°C . Limited amounts of 80S initiation complexes (3 nM) were then mixed with aa-tRNA ternary complex (150 nM). Reactions were incubated at 26°C and time points quenched into 500mM KOH. Samples were spotted (1 μL) to monitor peptide transfer by electrophoretic TLC (Millipore). TLC plates were equilibrated with pyridine acetate buffer (5 mL pyridine, 200 mL acetic acid in 1 l, pH 2.8) before electrophoresis at 1400 V for 20 min. Plates were developed using a Typhoon FLA 9500 Phosphorimager system (GE Healthcare Life Sciences) and quantified using ImageQuantTL (GE Healthcare Life Sciences). Time courses were fit to single exponential kinetics using Kaleidagraph (Synergy Software).

***In vitro* PTH assay to access ribosome recycling**

Reactions were performed as described previously^{37, 55}. Briefly: limiting amount of translation elongation complexes (3 nM) were mixed with rescue factors DOM34 (4 μM), HBS1 (4 μM), and labeled or unlabeled RLI1 (4 μM) in 1X Buffer E. An excess amount of peptidyl-tRNA hydrolase (PTH) (50uM) was added to monitor tRNA release from the

ribosome following recycling. Time points for recycled products were quenched with 10% formic acid and were analyzed by electrophoretic TLC in pyridine acetate buffer (see above) at 1400 V for 20 minutes.

***In vitro* peptide release assay**

Peptide release assays were performed as previously described⁵⁸ with slight variation. Initiation complexes were elongated using ternary complex (eEF1A, aa-tRNAs, GTP), eEF2, eEF3, and eIF5A for 5 minutes. Elongated complexes were then combined with pre-mixed combinations of labeled and unlabeled termination factors at a concentration of 6 μ M in 1X Buffer E. Time points were quenched with 10% formic acid and run on electrophoretic TLC plates pre-equilibrated in pyridine acetate buffer (see above). TLCs were run at 1200V for 25 minutes, dried, developed and quantified for release products.

Purification and labeling of RLI1

C-terminal His₆ RLI1 was cloned to include a SNAP tag following His₆ and was grown and purified as previously described³⁸ over Nickel and sizing (S200) columns. Labeling reactions were set up as follows: protein in Buffer SE (20 mM Tris-Cl, pH 7.5, 200 mM NaCl, 5mM β ME, and 5% glycerol) was mixed with 2X excess of SNAP-Alexa549 (NEB), and 1 mM β ME. Reactions were allowed to incubate at 4°C overnight. Labeled protein was then run over NAP 5 column (GE Healthcare) to remove excess dye. A280 and A555 measurements were taken to calculate concentration and labeling efficiency, respectively. Small aliquots of labeled protein were stored at -80°C until use.

Purification and labeling of eRF1 and eRF3

eRF1 and eRF3 (NΔ165) N terminal His₆-MBP constructs were cloned to insert N terminal ybbR tags downstream of the TEV cleavage site and subsequently purified and labeled in the Puglisi lab. The general method of purification is as follows: Ni-NTA purification, TEV cleavage, ortho-Nickel, sizing column, dialysis into labeling buffer, labeling, 10DG desalting column, and ortho-Nickel. Purified proteins were run on coomassie gels and scanned at the appropriate wavelengths to quantify labeling efficiency.

Purification and labeling of DOM34 and HBS1

DOM34 and HBS1 were cloned using Gibson assembly into MacroLab 1C vector (N terminal His₆-MBP) and the ybbR tag was inserted at the N terminus just downstream of the TEV cleavage site or at the C terminus followed by a GGGGKL amino acid linker (DOM34-C-ybbR LN72, DOM34-N-ybbR LN73, HBS1-C-ybbR LN74, and HBS1-N-ybbR LN75). Proteins were purified similarly to previously published protocols³⁷ over Nickel columns (GE Healthcare). Proteins were then TEV cleaved overnight to remove the His₆-MBP tag and run over ortho-Nickel. Proteins were then dialyzed into SFP labeling buffer (50 mM HEPES-KOH, pH 7.5, 100 mM NaCl, 10mM MgCl₂, and 5mM DTT). A lot of DOM34 protein crashed out during this step dialyzing into low salt buffer. Labeling reactions were set up as follows 2 μM SFP synthetase, 20 μM CoA-Cy3, and 15 μM protein in labeling buffer. Reactions were allowed to incubate at room temperature, 30°C, and 37°C for 30 minutes, or 4°C for 2 hours. Labeled protein was then run gel to assess labeling efficiency.

Subsequent purifications of DOM34 will include higher salt concentrations throughout purification before dropping salt concentrations for labeling. Unlabeled, tagged HBS1 constructs were sent to the Puglisi lab for large scale purifications as described above for eRF1 and eRF3 given the efficient labeling seen (Supplementary Figure 3C). SFP synthetase was gifted from the Puglisi lab and purified according to a previously published protocol⁴⁷. CoA-Cy3 was gifted from the Puglisi lab following synthesis.

RCA coverslip and slide cleaning

Slides and coverslips were placed in ceramic holders in a beaker and covered in a mixture of 400 mL H₂O, 80 mL Ammonium hydroxide (28%) which was heated and stirred until it starts to bubble. 80 mL 30% hydrogen peroxide was then added and the beaker was covered with foil. Slides and coverslips were cleaned for 1 hour. The beaker was then cooled and the mixture discarded to waste. Slides and coverslips were then washed multiple times with milli-Q water and transferred to methanol until surface passivation.

Plasma cleaning of coverslips and slides

Slides and coverslips were placed in ceramic holders inside the plasma cleaner (Harrick Plasma). The vacuum pump is turned on and the pressure of the chamber is allowed to fall below 200 mTorr. The plasma power is set to high and turned on. A small amount of air is bled in about every minute for 5 minutes to allow the slides and coverslips to be cleaned. The slides and coverslips are removed from the chamber and immediately immersed in methanol until surface passivation.

Coverslip and slide surface passivation

Coverslips and slides were passivated according to a previously published protocol²⁸. Briefly, slides and coverslips were silanized in a mixture of 400 mL methanol, 20 mL glacial Acetic Acid, 4 mL amino-silane with stirring for 20 minutes. Coverslips and slides are then placed back in methanol briefly. Coverslips and slides are then individually removed from methanol, washed with milli-W water and dried with N₂ gas. Clean, dried coverslips and slides are then placed in tip boxes filled partially with water so the solutions added to functionalize them do not dry out. A mixture of m-PEG and biotin-PEG (Laysan Bio) is prepared in 100 mM sodium bicarbonate as described²⁸. Solutions containing varying ratios of m-PEG and biotin-PEG can be used to vary the amount of biotin on the surface. For all slides a solution of only mPEG was used. 35 μ L of m-PEG/biotin-PEG mixtures was sandwiched between coverslips and 70 μ L of m-PEG only solution was sandwiched between slides. Slides and coverslips were incubated in humid chamber overnight. Sandwiches were then separated, rinsed with milli-Q water and dried with N₂ gas. One slide and coverslip were then placed in a 50 mL conical with holes in the lid and vacuum sealed in a bag for storage at -20°C until chamber assembly for imaging.

Sample chamber assembly

Slides and coverslips were removed from -20°C and allowed to come to room temperature. Double stick tape was placed on the functionalized surface of the glass slide on either side of the drilled holes to create a channel. The functionalized surface of the coverslip was then sandwiched face down onto the slide so the surface of the slide and

coverslip in the channel are both functionalized. The edges of the coverslip were then epoxied to prevent leaking. NanoPort assemblies were epoxied to the non-functionalized surface of the glass slide and tubing was inserted along with a needle and small syringe for sample delivery.

Single molecule TIRF imaging of ICs

Assembled sample chambers were washed and equilibrated in reaction Buffer E (see above) and imaged to assess background of surface. A solution of 200 nM neutravidin was mixed in Buffer E and combined with labeled 80S initiation complexes for a ratio of 4:1 neutravidin to IC. This mixture was incubated on ice for 2 minutes and then diluted in Buffer E with oxygen scavenging system (PCA and PCD) for a final labeled complex concentration of about 300 pM. This solution was then flowed over the surface of the slide and incubated for 3 minutes before washing with Buffer E containing oxygen scavengers and imaging. Imaging was done with continuous laser excitation with one or both lasers and recorded using Single software (Ha lab).

Analysis of single molecule traces to calculate fluorophore lifetime

Raw data files were then converted to trace files in IDL using scripts from the Ha lab. Trace files were then graphed in MATLAB and visually inspected to select only traces with a single photobleaching event. The lifetime (time at which the molecule bleached) was selected manually and all time were compiled. Lifetimes were then plotted as a histogram for a given laser power and fit using a maximum likelihood estimation model to

quantify the overall lifetime of the fluorophore when imaged as part of a ribosomal initiation complex bound to a coverslip surface.

References

1. Petrov, A., Chen, J., O'Leary, S., Tsai, A. & Puglisi, J.D. Single-molecule analysis of translational dynamics. *Cold Spring Harbor perspectives in biology* **4** (2012).
2. Prabhakar, A., Puglisi, E.V. & Puglisi, J.D. Single-Molecule Fluorescence Applied to Translation. *Cold Spring Harbor perspectives in biology* **11** (2019).
3. Ha, T. Single-molecule methods leap ahead. *Nature methods* **11**, 1015-1018 (2014).
4. Ha, T. & Tinnefeld, P. Photophysics of Fluorescent Probes for Single-Molecule Biophysics and Super-Resolution Imaging. *Physical Chemistry* **63**, 595-617 (2012).
5. Zheng, Q. *et al.* Ultra-stable organic fluorophores for single-molecule research. *Chemical Society reviews* **43**, 1044-1056 (2014).
6. Grimm, J.B. *et al.* A general method to improve fluorophores for live-cell and single-molecule microscopy. *Nature methods* **12**, 244-250 (2015).
7. Ha, T. Single-molecule fluorescence resonance energy transfer. *Methods (San Diego, Calif.)* **25**, 78-86 (2001).
8. Levene, M.J. *et al.* Zero-mode waveguides for single-molecule analysis at high concentrations. *Science (New York, N.Y.)* **299**, 682-686 (2003).
9. Zhu, P. & Craighead, H.G. Zero-mode waveguides for single-molecule analysis. *Annual review of biophysics* **41**, 269-293 (2012).
10. Friedman, L.J., Chung, J. & Gelles, J. Viewing dynamic assembly of molecular complexes by multi-wavelength single-molecule fluorescence. *Biophysical journal* **91**, 1023-1031 (2006).
11. Friedman, L.J. & Gelles, J. Multi-wavelength single-molecule fluorescence analysis of transcription mechanisms. *Methods (San Diego, Calif.)* **86**, 27-36 (2015).
12. Joo, C. & Ha, T. Single-molecule FRET with total internal reflection microscopy. *Cold Spring Harbor protocols* **2012** (2012).
13. Selvin, P.R. The renaissance of fluorescence resonance energy transfer. *Nature structural biology* **7**, 730-734 (2000).
14. Roy, R., Hohng, S. & Ha, T. A practical guide to single-molecule FRET. *Nature Methods* **5**, 507-516 (2008).
15. Blanchard, S.C., Kim, H.D., Gonzalez, R.L., Puglisi, J.D. & Chu, S. tRNA dynamics on the ribosome during translation. *Proceedings of the National Academy of Sciences of the United States of America* **101**, 12893-12898 (2004).
16. Morisaki, T. *et al.* Real-time quantification of single RNA translation dynamics in living cells. *Science (New York, N.Y.)* **352**, 1425-1429 (2016).
17. Wu, B., Eliscovich, C., Yoon, Y.J. & Singer, R.H. Translation dynamics of single mRNAs in live cells and neurons. *Science (New York, N.Y.)* **352**, 1430-1435 (2016).
18. MacDougall, D.D. & Gonzalez, R.L. Translation initiation factor 3 regulates switching between different modes of ribosomal subunit joining. *Journal of molecular biology* **427**, 1801-1818 (2015).
19. Fuchs, G. *et al.* Kinetic pathway of 40S ribosomal subunit recruitment to hepatitis C virus internal ribosome entry site. *Proceedings of the National Academy of Sciences of the United States of America* **112**, 319-325 (2015).
20. Chen, J. *et al.* Dynamic pathways of -1 translational frameshifting. *Nature* **512** (2014).
21. Hickerson, R., Majumdar, Z.K., Baucom, A., Clegg, R.M. & Noller, H.F. Measurement of internal movements within the 30 S ribosomal subunit using Förster resonance energy transfer. *Journal of molecular biology* **354**, 459-472 (2005).
22. Fei, J., Kosuri, P., MacDougall, D.D. & Gonzalez, R.L. Coupling of ribosomal L1 stalk and tRNA dynamics during translation elongation. *Molecular cell* **30**, 348-359 (2008).
23. Schuller, A.P. & Green, R. Roadblocks and resolutions in eukaryotic translation. *Nature reviews. Molecular cell biology* **19**, 526-541 (2018).
24. Dever, T.E. & Green, R. The Elongation, Termination, and Recycling Phases of Translation in Eukaryotes. *Cold Spring Harbor Perspectives in Biology* **4** (2012).
25. Joo, C. & Ha, T. Objective-Type Total Internal Reflection Microscopy (Excitation) for Single-Molecule FRET. *Cold Spring Harbor Protocols* **2012** (2012).

26. Toomre, D. Alignment and Calibration of Total Internal Reflection Fluorescence Microscopy Systems. *Cold Spring Harbor Protocols* **2012** (2012).
27. Kern W, P.D. Cleaning solutions based on hydrogen peroxide for use in silicon semiconductor technology. *RCA Review* **31**, 187-206 (1970).
28. Joo, C. & Ha, T. Preparing Sample Chambers for Single-Molecule FRET. *Cold Spring Harbor Protocols* **2012** (2012).
29. Keppler, A., Pick, H. & of the ..., A.-C. Labeling of fusion proteins with synthetic fluorophores in live cells. *Proceedings of the ...* (2004).
30. Keppler, A. *et al.* A general method for the covalent labeling of fusion proteins with small molecules in vivo. *Nature biotechnology* **21**, 86 (2003).
31. Sun, X., Zhang, A., Baker, B., Sun, L. & ..., H.-A. Development of SNAP-tag fluorogenic probes for wash-free fluorescence imaging. ... (2011).
32. Gautier, A., Juillerat, A., Heinis, C. & biology, C.I.R. An engineered protein tag for multiprotein labeling in living cells. *Chemistry & biology* (2008).
33. Aitken, C.E., Marshall, R.A. & Puglisi, J.D. An oxygen scavenging system for improvement of dye stability in single-molecule fluorescence experiments. *Biophysical journal* **94**, 1826-1835 (2008).
34. Dave, R., Terry, D.S., Munro, J.B. & Blanchard, S.C. Mitigating unwanted photophysical processes for improved single-molecule fluorescence imaging. *Biophysical journal* **96**, 2371-2381 (2009).
35. Rasnik, I., McKinney, S.A. & Ha, T. Nonblinking and long-lasting single-molecule fluorescence imaging. *Nature Methods* **3**, 891893 (2006).
36. Alkalaeva, E.Z., Pisarev, A.V., Frolova, L.Y., Kisselev, L.L. & Pestova, T.V. In vitro reconstitution of eukaryotic translation reveals cooperativity between release factors eRF1 and eRF3. *Cell* **125**, 1125-1136 (2006).
37. Shoemaker, C.J., Eyler, D.E. & Green, R. Dom34:Hbs1 Promotes Subunit Dissociation and Peptidyl-tRNA Drop-Off to Initiate No-Go Decay. *Science* **330**, 369-372 (2010).
38. Shoemaker, C.J. & Green, R. Kinetic analysis reveals the ordered coupling of translation termination and ribosome recycling in yeast. *Proceedings of the National Academy of Sciences* **108** (2011).
39. Juette, M.F. *et al.* The bright future of single-molecule fluorescence imaging. *Current opinion in chemical biology* **20**, 103-111 (2014).
40. Frolova, L. *et al.* Eukaryotic polypeptide chain release factor eRF3 is an eRF1- and ribosome-dependent guanosine triphosphatase. *RNA (New York, N.Y.)* **2**, 334-341 (1996).
41. Salas-Marco, J. & Bedwell, D.M. GTP hydrolysis by eRF3 facilitates stop codon decoding during eukaryotic translation termination. *Molecular and cellular biology* **24**, 7769-7778 (2004).
42. Song, H. *et al.* The crystal structure of human eukaryotic release factor eRF1--mechanism of stop codon recognition and peptidyl-tRNA hydrolysis. *Cell* **100**, 311-321 (2000).
43. Graille, M., Chaillet, M. & van Tilbeurgh, H. Structure of yeast Dom34: a protein related to translation termination factor Erf1 and involved in No-Go decay. *The Journal of biological chemistry* **283**, 7145-7154 (2008).
44. Chen, L. *et al.* Structure of the Dom34-Hbs1 complex and implications for no-go decay. *Nature structural & molecular biology* **17**, 1233-1240 (2010).
45. Pisarev, A.V. *et al.* The role of ABCE1 in eukaryotic posttermination ribosomal recycling. *Molecular cell* **37**, 196-210 (2010).
46. Preis, A. *et al.* Cryoelectron microscopic structures of eukaryotic translation termination complexes containing eRF1-eRF3 or eRF1-ABCE1. *Cell reports* **8**, 59-65 (2014).
47. Yin, J., Lin, A.J., Golan, D.E. & Walsh, C.T. Site-specific protein labeling by Sfp phosphopantetheinyl transferase. *Nature protocols* **1**, 280-285 (2006).
48. Frolova, L.Y. *et al.* Mutations in the highly conserved GGQ motif of class 1 polypeptide release factors abolish ability of human eRF1 to trigger peptidyl-tRNA hydrolysis. *RNA (New York, N.Y.)* **5**, 1014-1020 (1999).
49. Kong, C. *et al.* Crystal structure and functional analysis of the eukaryotic class II release factor eRF3 from *S. pombe*. *Molecular cell* **14**, 233-245 (2004).
50. Chen, J. *et al.* High-throughput platform for real-time monitoring of biological processes by multicolor single-molecule fluorescence. *Proceedings of the National Academy of Sciences* **111**, 664-669 (2014).
51. Brown, A., Shao, S., Murray, J., Hegde, R.S. & Ramakrishnan, V. Structural basis for stop codon recognition in eukaryotes. *Nature* **524**, 493-496 (2015).

52. Shao, S. *et al.* Decoding Mammalian Ribosome-mRNA States by Translational GTPase Complexes. *Cell* **167**, 1229-561774592 (2016).
53. Chen, J. *et al.* Coupling of mRNA Structure Rearrangement to Ribosome Movement during Bypassing of Non-coding Regions. *Cell* **163**, 1267-1280 (2015).
54. Heuer, A. *et al.* Structure of the 40S-ABCE1 post-splitting complex in ribosome recycling and translation initiation. *Nature structural & molecular biology* **24**, 453-460 (2017).
55. Eyler, D.E. & Green, R. Distinct response of yeast ribosomes to a miscoding event during translation. *RNA* **17**, 925-932 (2011).
56. Acker, M.G., Kolitz, S.E., Mitchell, S.F., Nanda, J.S. & Lorsch, J.R. Reconstitution of yeast translation initiation. *Methods in enzymology* **430**, 111-145 (2007).
57. Gutierrez, E. *et al.* eIF5A promotes translation of polyproline motifs. *Molecular cell* **51**, 35-45 (2013).
58. Schuller, A.P., Wu, C.C., Dever, T.E., Buskirk, A.R. & Green, R. eIF5A Functions Globally in Translation Elongation and Termination. *Molecular cell* **66**, 194-20500000 (2017).

Curriculum Vitae

Laura Nevin Lessen

Birth

November 30, 1990 Baltimore, MD

Education

- 2013 – Present Ph.D. candidate, Johns Hopkins University School of Medicine, Baltimore, MD. Program in Molecular Biophysics. Anticipated completion September 2019.
- 2011 – 2012 B.S. in Chemistry, University of Maryland Baltimore County, Baltimore, MD, cum laude.
- 2008 – 2011 United States Naval Academy, Annapolis, MD. Superintendent's List four semesters

Research

- 2013 – Present Graduate student, Johns Hopkins University School of Medicine, Baltimore, MD under Professor Rachel Green, Department of Molecular Biology and Genetics. Biochemical studies of translation elongation, termination and ribosome recycling.
- 2012 Undergraduate research, University of Maryland Baltimore County, Baltimore MD under Professor William LaCourse. Mass spectrometry studies of the active molecule in a plant used to induce labor in underdeveloped countries.
- 2011 Undergraduate research, University of Maryland Baltimore County, Baltimore, MD under Professor James Fishbein. Complex organic synthesis of guanine crosslinks used to study DNA mutations.
- 2009 – 2011 Undergraduate research, United States Naval Academy, Annapolis, MD under Professor Paul Trulove. Investigated biopolymer mobilization and reorganization by ionic liquids in a process termed "Natural Fiber Welding" (Haverhals et al., 2012).

Publications

Petr Tesina*, **Laura N. Lessen***, Robert Buschauer, Jingdong Cheng, Colin Chih-Chien Wu, Otto Berninghausen, Allen R. Buskirk, Thomas Becker, Roland Beckmann, Rachel Green. 2019. Molecular mechanism of translational stalling by inhibitory codon combinations and poly(A) tracts. EMBO. (submitted)

Luke M. Haverhals, Matthew P. Foley, E. Kathryn Brown, **Laura M. Nevin**, Douglas M. Fox, Hugh C. De Long, and Paul C. Trulove. 2012. Ionic Liquid-based Solvents for Natural Fiber Welding. ECS Transactions 50(11): 603-613.

Luke M. Haverhals, **Laura M. Nevin**, Matthew P. Foley, E. Kathryn Brown, Hugh C. De Long and Paul C. Trulove. 2012. Fluorescence Monitoring of Ionic Liquid-facilitated Biopolymer Mobilization and Reorganization. Chem. Commun. 48(51): 6417-6419.

Presentations

Poster. Defining the Impact of Problematic Codon Pairs on Translation Elongation. EMBO Conference on Protein Synthesis and Translational Control, Heidelberg, Germany 2017.

Poster. Fundamental Investigations of Natural Fiber Welding. 243rd ACS National Meeting & Exposition, San Diego, CA 2012.

Teaching Experience

2016 Completion of the Johns Hopkins University Teaching Academy, Preparing Future Faculty Certificate Program. One-year program of college teacher training and academic career preparation through courses, workshops, teaching practicums, teaching-as-research fellowship appointments and individual consultation.

2016 Participation in the Johns Hopkins University Teaching Academy, Preparing Future Faculty Teaching Institute. A three-day teaching institute to advance the development of university-level educators by enhancing classroom teaching skills.

2015 – 2016 Teaching assistant (two semesters) to Professor Carolyn Fitch, Johns Hopkins University Department of Biophysics, for the course “Molecular Biophysics Laboratory.”

2015 Participation in the Johns Hopkins Medical Institute, Institute for Excellence in Education Summer Teaching Camp.